



Searching for saturation in forward dijet production at the LHC

A. van Hameren¹, H. Kakkad², P. Kotko², K. Kutak^{1,a}, S. Sapeta¹

¹ Institute of Nuclear Physics, Polish Academy of Sciences, Radzikowskiego 152, 31-342 Kraków, Poland

² Faculty of Physics and Applied Computer Science, AGH University of Krakow, al. Mickiewicza 30, 30-059 Kraków, Poland

Received: 30 June 2023 / Accepted: 9 October 2023 / Published online: 21 October 2023
© The Author(s) 2023

Abstract We review recent results for forward jets at the LHC and EIC as obtained within small- x Improved Transverse Momentum Dependent factorization (ITMD). In addition to elementary overview of various approaches to perturbative QCD at high energy, including High Energy Factorization, Color Glass Condensate and ITMD, we describe the Monte Carlo implementation and discuss the existing and unpublished phenomenological results for forward dijets.

1 Introduction

Quantum Chromodynamics (QCD) is a well established theory that describes interactions of quarks and gluons. However, it still has its challenges. In the high energy domain, one of the long standing problems is finding clear experimental signals of gluon saturation, which is a signature of quasi equilibrium between gluon splitting and gluon fusion in dense nuclear systems. Gluon saturation has been predicted from QCD long time ago [1, 2] and has been extensively studied using various approaches, most recently the Color Glass Condensate (CGC) – i.e. effective theory obtained within QCD (for a reviews see [3–7] and the textbook [8]).

While there is no doubt that gluon distributions must saturate at some point due to the unitarity constraints on the cross section, and there are strong indications of saturation in the data [9–20], a complete consensus on reaching it is still to be achieved. This is mainly due to the demanding kinematics, which requires the final states to be measured in the forward region of the detectors. This configuration of jets is triggered by an asymmetry in the partonic state of colliding hadrons – one of the colliding hadron is probed at a very low longitudinal momentum fraction while the other at rather large longitudinal momentum fraction (see also Sect. 2. In this scenario, one expects to reach saturation at values of longitudi-

nal momentum fraction at about 10^{-5} . The saturation is also expected to be stronger for nuclei, in the same kinematic domain. Once the saturation is reached the shapes of jet correlation spectra are expected to be broadened as compared to the non-saturated case, although this signal is strongly affected by the Sudakov resummation (see Sect. 6.3). Therefore, it is essential to compare forward jet observables for proton–proton and proton–nucleus collisions.

Another of the challenges in dealing with nuclear targets is the rich collision environment (see e.g. [21]). Moreover, theoretical predictions in high energy QCD are at present not as precise as those requiring ordinary collinear factorization.

Among various final states that can be measured in the context of saturation searches, the system consisting of two identified jets in the forward region (and everything else) plays a special role [22–24]. The typical transverse momentum of gluons in a high density medium is of the order of the saturation scale Q_s , which then induces a small imbalance between the jet transverse momenta. The saturation scale is of the order of a few GeV, for sufficiently high collision energy and sufficiently forward. This means, that the jet transverse momenta can be quite large, of the order of twenty GeV or so, and still provide sensitivity to the saturation effects in the back-to-back region. The single inclusive jet production, on the other hand, require jet transverse momenta to be of the order of the saturation scale, thus rather small. Obviously, jets with larger transverse momenta are easier to reconstruct and are “cleaner”. There is also some interest in the forward-central dijets [12, 25–28], but these do not probe sufficiently low fractions of the longitudinal momenta to be sensitive to saturation. Another appealing feature of harder forward dijets is that their description becomes possible in terms of “generalized” transverse momentum dependent (TMD) factorization, which is easier to implement in Monte Carlo generators than the full CGC.

Dijet yields at relatively forward rapidity have already been measured at the Large Hadron Collider (LHC) by

^a e-mail: krzysztof.kutak@ifj.edu.pl (corresponding author)

ATLAS collaboration for both proton–proton and proton–lead collisions [29]. Since there was no cross section measurement, the conclusions regarding saturation signals do not give yet a definite answer to whether saturation has been observed or not. Inclusive single forward jet energy spectra for proton–lead collisions measured at CMS CASTOR detector [30] does not provide convincing proof either. Further research and analysis are necessary to gain a better understanding of gluon saturation and its effects on nuclear systems. In particular, more measurements of both proton–proton and proton–lead collisions in the same kinematics are needed. In addition to the ATLAS forward detector, the ALICE collaboration plans to build a more forward detector FoCal [31] that hopefully will shed more light on the saturation phenomenon. The forward jet physics at LHC is complementary to the physics of the Electron Ion Collider (EIC) [32,33] one of the primary goals of which is to study gluon saturation physics.

In this work, we review the theoretical framework suitable for a description of forward dijet production in hadro and lepto-production in the full azimuthal angle range. The formalism lies in the intersection of the CGC theory and more traditional factorization approach, utilizing TMD gluon distributions. Since the formalism accounts for power corrections it has been dubbed as Improved TMD Factorization (ITMD) [34]. A review of some essential aspects of high energy QCD and the ITMD framework itself is contained in Sect. 4. We shall also review Monte Carlo implementation of the ITMD framework KATIE (Sect. 5), construction of the TMD gluon distributions, as well as recent phenomenological predictions for azimuthal dijet correlations, both for proton–proton and proton–lead collisions, in the kinematics of the forward calorimeters of ATLAS detector and planned FoCal of ALICE (Sect. 6). We also include new unpublished earlier computations of the rapidity distributions for different kinematic cuts.

2 Kinematics

The process in question is the inclusive production of two jets, that is, there are at least two jets with transverse momenta above a certain threshold:

$$A(P_A) + p(P_B) \rightarrow J(p_1) + J(p_2) + X, \tag{1}$$

where A is either the proton state p or a nucleus having the four momentum P_A that is hit by the proton state with four momentum P_B (see Fig. 1). The produced jets have four momenta p_1 and p_2 and are defined by a proper jet algorithm. X corresponds to other particles produced in the process; there are no kinematic cuts imposed on those additional

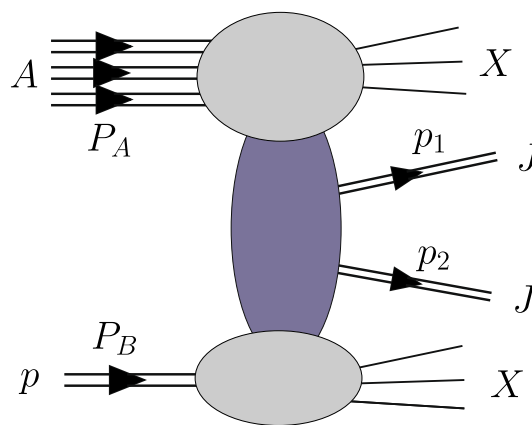


Fig. 1 The momentum assignment in the inclusive dijet production in p+A collision. The multiple double lines represent the nuclear target A . J are the jets with momenta p_1 and p_2 . X denotes arbitrary final states

states. We shall also discuss the complementary DIS process

$$A(P_A) + e^-(P_B) \rightarrow J(p_1) + J(p_2) + e^-(P'_B) + X, \tag{2}$$

which will be studied at EIC and will be essential in testing the theoretical formalism and constraining the nonperturbative input.

We are interested in the kinematic regime, where both jets $J(p_1)$ and $J(p_2)$ are produced in the “forward” rapidity interval, i.e. both jets have positive (or negative) sufficiently large rapidity. There is no universal definition as to what rapidity is considered sufficiently large. Basing on the current LHC setup, one can consider particles with rapidity $|y| > 2.5$ in the center of mass frame as being produced forward. Taking into account the planned forward calorimeters, the upper limit for the rapidity of reconstructed jets is about $|y| < 5.1$.

In what follows, we define the P_A and P_B four momenta as being the two light cone vectors, defining the “plus” and “minus” light cone components:

$$\begin{aligned} P_A^\mu &= (E_A, 0, 0, -E_A) = E_A n_+^\mu, \\ P_B^\mu &= (E_B, 0, 0, E_B) = E_B n_-^\mu, \end{aligned} \tag{3}$$

with the center of mass energy $s = 2P_A \cdot P_B$. Using these, the Sudakov decomposition of any four vector reads:

$$k^\mu = k^+ n_-^\mu + k^- n_+^\mu + k_T^\mu, \tag{4}$$

where

$$k_T \cdot P_A = k_T \cdot P_B = 0, \quad k_T \cdot k_T = -|\vec{k}_T|^2. \tag{5}$$

The central assumption in our investigations is that the nucleus (or a proton) is probed at small longitudinal momentum transfers compared to the hadron longitudinal momentum. That is, we define longitudinal momentum fractions

$$x_A = \frac{k_1 \cdot P_B}{P_A \cdot P_B}, \quad x_B = \frac{k_2 \cdot P_A}{P_B \cdot P_A}, \tag{6}$$

where k_1 is the momentum transferred to the target A , whereas k_2 is the momentum transferred to the proton target. We assume

$$x_A \ll x_B. \quad (7)$$

These fractions can be also expressed in terms of the final state rapidities y_i and transverse momenta

$$\begin{aligned} x_A &= \frac{1}{\sqrt{s}} (p_{T1} e^{-y_1} + p_{T2} e^{-y_2}), \\ x_B &= \frac{1}{\sqrt{s}} (p_{T1} e^{y_1} + p_{T2} e^{y_2}), \end{aligned} \quad (8)$$

Therefore, restricting the final states to a window with large rapidities as explicitly defined above and keeping the jet transverse momenta relatively low guarantees the smallness of x_A . For the LHC conditions, in the considered forward kinematic setup the x_A can be as low as 10^{-5} .

In phenomenological applications, we shall follow the realistic setup of the LHC experiments that measured (or plan to measure) forward dijets in proton–proton and proton–nucleus collisions: ATLAS and ALICE with their planned forward calorimeter FoCal. We shall discuss the kinematic cuts more precisely in Sect. 6 devoted to phenomenology.

3 QCD at high energy

One of the biggest achievements in theoretical developments of perturbative QCD are hard factorization theorems (see [35] for a review). These include the collinear factorization and the TMD factorization. They are applicable for processes that admit a large “hard scale” Q^2 , related to the momentum transfer to a hadron, so that the coupling constant $\alpha_s(Q^2)$ is small enough to permit the perturbation theory. Both types of factorization can be proved to all orders in coupling constant α_s and the leading power in the hard scale Q^2 , for few sufficiently inclusive processes. In practice, not only the truncation of perturbation series in α_s is necessary (at present at very low orders), but also the limit $Q^2 \rightarrow \infty$ is rarely adequate. Indeed, when comparing with experimental data, for example for large transverse momenta dijet production in the central rapidity region [36, 37], both a normalization factor (the so-called K -factor) is needed, as well as a resummation (parton shower) with the addition of semi-nonperturbative effects (like multiple partonic interactions).

In computations within the collinear factorization, one encounters powers of logarithms of the CM energy \bar{s} of colliding partons at every perturbative order, $\bar{s} = x_A x_B s$, where s is the total available CM energy. Therefore, at very large total CM energies, small transverse momenta, forward particle production, or a mixture of all of these conditions, these logarithms become large, even at the perturbative orders

not accounted for in the computation. Thus, the perturbative expansion becomes less reliable. Although within the collinear factorization, it is in principle possible to resum the logarithms of small x (see [38] and references therein), this does not address the two important issues.

First, within the collinear factorization the evolution of the Parton Distribution Functions (PDFs) describing the non-perturbative input is always linear, which is a result of a simple branching of partons. Denote a PDF as $f_i(x, \mu^2)$, where i is a parton type, x is the longitudinal momentum fraction carried by the parton, and μ^2 is the factorization scale. The evolution of $f_i(x, \mu^2)$ happens in the scale μ^2 that, intuitively, is inversely proportional to the spatial resolution scale. Decreasing the resolution scale, we find more gluons in a hadron due to the perturbative gluon emissions, and thus the gluon PDF slowly grows with decreasing μ^2 . The collinear factorization, however, does not directly restrict the behaviour of the PDFs in x , which turns out to be much more dramatic. The global fits (e.g. [39, 40]) predict a very steep increase of gluon PDF $f_g(x, \mu^2)$ in $1/x$. This is a consequence of the QCD perturbation theory and simple branching of partons. As mentioned in the previous paragraph, the perturbative calculations admit logarithms of $1/x$. Resummation of these leading logarithms to all orders predicts growth of the cross section as a power of $1/x$. In fact, this behaviour is usually implied in the initial parametrizations of the gluon PDFs. As we will recall in more detail in the following sections, the linear growth of the PDFs with the energy and, in turn, the cross section is in contradiction with the unitarity of the scattering matrix [41], known as the Froissart bound. Taming this behavior requires including gluon recombination, which cannot be implemented in any kind of linear evolution.

Second, the collinear factorization neglects higher twist effects that contribute to the power corrections of the order $\mathcal{O}(1/Q^2)$. As mentioned, realistically Q^2 is always finite. Moreover, for many processes, the inverse powers of Q^2 can be enhanced by other scales; for example, dijet production processes involve the dijet momentum imbalance which enhances the power corrections away from the correlation peak. For a discussion of higher twists in inclusive DIS and Drell-Yan see e.g. [42–47].

Below, we briefly recall the existing approaches that attempt to address the above issues (for an extensive and pedagogical review of high energy QCD see [8]). We focus on the central ideas and main references, skipping the technical details. We start with recalling the issues of energy dependence of hadronic cross section, a discussion that predates the QCD.

3.1 Pomeron and the Reggeon field theory

Historically, Pomeron – the Regge trajectory with the intercept greater than one and vacuum quantum numbers, was

introduced in order to explain the growth of the total hadronic cross section with energy observed in the data gathered in the early 1970s by the Intersecting Storage Rings (ISR) at CERN (see e.g. [48]). The Pomeron exchange results in a behavior of the cross section as $\sim s^{\omega_0}$, where $\omega_0 > 1$. However, according to the Froissart theorem [41] based on the unitarity and analytic properties of the S-matrix, the cross section should not grow faster than $\sim \ln s$. These facts, although pre-dating QCD, provide a major motivation for the study of high energy QCD.

The nature of the Pomeron quasi-particle is essentially non-perturbative. Together with its parity-odd partner, the Odderon, they constitute a possible effective theory of strong interactions with color singlet degrees of freedom. Typically, their interactions are described by the Euclidean field theory called the Regge field theory [49] (see also [50–52]). In its most general form, it includes the multiple Pomeron and Odderon interactions, but in the context of unitarity, one typically studies a truncation to the triple Pomeron vertex.

In perturbative QCD the parity even color singlet state exchanged in the t channel can be made out of two gluons. This leads to the perturbative Pomeron of Balitsky, Fadin, Kuraev and Lipatov (BFKL) [53–56] (for a pedagogical review see eg. [57]). The corresponding energy evolution equation of the Pomeron Green function gives the power like behavior of the cross section with energy. The triple Pomeron vertex needed for nonlinear taming of the growth can also be constructed in QCD [58–60]. The difference in the Pomeron intercept derived in perturbative QCD and the one needed to describe for example elastic hadron-hadron scattering leads to a distinction between the hard and the soft Pomeron.

There are numerous applications of the Pomeron calculus to particle production; in particular, there exist several Monte Carlo event generators: PHOJET and DPMJET [61, 62], EPOS [63, 64], SIBYLL [65, 66], QGSJET [67, 68].

3.2 Lipatov effective action

In view of the BFKL approach to Pomeron physics, it turns out, that the computations in QCD at high energy can be done using the effective building blocks: the “reggeized” gluons R and effective interaction vertices $RR \rightarrow g$. The former are characterized by the eikonal coupling to ordinary QCD vertices (due to the high energy approximation) and the “reggeization” factor $(-s)^{\omega(t)}$ appearing due to radiative corrections, where $\omega(t)$ is the perturbative Regge trajectory. The RRg effective vertices are separated in rapidity (the so-called quasi-multi-Regge kinematics).

Stripping off the reggeization factors, the building blocks can be formalized into an effective gauge invariant action [69, 70] that contains both the QCD degrees of freedom, and the reggeized gluon fields A_+, A_- , that, roughly, by virtue of equations of motions are straight semi-infinite Wilson lines

along two light-cone directions P_A and P_B . The vertices are naturally generalized into $RRg \dots g$ vertices, as well as multiple reggeon vertices. For a review see [71] (chapter 11 in [72]).

Using Lipatov’s high energy effective action beyond tree level is rather cumbersome due to double counting between gluon field and composite reggeons, but several results have been obtained (see for example [73–77]). The important feature of that action is that it includes all the necessary ingredients to unitarize the cross section. In particular in [78–81] a relation to the Color Glass Condensate was established and investigated.

3.3 High energy operator product expansion

It turns out that in high energy QCD, the non-perturbative information is rather naturally contained in hadronic matrix elements of straight infinite Wilson lines, instead of the PDFs. It is convenient to recall the evolution equation for their energy dependence via the high energy operator product expansion (OPE) [82]. Similar to Wilsonian OPE, it is straightforwardly applicable only for fully inclusive quantities.

Consider a projectile, a photon for simplicity, scattering off a hadron in a frame where it is moving slowly. The photon fluctuates into a pair of quarks well before it hits the target and – at high energies – interacts with the target eikonally. In the considered high energy kinematics, the target is made of gluons, that are treated as background field, which shrinks to a shock wave. The quark-antiquark dipole interacts with that shockwave becoming a straight infinite Wilson lines of the background field. Since the scattering cross section is related to the hadronic matrix element of the time ordered product of quark current, effectively, the above picture provides a means of decomposing the hadronic tensor into products of Wilson lines and the so-called impact factors. This is the essence of the high energy operator product expansion [82]. More precisely, the time ordered product of electromagnetic currents at high energy can be decomposed as

$$\mathcal{T} \{ J_{\text{em}}^\mu(x) J_{\text{em}}^\nu(y) \} = \int d^2z_{1T} d^2z_{2T} \times \mathcal{I}_2^{\mu\nu}(x, y; \vec{z}_{1T}, \vec{z}_{2T}) \text{Tr} U(\vec{x}_T) U^\dagger(\vec{y}_T) + \dots, \tag{9}$$

where

$$U(\vec{x}_T) = \mathcal{P} \exp \left\{ ig \int dw^+ \hat{A}^-(x_T + w^+) \right\} \tag{10}$$

is the straight infinite Wilson line along the plus light cone direction and fixed transverse position, whereas $\mathcal{I}_2^{\mu\nu}$ is the leading order impact factor. The dots represent the subleading corrections. In the collinear factorization, usually the hadronic matrix element is traded to the partonic one when deriving the evolution equation via operator renormalization

procedure. Analogously, here the hadronic matrix elements is traded to the matrix element of the background gluon field

$$\frac{\langle P_A | \dots | P_A \rangle}{\langle P_A | P_A \rangle} \rightarrow \langle \dots \rangle. \tag{11}$$

The distinction between the background field and the projectile is related to the rapidity; formally the matrix elements depend on the rapidity cutoff. This dependence is explicitly introduced when regulating the rapidity divergence appearing when considering perturbative correction. However, a perturbative gluon interacting with the shock wave generates an adjoint Wilson line that gives a product of four fundamental Wilson lines. The evolution of this four-point correlator generates in turn further higher point correlators. Therefore the resulting evolution equation is not closed and consists of a tower of products of an increasing number of Wilson lines, known as the Balitsky hierarchy. However, at the large N_c limit, the hierarchy is terminated and one obtains a single evolution equation for the product of two Wilson lines, the so-called *dipole* amplitude

$$N(\vec{x}_T, \vec{y}_T; \eta) = 1 - \frac{1}{N_c} \langle \text{Tr} U(\vec{x}_T) U^\dagger(\vec{y}_T) \rangle, \tag{12}$$

where η is the implicit rapidity cutoff. The evolution equation [82] reads

$$\begin{aligned} \frac{\partial}{\partial \eta} N(\vec{x}_T, \vec{y}_T; \eta) &= \frac{\alpha_s N_c}{2\pi} \int d^2 z_T \\ &\times \frac{(\vec{x}_T - \vec{y}_T)^2}{(\vec{x}_T - \vec{z}_T)^2 (\vec{y}_T - \vec{z}_T)^2} \left\{ N(\vec{x}_T, \vec{z}_T; \eta) + N(\vec{y}_T, \vec{z}_T; \eta) \right. \\ &\left. - N(\vec{x}_T, \vec{y}_T; \eta) - N(\vec{x}_T, \vec{z}_T; \eta) N(\vec{z}_T, \vec{y}_T; \eta) \right\}. \end{aligned} \tag{13}$$

It was also obtained independently in [83] using the Mueller dipole approach [84] and is therefore called the Balitsky–Kovchegov (BK) equation.

Typically one introduces new variables, the dipole size

$$\vec{r}_T = \frac{\vec{x}_T - \vec{y}_T}{2}, \tag{14}$$

and the impact parameter

$$\vec{b}_T = \frac{\vec{x}_T + \vec{y}_T}{2}. \tag{15}$$

The usual treatment of that equation assumes an infinite target and thus neglects the impact parameter dependence [85–93], but solutions with impact parameter are also known, see [94] and the following works, including [95–100].

Let us finally mention the huge progress in controlling next-to-eikonal corrections, see [101–107], as well as the development of the next-to-leading order BK equation [108–113].

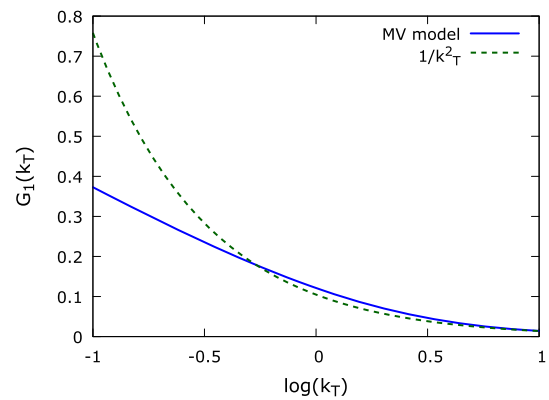


Fig. 2 Gluon saturation phenomenon in the MV model. The perturbative behaviour $\sim 1/k_T^2$ is tamed at $k_T \sim Q_s$, with Q_s increasing with energy

3.4 Color glass condensate

The High Energy Operator Product expansion does provide the evolution equation but does not allow for the calculation of the non-perturbative correlators itself. On the other hand, the effective theory of high energy QCD – the Color Glass Condensate (CGC) theory is a convenient framework to approach both the evolution and averages of Wilson lines in the background color field. For a full review of the CGC theory see for example [5].

In this part of the overview, we would like to focus on the essential aspects of the CGC theory, in particular how the saturation of a gluon distribution emerges. The procedure of computing dijet cross section within the CGC will be outlined in the next section.

To this end, let us now review a famous model of large nucleus – the McLerran–Venugopalan (MV) model [114,115]. Assume we view a large nucleus with a large number of nucleons in a frame where it is moving with a very large velocity. In that boosted frame, large x partons are localized in one of the light-cone directions and can be considered as color sources for the classical Yang–Mills fields. These sources are some, a priori unknown, distributions in the transverse plane $\rho_a(x_T)$ and are considered independent within the large nucleus because there are large numbers of nucleons inside. One can solve the Yang–Mills equation for such configuration to obtain the gluon “wee” fields. In order to compute observables, one needs to average over the color sources. For example, a basic quantity to consider is the particle number density with the generic definition

$$\frac{dn}{d^3\mathbf{k}} \sim \langle P_A | \tilde{A}_b^i(y^+, \mathbf{k}) \tilde{A}_b^i(y^+, -\mathbf{k}) | P_A \rangle, \tag{16}$$

where \tilde{A}_b^i are partially Fourier transformed gauge fields, $\mathbf{k} = (k^+, \vec{k}_T)$ is a three-vector conjugate to $\mathbf{y} = (y^-, \vec{y}_T)$. We have assumed here that the large boost is in the light

cone “plus” direction. In the MV model, the hadronic matrix element of the gluon field correlator is traded to

$$\langle A_b^i(\mathbf{y}) A_b^i(\mathbf{z}) \rangle_x = \int [d\rho] \mathcal{W}_x[\rho] A_b^i[\rho](\mathbf{y}) A_b^i[\rho](\mathbf{z}), \tag{17}$$

where the averaging is over the color sources in the functional sense. \mathcal{W}_x is the functional weight for random color sources, which in the MV model is a Gaussian. Direct computation of the above gluon distribution leads to the so-called Weizsacker-Williams (WW) gluon distribution [116,117]. Interestingly, despite it being the most basic quantity in the MV model it is not the easiest one to compute nor can it be probed in the simplest scattering processes. Rather, as we discuss later, the quantities that appear for example in inclusive DIS are correlators of Wilson lines. The WW gluon distribution can be approximated as

$$G_1(k_T) \sim \int d^2r_T \frac{e^{-i\vec{k}_T \cdot \vec{r}_T}}{|\vec{r}_T|} \times \left[1 - \exp\left(-\frac{1}{4}\alpha_s N_c \mu_A |\vec{r}_T|^2 \log \frac{1}{r_T \Lambda_{\text{QCD}}}\right) \right], \tag{18}$$

where μ_A is the average color charge per unit transverse area per color. The saturation phenomenon is visible in the above distribution as follows. If the two-point correlator (16) was an ordinary perturbative correlator it would behave like $\sim 1/k_T^2$; this behavior leads to the power-like growth of the gluon distribution. It turns out that (18) behaves like $\sim 1/k_T^2$ in the perturbative domain (large k_T), but at small k_T it behaves like $\frac{1}{\alpha_s} \log \frac{Q_s^2}{k_T^2}$, where Q_s is the scale at which the suppression happens, called the *saturation scale* (see Fig. 2). This dynamical scale depends on x (through the evolution) and increases with decreasing x .

The subscript x in the functional weight \mathcal{W}_x denotes a longitudinal cutoff between the sources and the “wee” partons. Decreasing the cutoff produces new color sources and thus the Gaussian distribution gets distorted. The CGC high energy effective theory predicts the evolution equation of \mathcal{W}_x in x . It is the so-called Jalilian–Marian–Iancu–McLerran–Weigert–Leonidov–Kovner (JIMWLK) equation [118–123] and has the following general form

$$\frac{d\mathcal{W}_x[\rho]}{d \ln x} = -H_{\text{JIMWLK}} \left[\rho, \frac{\delta}{\delta \rho} \right] \mathcal{W}_x[\rho], \tag{19}$$

where H_{JIMWLK} is the so-called JIMWLK Hamiltonian (we skip its exact form here). It gives a nonlinear evolution of \mathcal{W}_x and in turn also a nonlinear evolution of any gauge field-dependent quantity due to the averaging procedure in ρ . These equations are consistent with the Balitsky hierar-

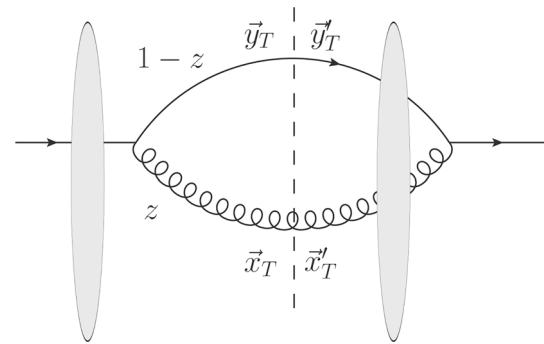


Fig. 3 Scattering of a color dipole $q \rightarrow qg$ off a nuclear target in CGC. The shaded ellipses symbolize the color field of a nucleus. This particular diagram corresponds to a contribution, where in the amplitude the incoming quark scatters off the color field of the nucleus before the splitting, while in the amplitude conjugate both gluon and a quark scatter after splitting. Particles scattering off the color field of the nucleus gain infinite straight Wilson line along the light cone, in their respective representations

chy mentioned earlier, therefore it is often called B-JIMWLK equation.

4 Forward dijet production in high energy QCD

In this section, we shall review the formalism that is suitable for phenomenological studies of forward jet production processes at moderate transverse momenta. The formalism lies at the intersection of the two aspects of QCD that in the past were rarely overlapping and, essentially, were exercised by distinct communities. One is the high energy scattering reviewed in the previous Section and the other is the hard factorization theorems, in particular the TMD factorization (see eg. [35] for a review).

4.1 Dijet production in dilute-dense collisions

We start with a CGC description of a scattering of a proton or a photon off a nuclear target to produce two partons. The basic assumption here is that, in the case of the proton projectile, it is dilute, that is the partons extracted from the projectile are moderate x partons. With that assumption, we can treat the scattering of color dipoles, such as $\gamma \rightarrow q\bar{q}$, $q \rightarrow qg$, etc., off a color field of a nucleus. This is the essence of the dilute-dense (or hybrid) approach which, as explained in Sect. 2, is kinematically well suited to study forward jets [124].

Consider, as an example, the scattering of a $q \rightarrow qg$ color system off a nuclear target (Fig. 3). In the shock wave approximation, the interaction with the color field of the nucleus can take place either before the quark splits or after. For example, in Fig. 3 the scattering takes place before the splitting in the amplitude and after the splitting in the amplitude conjugate. Each colored particle gains a nonabelian phase when

scattering, given by the Wilson line

$$U_R(\vec{x}_T) = \mathcal{P} \exp \left\{ ig \int_{-\infty}^{+\infty} dx^- A_a^+(x^-, \vec{x}_T) T_R^a \right\}, \quad (20)$$

where the generator T_R^a is in the fundamental representation ($R = F$) for a quark or in the adjoint representation ($R = A$) for a gluon. The cross section for the scattering of that system can be written as [22]

$$\begin{aligned} & \frac{d\sigma_{qA \rightarrow qg}}{d^2p_{1T} d^2p_{2T} dy_1 dy_2} \\ & \sim \int \frac{d^2x_T}{(2\pi)^2} \frac{d^2x'_T}{(2\pi)^2} \frac{d^2y_T}{(2\pi)^2} \frac{d^2y'_T}{(2\pi)^2} e^{-i\vec{p}_{1T} \cdot (\vec{x}_T - \vec{x}'_T)} e^{-i\vec{p}_{2T} \cdot (\vec{y}_T - \vec{y}'_T)} \\ & \quad \times \psi_q^*(z, \vec{x}'_T - \vec{y}'_T) \psi_q(z, \vec{x}_T - \vec{y}_T) \\ & \quad \times \left\{ S_x^{(4)}(\vec{y}_T, \vec{x}_T, \vec{y}'_T, \vec{x}'_T) \right. \\ & \quad - S_x^{(3)}(\vec{y}_T, \vec{x}_T, (1-z)\vec{y}'_T + z\vec{x}'_T) \\ & \quad - S_x^{(3)}((1-z)\vec{y}_T + z\vec{x}_T, \vec{y}'_T, \vec{x}'_T) \\ & \quad \left. - S_x^{(2)}((1-z)\vec{y}_T + z\vec{x}_T, (1-z)\vec{y}'_T + z\vec{x}'_T) \right\}, \quad (21) \end{aligned}$$

where $\psi_q(z, \vec{x}_T)$ is the wave function of the qg -dipole, with z being a fraction of the incoming quark momentum taken by a gluon. This wave function can be computed in perturbative QCD. The quantities in the curly bracket correspond to the color averages of the Wilson lines:

$$S_x^{(2)}(\vec{x}_T, \vec{y}_T) = \frac{1}{N_c} \langle \text{Tr} U_F(\vec{x}_T) U_F^\dagger(\vec{y}_T) \rangle_x \quad (22)$$

$$\begin{aligned} & \times S_x^{(3)}(\vec{x}_T, \vec{y}_T, \vec{z}_T) = \frac{1}{C_F N_c} \left\langle \text{Tr} \right. \\ & \times \left. \left\{ U_F^\dagger(\vec{z}_T) t^a U_F(\vec{x}_T) t^b \right\} U_A^{ab}(\vec{y}_T) \right\rangle_x \quad (23) \end{aligned}$$

$$\begin{aligned} & S_x^{(4)}(\vec{x}_T, \vec{y}_T, \vec{x}'_T, \vec{y}'_T) \\ & = \frac{1}{C_F N_c} \left\langle \text{Tr} \left\{ U_F(\vec{x}_T) U_F^\dagger(\vec{x}'_T) t^b t^a \right\} \right. \\ & \quad \times \left. \left\{ U_A(\vec{y}_T) U_A^\dagger(\vec{y}'_T) \right\}^{ab} \right\rangle_x. \quad (24) \end{aligned}$$

The above correlators depend on x through the B-JIMWLK equations. In practice, one often uses the Gaussian approximation [125], which states that the color source distribution stays Gaussian throughout the evolution. This allows us to compute the evolution of correlators in closed form.

In order to compute the differential cross section for dijet production in proton–nucleus scattering in the above setup, one needs to find the remaining color dipole contributions [22, 126] and convolute the parton-nucleus cross section with the ordinary collinear PDFs.

The CGC formulation of the dilute-dense scattering provides the high-energy description of the jet production at both small transverse momenta p_T of jets and moderate (at

very large p_T one should switch the approach from leading energy to leading power in the hard scale). The drawback of the above approach, in addition to being hard to generalize and implement in a Monte Carlo code, is that the perturbative information is contained not only in the color dipole wave function but also in the correlators. As we discuss later, in certain limits this information can be extracted and combined with the dipole wave function to obtain the hard matrix elements, similar to those known from hard factorization.

In the end, let us mention the huge progress in computing higher orders in particle production within the CGC framework. The NLO results for single inclusive jets have been available already for some time [127–129], also with resolutions of the “negative cross section” problem [130–133]. Further, there are NLO computations for inclusive DIS [19, 134], also with heavy quarks [135, 136], dijets in DIS [137–139], vector meson production [140, 141], dijet and dihadron hadroproduction [142–144] and Drell–Yan process [145]. Higher multiplicity LO computations in CGC include dijet and photon production [146], trijets [147] and trijets in photoproduction [148].

4.2 High energy (or k_T) factorization

Usually, the high energy factorization (HEF) (or k_T -factorization) refers to a description of particle production at asymptotically high energies in terms of “unintegrated” PDFs that undergo the BFKL [149–152] or CCFM [153, 154] evolution. More precisely, within HEF the cross section for a multi-jet production in a collision of two hadrons can be written as

$$\begin{aligned} & d\sigma_{AB} \left(P_A, P_B; p_1^{(J)}, \dots, p_n^{(J)} \right) \\ & = \int dx_A dx_B \int d^2k_{1T} d^2k_{2T} \mathcal{F}_{g/A} \left(x_A, |\vec{k}_{1T}| \right) \mathcal{F}_{g/B} \left(x_B, |\vec{k}_{2T}| \right) \\ & \quad \times d\hat{\sigma}_{RR} \left(x_A P_A + k_{1T}, x_B P_B + k_{2T}; p_1^{(J)}, \dots, p_n^{(J)}; \mu \right), \quad (25) \end{aligned}$$

where $\mathcal{F}_{g/H}$ are unintegrated gluon distributions defined as

$$\mathcal{F}_{g/H} \left(x, |\vec{k}_T| \right) = \int \frac{d^2p_T}{2\pi} \frac{\Phi_H(\vec{p}_T)}{|\vec{p}_T|^2} \mathcal{G} \left(\vec{p}_T, \vec{k}_T; x \right), \quad (26)$$

where Φ_H is the non-perturbative impact factor of a hadron and \mathcal{G} is the BFKL Green’s function. At leading order, the partonic cross section in (25) reads

$$\begin{aligned} & d\hat{\sigma}_{RR}^{(0)} \left(k_1, k_2; p_1^{(J)}, \dots, p_n^{(J)} \right) \\ & = \frac{1}{2x_A x_B S} \left| \bar{V}_{RR \rightarrow P \dots P} \left(k_1, k_2; p_1, \dots, p_n \right) \right|^2 \\ & \quad \times F \left(\{p_i\}, \{p_i^{(J)}\} \right) d\Gamma_n \left(\{p_i\} \right), \quad (27) \end{aligned}$$

where $V_{RR \rightarrow P \dots P}$ (the bar denotes the usual spin/color summation and averaging) is the suitably normalized tree-level

$RR \rightarrow P \dots P$ vertex to produce n partons (jets), with R being reggeon states understood as fields from the high energy Lipatov’s action (i.e. without the “reggeization” factors), while P being on-shell quarks or gluons. Above, $d\Gamma_n$ is ordinary on-shell phase space and F is a jet function that implements the cuts. The momenta of reggeons are

$$k_1^\mu = x_A P_A^\mu + k_{1T}^\mu \quad k_2^\mu = x_B P_B^\mu + k_{2T}^\mu. \quad (28)$$

Notice that they are off-shell $k_{1,2}^2 = -|\vec{k}_{T1,2}|^2$ and lack one of the light-cone components, due to the high energy approximations. In the original work on HEF in heavy quark production [150] the partonic cross section (27) was expressed in terms of off-shell amplitude to produce heavy quark pair, with initial gluons having momenta (28) and projected onto P_A and P_B (eikonal coupling). In that simple case, it turns out that the amplitude calculated in terms of ordinary diagrams is gauge invariant, despite the initial gluons being off-shell. In practical applications, it proves to be very convenient to stick to that logic also for more complicated processes, instead of using Lipatov’s effective action. Indeed, it is possible to define off-shell gauge invariant amplitude for arbitrary processes. In addition to ordinary Feynman diagrams (with off-shell space-like gluons), one needs “gauge restoring” contributions. Those additional diagrams can be reconstructed for example by the “embedding” method [155], where an off-shell process is embedded in an on-shell process with special kinematics of the auxiliary quarks or gluons. This method was automatized for arbitrary Standard Model tree level process in the KATIE Monte Carlo discussed in Sect. 5.¹ Also, other methods suitable for automatization were also developed [158–161]. In Fig. 4 we illustrate one of the methods.

In the context of forward jets, one can apply similar considerations to the hybrid approach explained before. Namely, when, say, x_B is moderate and not small, one should extract partons from collinear PDF rather than unintegrated PDF undergoing BFKL evolution. This was discussed in [162] and the corresponding HEF formula reads

$$d\sigma_{AB}^{\text{forward}}(P_A, P_B; p_1^{(J)}, \dots, p_n^{(J)}) = \sum_a \int dx_A dx_B \int d^2k_T f_{a/B}(x_B, \mu) \mathcal{F}_{g/A}(x_A, |\vec{k}_T|; \mu) \times d\hat{\sigma}_{ag^*}(x_B P_B, x_A P_A + k_T; p_1^{(J)}, \dots, p_n^{(J)}; \mu), \quad (29)$$

where we have explicitly denoted the fact that the partonic cross section is constructed from amplitude with one off-shell (gauge invariant) gluon. Above $f_{a/B}$ is the collinear PDFs for parton a (quark or gluon) in hadron B .

¹ The first Monte Carlo implementation of the High Energy Factorization was achieved within the CASCADE framework [156, 157].

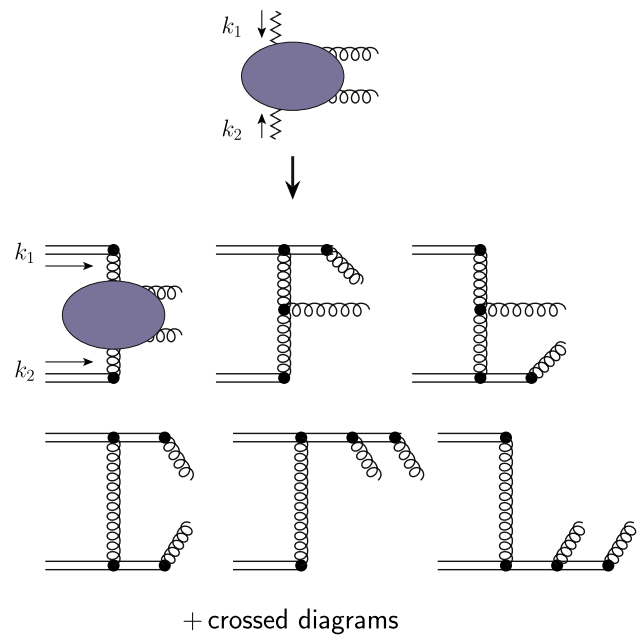


Fig. 4 Off-shell gauge invariant amplitude (upper blob – the zigzag lines represent off-shell gauge invariant gluons) can be constructed by promoting a single off-shell gluon coupled eikinally to a straight infinite Wilson line along corresponding hadron momenta P_A or P_B . Here we show diagrams for the production of two gluons at tree level. The double line represents the momentum space Wilson line along P_A (for the top line) and P_B (for the bottom line). Gluons couple to these Wilson lines via $igt^a p_{A(B)}^\mu$ and the double-line propagators have form $i/(k \cdot p_{A(B)} + i\epsilon)$. Only planar diagrams are shown. The blob represents all possible connections of gluons via standard vertices

Let us now refocus our attention to the dijet case. It turns out that the k_T -factorization formula with proper gauge invariant off-shell amplitudes can be retrieved from the CGC expressions discussed before [34, 126]. In the dilute limit, which corresponds to $|\vec{k}_T| \gg Q_s$, one can neglect the multiple scattering off the target. This means that the triple and quadrupole operators $S^{(3)}$, $S^{(4)}$ can be expressed only in terms of the dipole $S^{(2)}$. In that limit, one obtains for the $q \rightarrow qg$ dipole scattering

$$\frac{d\sigma_{pA \rightarrow qg}}{d^2p_{1T} d^2p_{2T} dy_1 dy_2} = x_B f_{q/B}(x_B, \mu^2) \mathcal{F}_{g/A}(x_A, |\vec{k}_T|) \times \frac{\alpha_s}{2\pi} \frac{(1-z)(1+(1-z)^2)}{|\vec{p}_{1T}|^2 |\vec{p}_{2T}|^2} \times \left[1 + \frac{(1-z)^2 |\vec{p}_{T1}|^2}{|\vec{P}_T|^2} - \frac{1}{N_c^2} \frac{z^2 |\vec{p}_{T2}|^2}{|\vec{P}_T|^2} \right], \quad (30)$$

where

$$\vec{P}_T = (1-z)\vec{p}_{1T} + z\vec{p}_{2T} \quad (31)$$

and the unintegrated gluon distribution is related to the average of the weak field limit of the CGC dipole operator as follows

$$\mathcal{F}_{g/A}(x, |\vec{k}_T|) = \frac{N_c}{\alpha_s(2\pi)^3} \int d^2 y_T d^2 z_T e^{-i\vec{k}_T \cdot (\vec{y}_T - \vec{z}_T)} \nabla_{\vec{y}_T - \vec{z}_T}^2 \left[1 - S_x^{(2)\text{weak}}(\vec{y}_T, \vec{z}_T) \right]. \tag{32}$$

The hard factor obtained above turns out to be exactly the off-shell gauge invariant amplitude.

4.3 TMD factorization

Formally, the TMD factorization is the leading power (in the hard scale μ^2) factorization of a cross section into TMD dependent PDFs and hard factors, that to leading power are on-shell (for a review see [35, 163, 164]). This factorization does not resum the large small- x logarithms and therefore becomes unreliable at very high energies. Moreover, it is not expected to hold to all orders in perturbation theory for the processes we are interested in. However, the formalism provides sturdy theoretical definitions of the TMD gluon distributions that, as it turns out, can be matched to the CGC correlators.

In TMD factorization, gluon distribution is given by the Fourier transform of the bilocal matrix element of the gluon field strength tensor

$$\mathcal{F}_{C_1 C_2}(x, |\vec{k}_T|) = 2 \int \frac{d\xi^- d^2 \xi_T}{(2\pi)^3 P_A^+} e^{ix P_A^+ \xi^- - i\vec{k}_T \cdot \vec{\xi}_T} \times \langle P_A | \text{Tr} \hat{F}^{j+}(\xi^-, \vec{\xi}_T, 0) \mathcal{U}_{C_1} \hat{F}^{j+}(0) \mathcal{U}_{C_2} | P_A \rangle, \tag{33}$$

where $\hat{F}^{j+} = F_a^{j+} t^a$ is the gluon field strength tensor; the two operators are displaced in both the light cone and transverse direction (unlike in the collinear PDF, where the displacement is only along the light cone). The bilocal operator would not be gauge invariant, therefore the proper general definition requires gauge links \mathcal{U}_{C_1} and \mathcal{U}_{C_2} (here everything is in the fundamental representation) that connect the two space-time points. There is also a possibility of the double-trace over the fundamental representation (see below). We consider here only the unpolarized case, therefore the transverse index j is summed over. The TMD gluon distributions are connected to a partonic process by virtue of factorization. Since we consider gauge theory, there are multiple soft and collinear gluons that can be connected to various places in the diagrams. The definition given above corresponds to the bare operator. In perturbation theory, it contains UV and rapidity divergences that, for some processes, can be removed order-by-order by the operator renormalization and by (part of) the soft factor accumulating soft gluons. This gives the hard scale and rapidity evolution of the TMD PDFs. The collinear gluons (collinear to the target hadron) can be resummed into the Wilson lines \mathcal{U}_{C_1} and \mathcal{U}_{C_2} . As can be easily understood, the form of these Wilson lines depends on the actual hard process (its color flow). In [165] a general procedure of determining

these Wilson lines via resummation of collinear gluons was given. It turns out, that they can become quite complicated for colored partonic processes, see for example [166]. In Table 1 we collect the operators relevant for the dijet production. The notation $\mathcal{F}_{gg}^{(i)}$ and $\mathcal{F}_{qg}^{(i)}$ corresponds to TMD PDFs that appear for incoming gluons (the ‘‘gg’’ subscript) or quark-gluon system (the ‘‘qg’’ subscript), and various color flows (the (i) superscript). The Wilson lines $\mathcal{U}^{[\pm]}$ are defined as

$$\mathcal{U}^{[-]} = \left[(\xi^-, \vec{\xi}_T, 0), (-\infty, \vec{\xi}_T, 0) \right] \times \left[(-\infty, \vec{\xi}_T, 0), (-\infty, \vec{0}_T, 0) \right] \left[(-\infty, \vec{0}_T, 0), (0, \vec{0}_T, 0) \right], \tag{34}$$

which is the past-pointing staple-like gauge link and

$$\mathcal{U}^{[+]} = \left[(\xi^-, \vec{\xi}_T, 0), (+\infty, \vec{\xi}_T, 0) \right] \times \left[(+\infty, \vec{\xi}_T, 0), (+\infty, \vec{0}_T, 0) \right] \left[(+\infty, \vec{0}_T, 0), (0, \vec{0}_T, 0) \right] \tag{35}$$

is the future pointing ‘‘staple’’, see Fig. 5. The square brackets above $[x, y]$ is a standard notation for segments of straight gauge link between the points x and y . Out of two staples it is possible to make a Wilson loop

$$\mathcal{U}^{[\square]} = \mathcal{U}^{[-]} \mathcal{U}^{[+]}. \tag{36}$$

The relation of the field theoretical definitions of TMD PDFs and small- x QCD has been a subject of intense work, see for example [167–178]. In the context of forward dijet production, we are interested in the small- x limit of the TMD gluon distributions. This is achieved by literally taking the limit $x_A \rightarrow 0$ in the definitions. On the other hand, one can consider the leading power limit of the CGC expressions (21). This leads to the identification of the TMD gluon distributions and the leading terms in the gradient expansions of the CGC correlators [168]. For example

$$\mathcal{F}_{qg}^{(1)} = \frac{1}{\pi \alpha_s} \int \frac{d^2 x_T d^2 y_T}{2\pi^3} e^{-i\vec{k}_T \cdot (\vec{x}_T - \vec{y}_T)} \times \langle \text{Tr} \partial_j U_F(\vec{y}_T) \partial_j U_F^\dagger(\vec{x}_T) \rangle_x, \tag{37}$$

$$\mathcal{F}_{qg}^{(2)} = -\frac{1}{\pi \alpha_s N_c} \int \frac{d^2 x_T d^2 y_T}{2\pi^3} e^{-i\vec{k}_T \cdot (\vec{x}_T - \vec{y}_T)} \times \left\langle \text{Tr} \left\{ \partial_j U_F(\vec{x}_T) U_F^\dagger(\vec{y}_T) \partial_j U_F^\dagger(\vec{y}_T) U_F(\vec{x}_T) \right\} \right\rangle_x \times \left\langle \text{Tr} \left\{ U_F(\vec{y}_T) U_F^\dagger(\vec{x}_T) \right\} \right\rangle_x, \tag{38}$$

that is, the $\mathcal{F}_{qg}^{(1)}$ is identified with the expansion of the dipole operator. For the complete list of similar relations for other TMDs see [168, 179]. Ultimately, in the leading power limit, the CGC formula for the $qg \rightarrow qg$ contribution can be written as

Table 1 Gauge links \mathcal{U}_{C_1} and \mathcal{U}_{C_2} in terms of the “staple-like” Wilson lines contributing to TMD gluon distributions that are coupled to independent color flows of $gg \rightarrow gg$ and $gg \rightarrow q\bar{q}$ (upper table) and

$qg \rightarrow qg$ (lower table) processes. The operators in the column marked with a star * should be traced with the gluon field strength tensor independently

$\mathcal{F}_{C_1 C_2}$	$\mathcal{F}_{gg}^{(1)}$	$(*)\mathcal{F}_{gg}^{(2)}$	$\mathcal{F}_{gg}^{(3)}$	$\mathcal{F}_{gg}^{(4)}$	$\mathcal{F}_{gg}^{(5)}$	$\mathcal{F}_{gg}^{(6)}$
\mathcal{U}_{C_1}	$\frac{\text{Tr}\mathcal{U}^{[\square]\dagger}}{N_c}\mathcal{U}^{[-]\dagger}$	$\mathcal{U}^{[\square]\dagger}$	$\mathcal{U}^{[+]\dagger}$	$\mathcal{U}^{[-]\dagger}$	$\mathcal{U}^{[\square]\dagger}\mathcal{U}^{[+]\dagger}$	$\frac{\text{Tr}\mathcal{U}^{[\square]\dagger}}{N_c}\mathcal{U}^{[+]\dagger}$
\mathcal{U}_{C_2}	$\mathcal{U}^{[+]}$	$\mathcal{U}^{[\square]}$	$\mathcal{U}^{[+]}$	$\mathcal{U}^{[-]}$	$\mathcal{U}^{[\square]}\mathcal{U}^{[+]}$	$\frac{\text{Tr}\mathcal{U}^{[\square]}}{N_c}\mathcal{U}^{[+]}$

$\mathcal{F}_{C_1 C_2}$	$\mathcal{F}_{qg}^{(1)}$	$\mathcal{F}_{qg}^{(2)}$
\mathcal{U}_{C_1}	$\mathcal{U}^{[-]\dagger}$	$\mathcal{U}^{[+]\dagger}$
\mathcal{U}_{C_2}	$\mathcal{U}^{[+]}$	$\frac{\text{Tr}\mathcal{U}^{[\square]}}{N_c}\mathcal{U}^{[+]}$

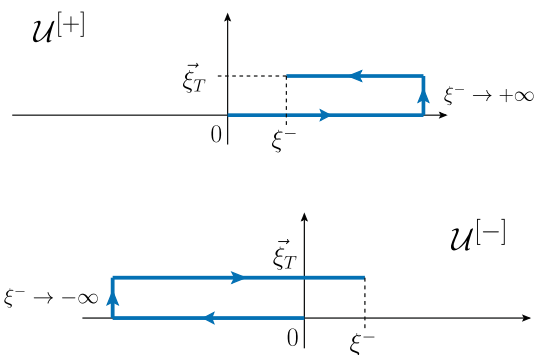


Fig. 5 The shape of the “staple-like” gauge links $\mathcal{U}^{[+]}$ and $\mathcal{U}^{[-]}$. The horizontal axis represents the light-cone minus direction, the vertical axis symbolizes the transverse displacement. The transverse pieces are placed at $+\infty$ and $-\infty$, respectively

$$\frac{d\sigma_{pA \rightarrow qg+X}}{d^2P_T d^2k_T dy_1 dy_2} = \frac{1}{(x_A x_B s)^2} x_B f_{q/B} \times (x_B, \mu^2) \sum_{i=1}^2 \mathcal{F}_{qg}^{(i)}(x_A, |\vec{k}_T|) \mathcal{H}_{qg \rightarrow qg}^{(i)}, \tag{39}$$

where s is the hadronic center of mass energy and $\mathcal{H}_{qg \rightarrow qg}^{(i)}$ are on-shell hard factors corresponding to the two independent color flows. They read

$$\mathcal{H}_{qg \rightarrow qg}^{(1)} = \alpha_s^2 (\hat{u}^2 + \hat{s}^2) \times \left(-\frac{\hat{u}}{2\hat{s}\hat{t}^2} + \frac{1}{2N_c^2} \frac{1}{\hat{s}\hat{u}} \right), \tag{40}$$

$$\mathcal{H}_{qg \rightarrow qg}^{(2)} = \alpha_s^2 (\hat{u}^2 + \hat{s}^2) \times \left(-\frac{\hat{s}}{2\hat{u}\hat{t}^2} \right), \tag{41}$$

where $\hat{s}, \hat{t}, \hat{u}$ are the Mandelstam variables.

In collinear LO factorization, both TMD gluon distributions would be replaced by the collinear gluon PDFs and the

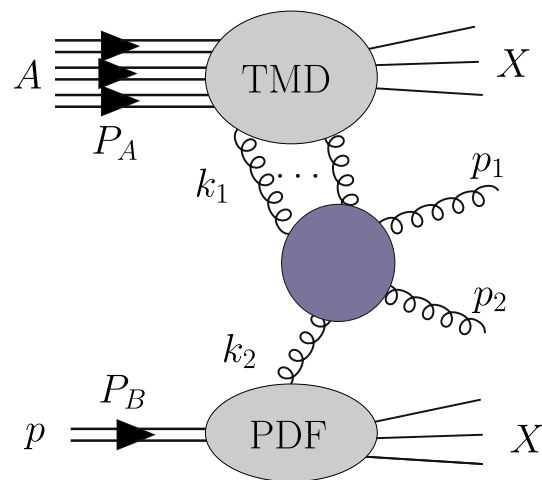


Fig. 6 The ITMD factorization (pure gluon channel) of the p+A dijet cross section into TMD PDF (upper blob), the collinear PDF (lower blob) and the off-shell hard part (center blob). Since the exchanged momentum between the upper blob and the center is off-shell, multiple eikonal gluon exchanges are required to maintain the gauge invariance. In ITMD factorization, these gluons do not increase the genuine twist of the TMD operator. The TMD distribution is given by a certain linear combination of the operators listed in Table 1

above hard factors would be added. It is easy to check that the sum corresponds to the known on-shell hard factor for $qg \rightarrow qg$ process. The list of all hard factors for all subprocesses beyond the large N_c limit is given in [159].

In the end, let us mention progress in establishing the CGC-leading power TMD factorization correspondence. In [166] the Authors explicitly obtained the structure of all TMD operators corresponding to five and six colored parton processes. In [148] the TMD factorization limit was studied for three jet production in CGC. Finally, in [144] the TMD factorization was studied in the context of dijet production in photoproduction at NLO.

4.4 Improved TMD factorization and resummation of kinematic twists

It is important to stress, that the TMD factorization in dilute-dense collisions, despite being leading power, does take into account the gluon saturation, although certain contributions that affect the saturation are neglected. The leading power means here the regime $k_T \ll P_T$, where P_T is related to the transverse momenta of the jets. The saturation scale is taken into account by the leading twist TMD gluon distribution which is considered in the strict high energy limit and undergoes the nonlinear evolution, even at leading twist (for an interesting discussion of two types of saturation see [180]). To summarize, the dilute-dense TMD factorization is suitable when the transverse momenta of dijets are rather large and when we are interested in the back-to-back dijet region. For very large transverse momenta of the jets, the highest scale is not given by the energy but the hard scale and one should switch the framework to the collinear factorization.

The main limitation of the dilute-dense TMD factorization is that it works only in the back-to-back region. In dijet studies, especially at small x , dijet azimuthal correlations are the most important observables and can be measured over a wide range of the azimuthal angle. Therefore, it is essential to account not only for jet correlations but also decorrelations. A related issue is that of the transverse momentum conservation. In the TMD factorization, the transverse momentum k_T of the gluon scattered (or extracted) from the target nucleus enters only TMD gluon distributions, and not the hard process. This complicates for example Monte Carlo realization of such an approach.

It turns out, that, in practical terms, it is actually quite easy to improve the dilute-dense TMD factorization. The hard factors have to take into account power corrections due to the transverse momentum of the incoming gluon. This is uniquely realized in the high energy limit by promoting the on-shell hard factors to the gauge invariant off-shell ones, following the rules described in the part devoted to HEF. This procedure was described in detail in [34], where also off-shell gauge invariant hard factors are calculated for all channels and color flows. A proof and proper interpretation within the CGC was later given in [181]. First, a formal distinction between kinematic and genuine twist is made. The genuine twist counting can be simply understood as counting gluon operators in the TMD matrix element (but not the Wilson lines), for example, an operator with two strength field tensors corresponds to twist two and two-body contribution. The kinematic twists are power corrections in k_T to the n -body process and come from the hard matrix element. In [181] a resummation of the kinematic twists was performed for the two-body contributions, showing that the resulting hard factors indeed correspond to the off-shell gauge invariant hard factors.

Before we review the dilute-dense improved TMD (ITMD) factorization framework, let us first comment, that when determining the TMD gluon distribution functions it is important to work with gauge invariant subset of diagrams and not the individual ones. The systematic way of doing that in small- x physics was suggested in [159], where a decomposition of an amplitude into color-ordered amplitudes was used. The color-ordered amplitudes [182] are gauge invariant, but contain only planar diagrams and correspond to the different ordering of the external partons. Each color-ordered amplitude comes with a color structure, for which the TMD operator can be determined. It is then usually given as some combination of the basic operators build from $U^{[\pm]}$ Wilson lines, but corresponds to the gauge invariant hard factor. The ITMD framework given below was formulated with that feature in mind.

The ITMD factorization formula, accounting for all channels (Fig. 6), reads

$$\frac{d\sigma_{pA \rightarrow JJ+X}}{d^2P_T d^2k_T dy_1 dy_2} = \frac{\alpha_s^2}{(x_A x_B s)^2} \sum_{a,c,d} x_B f_{a/B}(x_B, \mu^2) \times \sum_{i=1}^2 K_{ag^* \rightarrow cd}^{(i)}(\vec{k}_T) \Phi_{ag \rightarrow cd}^{(i)}(x_A, |\vec{k}_T|) \frac{1}{1 + \delta_{cd}} \quad (42)$$

where $K_{ag^* \rightarrow cd}^{(i)}(\vec{k}_T)$ are off-shell gauge invariant hard factors and $\Phi_{ag \rightarrow cd}^{(i)}(x_A, |\vec{k}_T|)$ are the corresponding TMD gluon distributions. We collect them in Table 2. They are expressed in terms of the ordinary Mandelstam variables, as well as “modified” Mandelstam variables. The former read explicitly

$$\hat{s} = (k_1 + k_2)^2 = (p_1 + p_2)^2 = \frac{|\vec{P}_T|^2}{z(1-z)}, \quad (43a)$$

$$\hat{t} = (p_2 - k_1)^2 = (p_1 - k_2)^2 = -\frac{|\vec{p}_{2T}|^2}{1-z}, \quad (43b)$$

$$\hat{u} = (p_1 - k_1)^2 = (p_2 - k_2)^2 = -\frac{|\vec{p}_{1T}|^2}{z}, \quad (43c)$$

where the incoming momenta are

$$k_1 = x_A P_A + k_T, \quad k_2 = x_B P_B \quad (44)$$

and

$$z = \frac{p_1^+}{p_1^+ + p_2^+} \quad \text{and} \quad \vec{P}_T = (1-z)\vec{p}_{1T} - z\vec{p}_{2T}. \quad (45)$$

They sum up to $\hat{s} + \hat{t} + \hat{u} = -|\vec{k}_T|^2$. The “modified” Mandelstam variables take into account only the longitudinal component of the off-shell initial state k_1 and read

$$\bar{s} = (x_A P_A + k_2)^2 = \frac{|\vec{P}_T|^2}{z(1-z)} + |\vec{k}_T|^2 = x_A x_B s, \quad (46a)$$

Table 2 The top table lists the combinations of the TMD gluon distributions listed in Table 1 that correspond to gauge invariant off-shell hard factors of the ITMD factorization formula. The bottom table gives explicit formulae for the LO off-shell gauge invariant hard factors of the ITMD factorization. The \hat{s} , \hat{t} and \hat{u} are ordinary Mandelstam variables, whereas \bar{s} , \bar{t} , \bar{u} are invariants where instead of the incoming off-shell gluon momentum its longitudinal component is used

i	1	2
$\Phi_{gg^* \rightarrow gg}^{(i)}$	$\frac{1}{2N_c^2} (N_c^2 \mathcal{F}_{gg}^{(1)} - 2\mathcal{F}_{gg}^{(3)} + \mathcal{F}_{gg}^{(4)} + \mathcal{F}_{gg}^{(5)} + N_c^2 \mathcal{F}_{gg}^{(6)})$	$\frac{1}{N_c^2} (N_c^2 \mathcal{F}_{gg}^{(2)} - 2\mathcal{F}_{gg}^{(3)} + \mathcal{F}_{gg}^{(4)} + \mathcal{F}_{gg}^{(5)} + N_c^2 \mathcal{F}_{gg}^{(6)})$
$\Phi_{gg^* \rightarrow q\bar{q}}^{(i)}$	$\frac{1}{N_c^2 - 1} (N_c^2 \mathcal{F}_{gg}^{(1)} - \mathcal{F}_{gg}^{(3)})$	$-\mathcal{F}_{gg}^{(2)} + \mathcal{F}_{gg}^{(3)}$
$\Phi_{qg^* \rightarrow qg}^{(i)}$	$\mathcal{F}_{qg}^{(1)}$	$\frac{1}{N_c^2 - 1} (-\mathcal{F}_{qg}^{(1)} + N_c^2 \mathcal{F}_{qg}^{(2)})$
$K_{gg^* \rightarrow gg}^{(i)}$	$\frac{N_c}{C_F} \frac{(\bar{s}^4 + \bar{t}^4 + \bar{u}^4)(\bar{u}\hat{u} + \bar{t}\hat{t})}{\bar{t}\bar{u}\hat{u}\hat{s}\hat{s}}$	$-\frac{N_c}{2C_F} \frac{(\bar{s}^4 + \bar{t}^4 + \bar{u}^4)(\bar{u}\hat{u} + \bar{t}\hat{t} - \bar{s}\hat{s})}{\bar{t}\bar{u}\hat{u}\hat{s}\hat{s}}$
$K_{gg^* \rightarrow q\bar{q}}^{(i)}$	$\frac{1}{2N_c} \frac{(\bar{t}^2 + \bar{u}^2)(\bar{u}\hat{u} + \bar{t}\hat{t})}{\bar{s}\bar{t}\hat{u}}$	$\frac{1}{4N_c^2 C_F} \frac{(\bar{t}^2 + \bar{u}^2)(\bar{u}\hat{u} + \bar{t}\hat{t} - \bar{s}\hat{s})}{\bar{s}\bar{t}\hat{u}}$
$K_{qg^* \rightarrow qg}^{(i)}$	$-\frac{\bar{u}(\bar{s}^2 + \bar{u}^2)}{2\bar{t}\hat{s}} \left(1 + \frac{\bar{s}\hat{s} - \bar{t}\hat{t}}{N_c^2 \bar{u}\hat{u}}\right)$	$-\frac{C_F}{N_c} \frac{\bar{s}(\bar{s}^2 + \bar{u}^2)}{\bar{t}\hat{u}}$

$$\bar{t} = (p_2 - x_A P_A)^2 = -z\bar{s}, \tag{46b}$$

$$\bar{u} = (p_1 - x_A P_A)^2 = -(1 - z)\bar{s}, \tag{46c}$$

which are related via the equation

$$\bar{s} + \bar{t} + \bar{u} = 0. \tag{47}$$

The ITMD factorization was also investigated for other processes than dijets in proton–nucleus collisions. In [183] heavy quark pair production was studied and the problem of longitudinal gluons was discussed in depth. In [184] the effect of the genuine twists vs kinematic twists was studied in detail for dijets in DIS. Finally, neglecting the longitudinal gluon contribution, the ITMD framework was formulated and applied to the trijet production [166, 185].

5 ITMD with the Monte Carlo tool KATIE

KATIE [186] is a parton-level Monte Carlo event generator that can deal with space-like initial-state partons for arbitrary tree-level processes within the Standard Model. This means that it can be provided with k_T -dependent PDFs and that it will automatically calculate the necessary matrix elements with space-like initial-state partons to create parton-level event files. These event files can be chosen to be in the LHEF-format [187]. The k_T -dependent PDFs can be provided via TMDlib [188], or via independent grid files, which however must be in a specific format. Furthermore, KATIE can perform calculations within ITMD factorization, and automatically calculates the necessary gauge invariant matrix elements corresponding to the color structures associated with the several gluon distributions that appear in this factorization scheme. While KATIE primarily creates event files, it also provides tools to create histograms of differential distributions.

KATIE can be downloaded from <https://bitbucket.org/penalty-\@Mhameren/katie/downloads/define> the following Fourier transforms, and a description of use is provided in

the manual there. Here, we provide some background on the Monte Carlo method it employs, elucidating the procedures to be followed when using KATIE.

In hybrid factorization like ITMD factorization, the cross section can be written as a $3n$ -dimensional integral

$$\sigma = \int d^{3n}\omega F(\omega), \tag{48}$$

where n is the number of final-state momenta. There are 4 initial-state variables and $3n - 4$ final-state variables. For hadro-production of dijets at tree-level the number $n = 2$. The function F includes the collinear PDF, the TMDs, the flux factor, and the hard matrix elements. Given a probability density $G(\omega)$ in the integration space (or *phase space*) that is non-zero whenever $F(\omega)$ is non-zero, we can write

$$\sigma = \int d^{3n}\omega G(\omega) \frac{F(\omega)}{G(\omega)}. \tag{49}$$

The Monte Carlo method is based on the Central Limit Theorem, which dictates that if $\{\omega_1, \omega_2, \dots, \omega_N\}$ is a sequence of random phase space points, or *events*, independently drawn from density $G(\omega)$, then

$$\frac{1}{N} \sum_{i=1}^N \frac{F(\omega_i)}{G(\omega_i)} = \sigma + \mathcal{O}\left(\frac{1}{\sqrt{N}}\right). \tag{50}$$

Clearly, the approximation converges to the correct result faster if the fluctuation over the terms in the sum is smaller, with the optimum when $G(\omega) = F(\omega)/\sigma$. Successfully applying the Monte Carlo method means that one solves the problem of bringing $G(\omega)$ to this optimum to a satisfactory degree. Reaching the optimum implies having solved the integration problem and eliminates the need for the Monte Carlo procedure. Satisfaction means that the result can be obtained within an acceptable time, and in practice means finding a compromise between the number of terms needed,

and the complexity of the algorithm to produce the sequence of events.

An advantage of the Monte Carlo method is that, given a “satisfactory” sequence *generator* to calculate the cross section σ , it can also be used to estimate differential distributions. Let $\varphi(\omega)$ be an observable, and $b_j(\varphi) = \theta(\varphi - \varphi_j)\theta(\varphi_{j+1} - \varphi)$ be a bin for this observable between values $[\varphi_j, \varphi_{j+1}]$, then

$$\frac{1}{N} \sum_{i=1}^N \frac{F(\omega_i)}{G(\omega_i)} b_j(\varphi(\omega_i)) = \int_{\varphi_j}^{\varphi_{j+1}} d\varphi \frac{d\sigma}{d\varphi} + \mathcal{O}\left(\frac{1}{\sqrt{N}}\right). \quad (51)$$

The idea of an *event file* is to store events ω_i and their *weight* $W_i = F(\omega_i)/G(\omega_i)$ to produce arbitrary distributions without having to redo the generation of events.

In the context of the foregoing, KATIE performs roughly speaking two tasks: it calculates the hard matrix elements, automatically and efficiently, as part of the evaluation of $F(\omega)$, and, provided with PDFs and TMDs, it creates reasonably-sized event files. In order to perform the first task, KATIE employs the Dyson–Schwinger approach to calculate tree-level helicity amplitudes numerically, as first proposed in [189] and also utilized in other tree-level programs, notably ALPGEN [190]. The feature of space-like initial-state momenta is dealt with following the auxiliary-parton method outlined in [155]. The second task is achieved through the application of many well-known optimization techniques, a few of which are worth mentioning in order to understand the procedures in KATIE’s operation.

One is *adaptive importance sampling*, which optimizes adaptable probability densities iteratively, using the information of events generated so far in each iterative step. While being very effective, it can cause bias in those events, and they must not be used for the actual event file. Consequently, there must be a separate optimization stage before the generation of the event file starts. This happens for each partonic subprocess separately. Once this has been performed, the information of the optimized densities is stored, and is from then on used to generate an arbitrary number of event files.

Secondly, KATIE employs *rejection*. Phase space cuts are required to mimic detector acceptance and to avoid singularities in tree-level matrix elements. These typically are formulated in terms of variables that are non-trivial functions of the variables in ω that are actually generated, and cannot be implemented as exact integration bounds. Instead, the integrand $F(\omega)$ is imagined to vanish outside those phase space cuts, and a bigger enveloping space is generated. This leads to many events with $W_i = 0$, which are however not stored but are included in the eventual normalization of the weights. In order to achieve the unbiased normalization of the event weights in case several event files are generated, so called *raw* files are stored instead of actual event files, containing non-

normalized weights and more statistical information. Event files in the LHF format can be extracted from these.

The third method that needs to be mentioned is *unweighting*. This is a statistical procedure to reduce the fluctuations of the weights W_i while keeping the event file sound. In practice this procedure “weeds out” low-weight events and reweights remaining ones. The cross section estimate is not affected (is also not getting better) but it allows to reduce the required size of the event file. While it causes many events to get the same constant weight, there may occur events with higher weights.

The phase space is only $3n$ -dimensional, but it is much more convenient to write the events in terms of the $4(n + 2)$ variables being the parton-level initial-state and final-state momenta. We will still denote events with the symbol ω . While all components of $F(\omega_i)$, like the matrix element, the PDFs, the strong coupling etc., can be re-evaluated using these, it is more convenient to also store their values besides W_i . This is useful if one wants to employ the *reweighting* procedure. For example, let an event file be created within hybrid k_T -factorization with a TMD $\mathcal{F}(\omega)$ (we simply imply that this function selects the appropriate variables from ω . Realize that this in practice includes the final-state ones due to the factorization scale dependence). Suppose a user has their own TMD \mathcal{F}' but only in a numerical form that cannot (yet) be married with KATIE or TMDlib. The value of $\mathcal{F}_i = \mathcal{F}(\omega_i)$ is stored for each event, and the event file can be transformed to be valid for \mathcal{F}' by multiplying

$$W_i \rightarrow W_i \frac{\mathcal{F}'(\omega_i)}{\mathcal{F}_i} \quad (52)$$

for each event. It will increase the fluctuation of the weights and reduce the quality of the event file, but most likely not in a drastic way.

As mentioned earlier, the use of KATIE is described in the manual, but below we present the complete single input card that allows to create event files for dijets within ITMD.

```
# Only QCD interaction, QED and Weak are on by
default switch = withQCD Yes
switch = withQED No
switch = withWeak No
# List of processes
process = g g -> g g , factor = 1
process = g g -> u u~ , factor = Nf
process = u g -> g u , factor = 1
process = d g -> g d , factor = 1
process = s g -> g s , factor = 1
process = c g -> g c , factor = 1
process = b g -> g b , factor = 1
# In the process definition B A -> 1 2..., put
initial state A off-shell
offshell = 0 1
itmdf = yes
# Collinear pdf set
lhaSet = CT10nlo
```

```
# Example directory and filenames below
tmdTableDir = /home/user/projects/TMDs/
tmdpdf = gg1 myGridFile-Fgg1.dat
tmdpdf = gg2 myGridFile-Fgg2.dat
tmdpdf = gg1 myGridFile-Fgg1.dat
tmdpdf = gg2 myGridFile-Fgg2.dat
tmdpdf = gg6 myGridFile-Fgg6.dat
Nflavors = 5
# Number of non-zero weight events to be spent
on optimization
Noptim = 100,000
# Summing squared helicity amplitudes is more
efficient in number of
# events (less fluctuation), but slower in time
than sampling.
helicity = sum
# Center-of-mass (CM) energy, events will be in
CM frame.
Ecm = 8160
# Jet definition, 1 and 2 refer to the final-
state momenta
cut = {deltaR|1,2|} > 0.4
# {pT|1|} is the pT of final-state number 1
# {pT|1|,2|} is the hardest of the pTs of
final-state number 1 and 2
cut = {pT|1|,2|} > 28
cut = {pT|1|,2|} < 35
cut = {pT|2|,1,2|} > 28
cut = {pT|2|,1,2|} < 35
# In the process definition B A -> 1 2...,
# initial-state A has equal-sign energy and
z-component,
# while initial-state B has opposite-sign.
# The off-shell initial-state A has lower x
than B,
# so the final state is boosted towards
negative rapidity.
cut = {rapidity|1|} > -4.0
cut = {rapidity|2|} > -4.0
cut = {rapidity|1|} < -2.7
cut = {rapidity|2|} < -2.7
# Renormalization/factorization scale
scale = ({pT|1|}+{pT|2|})/2
```

6 Gluon densities saturation and Sudakov form factor

6.1 BK equation for dipole gluon density

From the BK equation discussed in the earlier sections, one can obtain TMD dipole gluon density. The steps outlined below will closely follow the results obtained in [60, 85, 191].

In this section, we will use $k^2 = |\vec{k}_T|^2$ as an argument of gluon density. This is the standard notation used in the discussion of angular averaged distributions.

Let's define the following Fourier transforms [191, 192]

$$\begin{aligned} \mathcal{F}(x, k^2) &= \frac{N_c}{\alpha_s(2\pi)^3} \int d^2b \int d^2r e^{ik \cdot r} \nabla_r^2 N(r, b, x), \\ &\times \Phi(x, k^2) \\ &= \frac{1}{2\pi} \int d^2b \int \frac{d^2r}{r^2} e^{ik \cdot r} N(r, b, x) \end{aligned} \quad (53)$$

The function $\mathcal{F}(x, k^2)$ is the dipole gluon density already introduced in the previous sections. The function $\Phi(x, k^2)$ is an auxiliary quantity for which the BK equation has a simple form with local nonlinear term as will be shown below.

The explicit relation between the two functions $\mathcal{F}(x, k^2)$ and $\Phi(x, k^2)$ is

$$\begin{aligned} \mathcal{F}(x, k^2) &= \frac{N_c}{4\alpha_s\pi^2} k^2 \nabla_k^2 \Phi(x, k^2), \quad \Phi(x, k^2) = \frac{\alpha_s\pi^2}{N_c} \\ &\times \int_{k^2}^{\infty} \frac{dl^2}{l^2} \ln \frac{l^2}{k^2} \mathcal{F}(x, l^2). \end{aligned} \quad (54)$$

It has been shown in [85] that once one considers homogeneous infinite nucleus the b integral on the formula 53 can be factorized and enters only via initial condition

$$\begin{aligned} \Phi(x, k^2) &= \frac{1}{2\pi} \int d^2b \int \frac{d^2r}{r^2} e^{ik \cdot r} N(r, b, x) = \frac{1}{2\pi} \int d^2b \\ &\times \int \frac{d^2r}{r^2} e^{ik \cdot r} N(r, x) = \int d^2b \Phi_b(x, k^2) \end{aligned} \quad (55)$$

and one gets the following BK equation

$$\begin{aligned} \Phi_b(x, k^2) &= \Phi_{0b}(x, k^2) + \bar{\alpha}_s \int_{x/x_0}^1 \frac{dz}{z} \\ &\times \int_0^{\infty} \frac{dl^2}{l^2} \left[\frac{l^2 \Phi_b(x/z, l^2) - k^2 \Phi_b(x/z, k^2)}{|k^2 - l^2|} \right. \\ &\left. + \frac{k^2 \Phi_b(x/z, k^2)}{\sqrt{(4l^4 + k^4)}} \right] \\ &- \bar{\alpha}_s \int_{x/x_0}^1 \frac{dz}{z} \Phi_b^2(x/z, k^2). \end{aligned} \quad (56)$$

In the equation above, the impact parameter is not a dynamic quantity. On top of that it does not describe physics at large distances correctly as it does not take into account confinement effects [193]. Taking the above into account in order to obtain the integrated over impact parameter gluon density one needs to assume some impact parameter dependence since one needs to perform the integration over it to calculate gluon density. For cylinder like target, one may use the following ansatz for factorization [191]

$$\Phi_b(x, k^2) = \Phi(x, k^2) S(b) \quad (57)$$

with normalization conditions

$$\int d^2\mathbf{b} S(b) = 1, \quad \int d^2\mathbf{b} S^2(b) = \frac{1}{\pi R^2} \quad (58)$$

where $S(b)$ is the profile function $S(b) = \theta(R - b)/\pi R^2$.

The momentum space equation for the integrated over impact parameter dependence $\Phi(x, k^2)$ assumes the form:

$$\Phi(x, k^2) = \Phi_0(x, k^2) + \bar{\alpha}_s \int_{x/x_0}^1 \frac{dz}{z}$$

$$\begin{aligned} & \times \int_0^\infty \frac{dl^2}{l^2} \left[\frac{l^2 \Phi(x/z, l^2) - k^2 \Phi(x/z, k^2)}{|k^2 - l^2|} \right. \\ & \left. + \frac{k^2 \Phi(x/z, k^2)}{\sqrt{(4l^4 + k^4)}} \right] \\ & - \frac{\bar{\alpha}_s}{\pi R^2} \int_{x/x_0}^1 \frac{dz}{z} \Phi^2(x/z, k^2). \end{aligned} \tag{59}$$

where $\bar{\alpha} = N_c \alpha_s / \pi$.

The the equation for $\mathcal{F}(x, k^2)$ is obtained from Eq. (59) by inserting in the nonlinear part of it relation expressing $\Phi(x, k^2)$ in terms of $\mathcal{F}(x, k^2)$ and acting on the whole equation with the operator that transforms $\Phi(x, k^2)$ to $\mathcal{F}(x, k^2)$ see [191] for the details of this transformations. In the end one obtains [60, 191, 194]

$$\begin{aligned} \mathcal{F}(x, k^2) &= \mathcal{F}_0(x, k^2) + \bar{\alpha}_s \int_{x/x_0}^1 \frac{dz}{z} \int_0^\infty \frac{dl^2}{l^2} \\ & \times \left[\frac{l^2 \mathcal{F}(x/z, l^2) - k^2 \mathcal{F}(x/z, k^2)}{|k^2 - l^2|} + \frac{k^2 \mathcal{F}(x/z, k^2)}{\sqrt{(4l^4 + k^4)}} \right] \\ & - \frac{2\alpha_s^2 \pi}{N_c R^2} \int_{x/x_0}^1 \frac{dz}{z} \\ & \times \left\{ \left[\int_{k^2}^\infty \frac{dl^2}{l^2} \mathcal{F}(x/z, l^2) \right]^2 \right. \\ & \left. + \mathcal{F}(x/z, k^2) \int_{k^2}^\infty \frac{dl^2}{l^2} \ln \left(\frac{l^2}{k^2} \right) \mathcal{F}(x/z, l^2) \right\}. \end{aligned} \tag{60}$$

The linear part of the equation above is the well known BFKL kernel while the nonlinear part is the triple pomeron vertex. The triple pomeron vertex has such property that it is dominated by the anticollinear pole. We see that as one evaluates the gluon at lower and lower values of k^2 the integration in the nonlinear term is over a larger domain giving a larger contribution and suppressing the gluon density. One can also see that in the collinear limit, the nonlinear term completely drops and one is left with a linear equation.

$$\begin{aligned} \mathcal{F}(x, k^2) &= \mathcal{F}^{(0)}(x, k^2) + \bar{\alpha}_s \int_{x/x_0}^1 \frac{dz}{z} \\ & \times \int_{k_0^2}^{k^2} dk'^2 \frac{\mathcal{F}(x/z, k'^2)}{k^2}. \end{aligned} \tag{61}$$

6.2 BK equation within Kwiecinski Martin Staśto model

The (60) is a leading order BK equation for dipole gluon density. So far there is no direct momentum space extension of the equation beyond LO approximation. It is known that higher-order corrections slow down the rapid growth of gluon density and are relevant for phenomenology. Therefore in order to make it applicable to phenomenology it has been extended to account for higher order corrections fol-

lowing Kwiecinski–Martin–Stasto (KMS) model [195] that was originally applied to the BFKL equation. Those include

- kinematical constraints which enforce that the virtuality of the exchanged gluon is dominated by its transverse component $k^2 = |\vec{k}_T|^2$. This constraint suppresses the anticollinear pole and therefore suppresses the diffusion into the infrared. Furthermore, this contribution can be shown to account for resummation of collinear logs
- nonsingular at small z pieces of the splitting function in order to be consistent in the collinear limit with the DGLAP system of equations in the collinear limit
- running coupling constant
- sea quark singlet contribution to match the DGLAP limit at large z

With these corrections, the equation assumes the form [191]

$$\begin{aligned} \mathcal{F}(x, k^2) &= \mathcal{F}_0(x, k^2) \\ & + \frac{\alpha_s(k^2) N_c}{\pi} \int_{x/x_0}^1 \frac{dz}{z} \\ & \times \int_{k_0^2}^\infty \frac{dl^2}{l^2} \left\{ \frac{l^2 \mathcal{F}\left(\frac{x}{z}, l^2\right) \theta\left(\frac{k^2}{z} - l^2\right) - k^2 \mathcal{F}\left(\frac{x}{z}, k^2\right)}{|l^2 - k^2|} \right. \\ & \left. + \frac{k^2 \mathcal{F}\left(\frac{x}{z}, k^2\right)}{\sqrt{4l^4 + k^4}} \right\} \\ & + \frac{\alpha_s(k^2)}{2\pi k^2} \int_{x/x_0}^1 dz \left\{ \left(P_{gg}(z) - \frac{2N_c}{z} \right) \right. \\ & \times \int_{k_0^2}^{k^2} dl^2 \mathcal{F}\left(\frac{x}{z}, l^2\right) + z P_{gq}(z) \Sigma\left(\frac{x}{z}, k^2\right) \left. \right\} \\ & - \frac{2\pi \alpha_s^2(k^2)}{N_c R^2} \left\{ \left[\int_{k^2}^\infty \frac{dl^2}{l^2} \mathcal{F}(x, l^2) \right]^2 \right. \\ & \left. + \mathcal{F}(x, k^2) \int_{k^2}^\infty \frac{dl^2}{l^2} \ln\left(\frac{l^2}{k^2}\right) \mathcal{F}(x, l^2) \right\}, \end{aligned} \tag{62}$$

where $\Sigma(x, k^2)$ is a sea quark distribution obeying essentially DGLAP equation in unintegrated form (further details can be found in [191]). Please note that in the equation above lower cut in $k^2 = k_0^2$ was introduced. The origin of the cut is related to the method of solving of the equation and in principle can be set to an arbitrarily small value.

In Ref. [12], the following initial condition for Eq. (62) was fitted to the F_2 proton structure data from HERA [196]

$$\mathcal{F}_0(x, k^2) = \frac{\alpha_s(k^2)}{2\pi k^2} \int_x^1 dz P_{gg}(z) \frac{x}{z} g\left(\frac{x}{z}, k_0^2\right), \tag{63}$$

with

$$xg(x) = N(1-x)^\beta(1-xD). \tag{64}$$

For $k^2 \leq 1 \text{ GeV}^2$, the gluon distribution was taken as $\mathcal{F}(x, k^2) = k^2 \mathcal{F}(x, 1)$, which is motivated by the shape obtained from the solution of the LO BK equation in the saturation regime [197].

The fitting procedure gave the following numerical values for the parameters: $N = 0.94$, $\beta = 18.6$, $D = -82.1$ and $R = 2.40 \text{ GeV}^{-1}$. The overall quality of the fit was good, with $\chi^2/\text{ndof} = 1.73$. We shall refer to this gluon distribution as the Kutak-Sapeta or KS gluon.

For completeness, the fit of a linearized version of Eq. (62), i.e. with the last term dropped, was performed as well, and the following parameters were obtained: $N = 0.004$, $\beta = 26.7$, $D = -51102$ and $\chi^2/\text{ndof} = 3.86$. The presence of the parameter R , characterizing the target, allows one to obtain the dipole gluon distribution of nuclei. In order to do that, one uses relation $R_A = d A^{1/3} R$, which in the end gives the enhancement by $A^{1/3}$ of the nonlinear term for gluon density normalized to the number of nucleons [12]. The parameter d is a phenomenological factor that was varied between $d = 0.5$ and $d = 1.0$. In the following computations, we used the “least saturation” scenario with $d = 0.5$.

6.3 The Sudakov resummation

An important class of perturbative corrections to the scattering process, appearing when the emitted partons are both collinear and soft, is resummed in terms of the Sudakov form factor. It appears due to not exact cancellation of virtual corrections and real corrections, as a consequence of certain exclusivity of the final state. The Sudakov resummation is used to formulate DGLAP evolution equations in unintegrated form [198–200] and in Monte Carlo simulations [201]. In the latter application, it leads to finite transverse momentum even in the absence of any other mechanism generating transverse momentum. Finally, it is also independent of any saturation effects.

In the processes considered here the largest effect of the Sudakov is expected to affect the cross section when the jets are in a nearly back-to-back configuration. The large logarithm appears because the transverse momenta of jets can be sizable while the imbalance k_T of incoming space-like parton is small. The effect of the Sudakov form factor is to suppress the back-to-back configuration and enhance the moderate angle part of the distribution, leading to so-called broadening. Within the small- x formalism, the Sudakov form factor can be factorized at one loop level, in the coordinate space, from the hard process [202–204]. The complete cross-section accounting for the Sudakov form factor reads:

$$\frac{d\sigma^{\text{pA} \rightarrow j_1 j_2 + X}}{d^2 P_T d^2 k_T dy_1 dy_2} = \sum_{a,c,d} x_p \sum_{i=1}^2 \mathcal{K}_{ag^* \rightarrow cd}^{(i)}(P_T, k_T; \mu) \times \int db_T b_T J_0(b_T k_T) f_{a/p}(x_p, \mu_b) \tilde{\Phi}_{ag \rightarrow cd}^{(i)} \times (x_A, b_T) e^{-S^{ag \rightarrow cd}(\mu, b_T)}, \tag{65}$$

where $\tilde{\Phi}_{ag \rightarrow cd}^{(i)}$ is the Fourier transform of the TMD gluon distributions and $S^{ag \rightarrow cd}$ are the Sudakov factors written for each channel

$$S^{ab \rightarrow cd}(\mu, b_T) = \sum_{i=a,b,c,d} S_p^i(\mu, b_T) + \sum_{i=a,c,d} S_{np}^i(\mu, b_T), \tag{66}$$

where S_p^i and S_{np}^i are the perturbative and non-perturbative contributions. The perturbative Sudakov factors, including double and single logarithms, are given by [202, 205]

$$S_p^{qg \rightarrow qg}(\mu, b_T) = \int_{\mu_b^2}^{\mu^2} \frac{dq_T^2}{q_T^2} \left[2(C_F + C_A) \frac{\alpha_s}{2\pi} \ln \left(\frac{\mu^2}{q_T^2} \right) - \left(\frac{3}{2} C_F + C_A \beta_0 \right) \frac{\alpha_s}{\pi} \right], \tag{67}$$

$$S_p^{gg \rightarrow gg}(\mu, b_T) = \int_{\mu_b^2}^{\mu^2} \frac{dq_T^2}{q_T^2} \times \left[4C_A \frac{\alpha_s}{2\pi} \ln \left(\frac{\mu^2}{q_T^2} \right) - 3C_A \beta_0 \frac{\alpha_s}{\pi} \right], \tag{68}$$

where $\beta_0 = (11 - 2n_f/N_c)/12$. The $gg \rightarrow q\bar{q}$ channel is negligible in the kinematic domain considered here. In the above the scale μ_b is the inverse of the impact parameter:

$$\mu_b = 2e^{-\gamma_E} / b_*, \tag{69}$$

with

$$b_* = b_T / \sqrt{1 + b_T^2 / b_{\text{max}}^2}. \tag{70}$$

Given this selection, the scale μ_b becomes constant at the point of high b_T , where its value is determined to be $2e^{-\gamma_E} / b_{\text{max}}$, which is considerably greater than Λ_{QCD} . Following Ref. [206], we will adopt $b_{\text{max}} = 0.5, \text{ GeV}^{-1}$.

For completeness, we comment briefly on DGLAP based prescriptions for incorporating the Sudakov form factor. The method relies on constructing the Sudakov form factor from the DGLAP splitting function and using it to reshuffle events according to the relation between hard scale and transverse momentum of the gluon. In such constructions, one chooses some inclusive quantity to be unmodified while allowing for modification of unintegrated quantity. Two such methods were presented in [24, 27]. In the former, the total cross

section was preserved while in the latter the integrated gluon density was unmodified.

6.4 Kutak–Sapeta (KS) gluon distribution

We shall now discuss the KS gluon, introduced above, in variants with and without the Sudakov resummation. The parameters were fixed by the original fit [12] with no Sudakov factors and the gluon was later used without any modifications. Hence, combining it with the Sudakov does not introduce new parameters. This is true because the perturbative part (67) and (68) is parameter-free while the non-perturbative terms are universal in the kinematic domain of our study [207].

We introduce the Sudakov effects into the KS gluon distribution following the formalism described above. In addition, for reference, we use two methods employed in our earlier studies [24, 27]. Those calculations used the Sudakov form factor, understood as the DGLAP evolution kernel, that has been applied on the top of the gluon TMD, together with constraints such as unitarity. Those methods should therefore be considered as models, in contrast to the proper resummation of Sudakov logarithms described in the preceding section. Nevertheless, the approaches used in Refs. [24, 27] were phenomenologically successful (see also [14]), and it is therefore useful and interesting to compare the predictions of those simplistic models with the proper way of including the Sudakov effects into the small- x gluon.

The reference models are:

- Model 1: The survival probability model [27], where the Sudakov factor of the form [208]

$$T_s(\mu_F^2, k_T^2) = \exp \left(- \int_{k_T^2}^{\mu_F^2} \frac{dk_T'^2}{k_T'^2} \times \frac{\alpha_s(k_T'^2)}{2\pi} \sum_{a'} \int_0^{1-\Delta} dz' P_{a'a}(z') \right), \quad (71)$$

is imposed at the level of the cross section. This procedure corresponds to performing a DGLAP-type evolution from the scale $\mu_0 \sim k_T$ to μ , decoupled from the small- x evolution.

- Model 2: The model with a hard scale introduced in Ref. [24]. The Sudakov form factor of the same form as in Eq. (71) is imposed on top of the KS gluon distribution in such a way that, after integration of the resulting hard scale dependent gluon TMD, one obtains the same result as by integrating the KS gluon distribution.

In Fig. 7, we show the KS gluon distributions, with and without Sudakov form factors, as functions of the transverse

momentum k_T and the hard scale μ . Three columns correspond to three different x values. The first row shows the original KS gluon distribution, which, as expected, does not depend on the value of μ . In the second row, we show the KS hardscale gluon distribution of Ref. [24] (the other model [27] does not allow one to plot gluon distribution, as it applies Sudakov effects at the cross section level via a reweighting procedure). Here, the dependence on μ is non-trivial and we see that the gluon develops a maximum in that variable. As shown in the figure, this maximum is rather broad. In the third and the fourth row of Fig. 7, we present the KS gluon distribution with the Sudakov form factor from Eqs. (66)–(68). As explained earlier, this gluon exists in two versions, one for the qg and the other for the gg channel. The dependence on k_T and μ is qualitatively similar between these gluons and the naive KS hardscale gluon distribution. In the former case, however, the peak is significantly narrower in μ as compared to the naive model of Ref. [24]. It is interesting to note that the qg gluon is broader than the gg gluon. This can be understood by comparing the colour factors in the Sudakov functions (67) and (68). Since the colour factor for the gg channel is larger than for the qg , the Sudakov suppression is stronger along the μ direction in the former case.

We have as well computed linear versions of the KS gluon distributions with the Sudakov, using the KS linear gluon distribution of Ref. [12]. The gluons discussed in this section are available publicly as part of the `KS` package and can be downloaded from <http://nz42.ifj.edu.pl/~sapeta/KSgluon-2.0.tar.gz>.

6.5 ITMD gluons distributions

In the limit of small x and assuming the mean field approximation, the gluons listed in the table (1) can be expressed in terms of dipole gluon density as [168]

$$\mathcal{F}_{qg}^{(1)}(x, |\vec{k}_T|) = xG^{(2)}(x, |\vec{q}_T|), \quad (72)$$

$$\mathcal{F}_{qg}^{(2)}(x, |\vec{k}_T|) = \int d^2q_T xG^{(1)}(x, |\vec{q}_T|) \times F(x, |\vec{k}_T - \vec{q}_T|), \quad (73)$$

$$\mathcal{F}_{gg}^{(1)}(x, |\vec{k}_T|) = \int d^2q_T xG^{(2)}(x, |\vec{q}_T|) \times F(x, |\vec{k}_T - \vec{q}_T|), \quad (74)$$

$$\mathcal{F}_{gg}^{(2)}(x, |\vec{k}_T|) = - \int d^2q_T \frac{(\vec{k}_T - \vec{q}_T) \cdot \vec{q}_T}{|\vec{q}_T|^2} xG^{(2)}(x, |\vec{q}_T|) \times F(x, |\vec{k}_T - \vec{q}_T|), \quad (75)$$

$$\mathcal{F}_{gg}^{(6)}(x, |\vec{k}_T|) = \int d^2q_T d^2q_T' xG^{(1)}(x, |\vec{q}_T|) \times F(x, |\vec{q}_T'|) F(x, |\vec{k}_T - \vec{q}_T - \vec{q}_T'|). \quad (76)$$

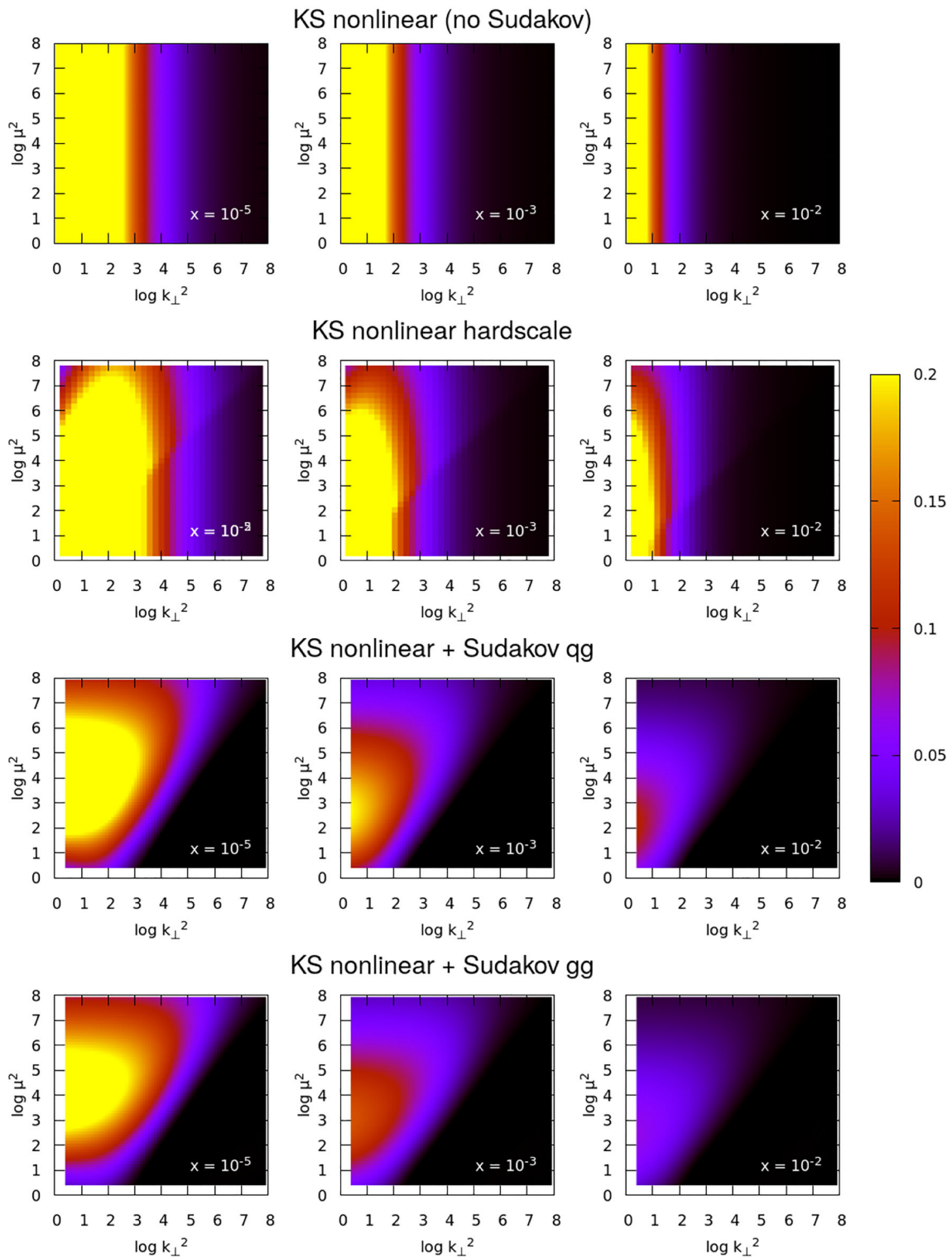


Fig. 7 KS gluon distribution, without and with the Sudakov form factors. The second row corresponds to the simple model-Sudakov given in Eq. (71), while the third and the fourth rows show results obtained with the Sudakov factors derived from QCD and given in Eqs. (66)–(68)

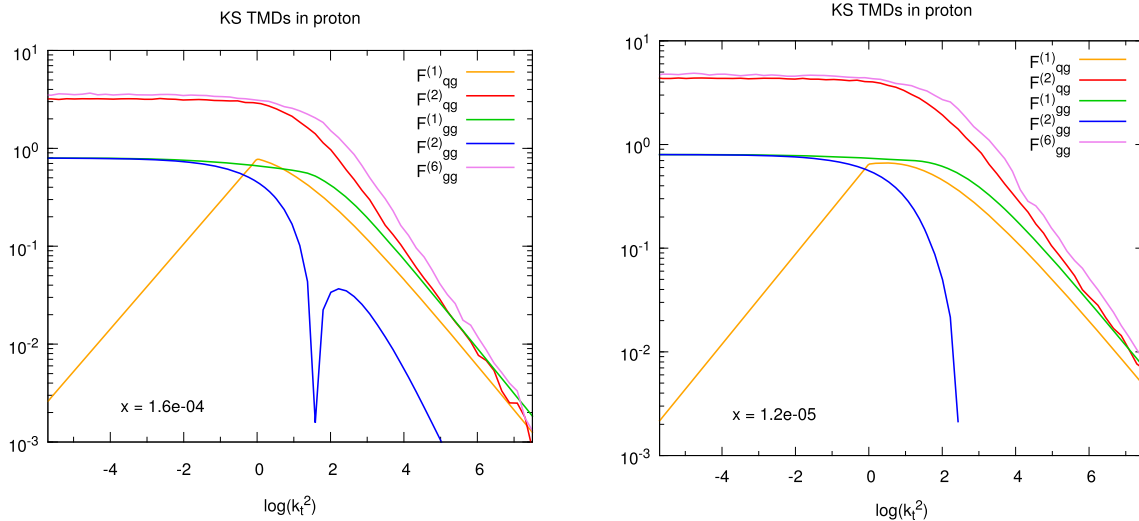


Fig. 8 The KS gluon TMDs as a function of $\log(|\vec{k}_T|^2/\text{GeV}^2)$ at $x = 1.6 \cdot 10^{-4}$ for the proton (left) and the lead nucleus (right). Since $\mathcal{F}_{gg}^{(2)}$ goes negative, its absolute value is shown on the figures

where

$$xG^{(2)}(x, |\vec{k}_T|) = \frac{N_c |\vec{k}_T|^2 S_\perp}{2\pi^2 \alpha_s} F(x, |\vec{k}_T|) \tag{77}$$

and $F(x, |\vec{k}_T|)$ is a Fourier transform of the fundamental dipole

$$F(x, |\vec{k}_T|) = \int \frac{d^2\vec{r}}{(2\pi)^2} e^{-i\vec{k}_T \cdot \vec{r}} \left\langle \text{Tr} \left[U(\vec{r}) U^\dagger(0) \right] \right\rangle_x / N_c, \tag{78}$$

The gluons listed above form a set from which one can construct the gluon densities $\Phi^{(i)}$ entering the ITMD factorization formula (42) as obtained in [34]:

$$\Phi_{qg \rightarrow qg}^{(1)} = \mathcal{F}_{qg}^{(1)}, \quad \Phi_{qg \rightarrow qg}^{(2)} \approx \mathcal{F}_{qg}^{(2)} \tag{79}$$

$$\Phi_{gg \rightarrow q\bar{q}}^{(1)} \approx \mathcal{F}_{gg}^{(1)}, \quad \Phi_{gg \rightarrow q\bar{q}}^{(2)} \approx -N_c^2 \mathcal{F}_{gg}^{(2)} \tag{80}$$

$$\begin{aligned} \Phi_{gg \rightarrow gg}^{(1)} &\approx \frac{1}{2} \left(\mathcal{F}_{gg}^{(1)} + \mathcal{F}_{gg}^{(6)} \right), \\ \Phi_{gg \rightarrow gg}^{(2)} &\approx \mathcal{F}_{gg}^{(2)} + \mathcal{F}_{gg}^{(6)}. \end{aligned} \tag{81}$$

6.6 ITMD distributions from KS gluon

All the gluon TMDs (72)–(76) can be calculated from a single $xG^{(2)}(x, |\vec{k}_T|)$ distribution in the above Gaussian approximation. However, because the KS gluon provides directly an impact-parameter-integrated distribution, it is not straightforward to identify S_\perp and obtain $F(x, |\vec{k}_T|)$ from Eq. (77). To address this issue, we applied the following procedure [209]. We first computed the dipole cross section $\sigma_{\text{dipole}}(x, r = |\mathbf{r}|) = 2 \int d^2b N_F(x, \mathbf{r})$ from $xG^{(2)}(x, |\vec{k}_T|)$ by inverse Fourier transformation of Eq. (78), and then defined S_\perp as

its value at large r , i.e. when it saturates (since in that limit $N_F \rightarrow 1$):

$$\begin{aligned} \frac{1}{2} \sigma_{\text{dipole}}(x, r = \infty) &= S_\perp(x) = \lim_{r \rightarrow \infty} \frac{4\pi^3}{N_c} \alpha_s \\ &\times \int \frac{d|\vec{k}_T|}{|\vec{k}_T|} \left[1 - J_0(r|\vec{k}_T|) \right] xG^{(2)}(x, |\vec{k}_T|). \end{aligned} \tag{82}$$

We can now obtain $F(x, |\vec{k}_T|)$ and calculate all the needed gluon TMDs. Their behavior as a function of $k_t = |\vec{k}_T|$ is plotted in Fig. 8, both for the proton and the lead nucleus. The small mismatch between their high- k_t behavior, expected due to the initial condition for the x evolution, can be observed.

Similarly, we computed [210] the ITMD distributions from the KS gluon with the proper QCD Sudakov, shown in Fig. 7.

Within the Gaussian approximation, one can also derive the following formula for the WW gluon density [209]

$$\begin{aligned} \mathcal{F}_{gg}^{(3)}(x, |\vec{k}_T|) &= \frac{2\pi^2 \alpha_s}{N_c |\vec{k}_T|^2 S_\perp} \frac{1}{2} \int_{|\vec{k}_T|^2} d^2k'_T \ln \frac{|\vec{k}'_T|^2}{|\vec{k}_T|^2} \\ &\int \frac{d^2q_T}{|\vec{q}_T|^2} \mathcal{F}_{qg}^{(1)}(x, |\vec{q}_T|) \mathcal{F}_{qg}^{(1)}(x, |\vec{k}_T - \vec{q}_T|), \end{aligned} \tag{83}$$

where $\mathcal{F}_{qg}^{(1)}$ is the dipole gluon density and S_\perp is the target’s transverse area.

Using the procedure described above, we computed also the WW gluon, which we show in Fig. 9 in proton (left) and lead (right), with and without Sudakov form factors, as functions of the transverse momentum $|\vec{k}_T|$ and the hard scale μ , for one particular $x = 10^{-3}$. (The gluon density is available from the TMDlib [188]).

First of all, let us notice that the WW gluon distribution has no maximum, contrary to the dipole gluon [12,209].

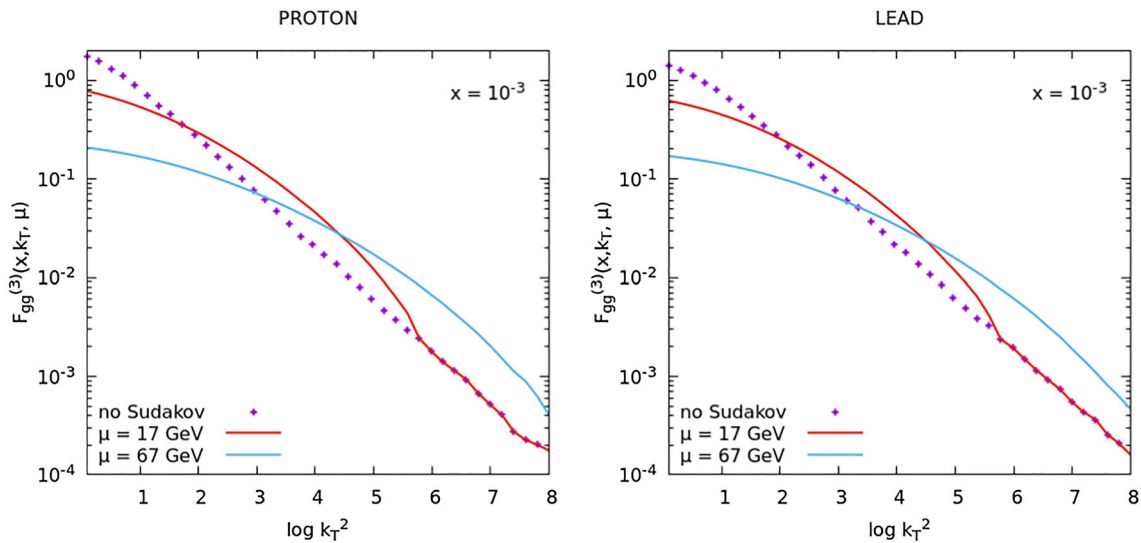


Fig. 9 The WW gluon density in the proton (left) and lead (right), with and without Sudakov resummation, as a function of the transverse momentum of the gluon, for various values of the hard scale

Secondly, we see that the Sudakov factor suppresses the gluon distribution at low $|\vec{k}_T|$ and enhances it at higher $|\vec{k}_T|$. Because the Sudakov form factor is derived in the regime $\mu \propto |\vec{p}_T| \gg |\vec{k}_T|$, we apply it only to that part of the gluon density where $\mu > |\vec{k}_T|$. In the remaining domain, we use the gluon without Sudakov, given in Eq. (83). This is visible in Fig. 9 as a kink of the curve corresponding to $\mu = 17$ GeV. (A similar kink exists also for the $\mu = 67$ GeV curve but it is located at larger values of $\log |\vec{k}_T|^2$).

All the ITMD gluons discussed above are available publicly and can be downloaded from <http://nz42.ifj.edu.pl/~sapeta/itmd-KS.tar.gz>.

7 Phenomenology of forward jets

7.1 Forward dijets at the LHC

In the following section we review some existing predictions for forward dijet production in proton–proton and proton–lead collisions at LHC energies, obtained within the ITMD framework. We also include some new computations, not published before.

Before we proceed, it is important to mention, that the first predictions for forward dijets in saturation formalism using the ITMD, that – as discussed in Sect. 4.4 – approximates the CGC for sufficiently large transverse momenta, appeared in [209]. This computation significantly improved the predictions of [23] obtained with k_T -factorization, which is not entirely accurate at small dijet imbalance. Later, in [211] a full computation within CGC was compared to ITMD, confirming, that at larger transverse momenta ITMD is adequate.

None of the above computations included the Sudakov resummation, however. In [14] a calculation has been performed that included both the full ITMD and the Sudakov resummation “model” [27], based on the reweighting the events with the DGLAP Sudakov form factor. The Authors compared the shape of the obtained azimuthal dijet correlations for proton–proton and proton–lead with those obtained by ATLAS collaboration [29] (no dijet cross section was actually measured, only the conditional yields). Interestingly, when the shapes of the azimuthal correlations for p–p and p–Pb are stacked together so that they match in the first bin, one can clearly see broadening of the p–Pb cross section. It turns out, that similar broadening is obtained within the ITMD, if both the saturation as well as the Sudakov resummation are present. We show this result in Fig. 10.

In the following, we shall report on further advances in dijet computations within ITMD, with the full Sudakov resummation [212]. In particular, we will present the numerical results for the differential cross sections in terms of the azimuthal angle $\Delta\phi$ between the leading and the sub-leading jets for the proton–proton and the proton–lead collisions at LHC energies. We shall also discuss the nuclear modification ratio R_{p-Pb}

$$R_{p-Pb} = \frac{d\sigma^{p+Pb}}{d\mathcal{O}} \bigg/ A \frac{d\sigma^{p+p}}{d\mathcal{O}}, \tag{84}$$

where \mathcal{O} is a differential related to an observable. Finally, we shall investigate differential cross sections in the rapidity of the leading and sub-leading jet.

The cross sections were computed using the KATIE Monte Carlo program [186] within the ITMD factorization, both described in the preceding Sections. We considered the

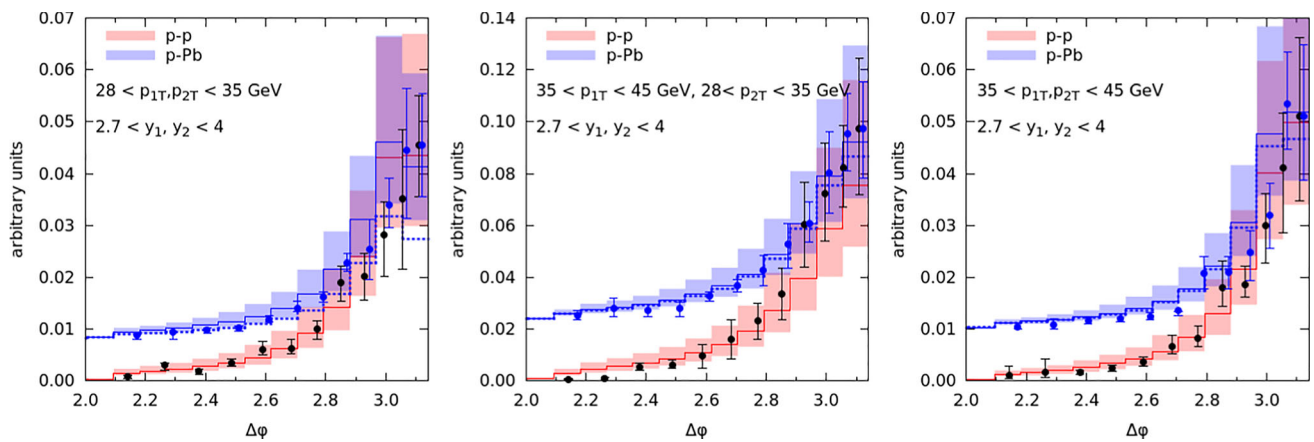


Fig. 10 Broadening of azimuthal correlations in p–Pb collisions vs p–p collisions for different sets of cuts imposed on the jets’ transverse momenta. The blue and red bands show the normalized differential cross sections in azimuthal angle $\Delta\phi$, respectively for p–Pb and p–p, shifted so that they match in the first bin. The points show the

experimental data [29] for p–p and p–Pb, where the p–Pb data were shifted by a pedestal, so that the values in the bin $\Delta\phi \sim \pi$ are the same. Theoretical calculations are represented by the histograms with uncertainty bands coming from varying the scale by factors 1/2 and 2

proton–proton and proton–lead collisions at $\sqrt{s} = 5.02$ TeV, 8.16 TeV and 8.8 TeV per nucleon. For proton–proton collisions, we also computed the proton–proton cross section for $\sqrt{s} = 14$ TeV. In order to define the leading and the sub-leading jets, mentioned above, we used the anti- k_T jet clustering algorithm [213] with a radius of $R = 0.4$. Since our computation is leading order, the jet algorithm is actually equivalent to a simple cut in rapidity-azimuthal plane. Motivated by the current and planned LHC experiments, we applied the following cuts to the transverse momentum of these jets:

- i) $28 \text{ GeV} < p_{T1}, p_{T2} < 35 \text{ GeV}$,
- ii) $35 \text{ GeV} < p_{T1}, p_{T2} < 45 \text{ GeV}$,
- iii) $35 \text{ GeV} < p_{T1} < 45 \text{ GeV}$ and $28 \text{ GeV} < p_{T2} < 35 \text{ GeV}$,
- iv) $p_{T1}, p_{T2} > 10 \text{ GeV}$,
- v) $p_{T1}, p_{T2} > 20 \text{ GeV}$.

Specifically, we used the first three cuts *i) – iii)* for the transverse momentum of the jets in the rapidity range $2.7 < y_1^*, y_2^* < 4.0$, both for proton–proton and proton–lead collisions at $\sqrt{s} = 8.16$ TeV. These cuts correspond to the FCal calorimeter of the ATLAS detector and are motivated by the measurement [29]. The last two cuts *iv) – v)* were applied in the rapidity range $3.8 < y_1^*, y_2^* < 5.1$, both for proton–proton and proton–lead collisions at $\sqrt{s} = 5.02$ TeV, and 8.8 TeV energies per nucleon. These correspond to the planned FoCal extension of the ALICE detector [31]. For the same kinematic domain (rapidity and transverse momentum cuts for the jets), we also considered protons collisions at $\sqrt{s} = 14$ TeV (proton–lead collisions are not feasible at

this energy). The result for 5.02 TeV and 14 TeV were not published in [212] and are thus new.

The factorization and renormalization scales were set using the transverse momentum of the leading and the sub-leading jets $\mu = (p_{T1} + p_{T2})/2$. For the TMD gluon distributions, we used the ones calculated in [209] based on the Kutak-Sapeta (KS) fit of the dipole gluon density [12], as described in the preceding subsections. For the collinear PDFs we used the CTEQ10NLO PDF set [214] from LHAPDF6 [215]. For the computation of the cross sections, we included the channels $qg^* \rightarrow qg$, with five quark flavours, and $gg^* \rightarrow gg$. The channel $gg^* \rightarrow \bar{q}q$ was neglected because its contribution, for the considered kinematic domain, is quite small [12,209].

Let us now discuss the results. In Fig. 11 we show the results for the azimuthal correlations for p–p and p–Pb collisions in the ATLAS kinematics at $\sqrt{s} = 8.16$ TeV. We compare the Sudakov resummation obtained via two methods, the full- b space resummation (dotted) and the simplified approach, where the collinear PDF is not affected by the Sudakov form factor. As can be seen, they differ a bit, but as we shall see below, the difference cancels in the nuclear modification ratio, and thus does not affect the saturation signal. Moreover, as we also show below, there are very large scale uncertainties, within which both methods are qualitatively similar. In our computations, we used the ITMD factorization alone, without parton shower or hadronisation corrections. In order to assess this effect, we computed cross section with PYTHIA [216,217] with all correction turned on, and then just with initial-state parton shower. The latter roughly corresponds to the TMD framework (as discussed e.g. in [218]), therefore both calculations allow for the extraction of a “cor-

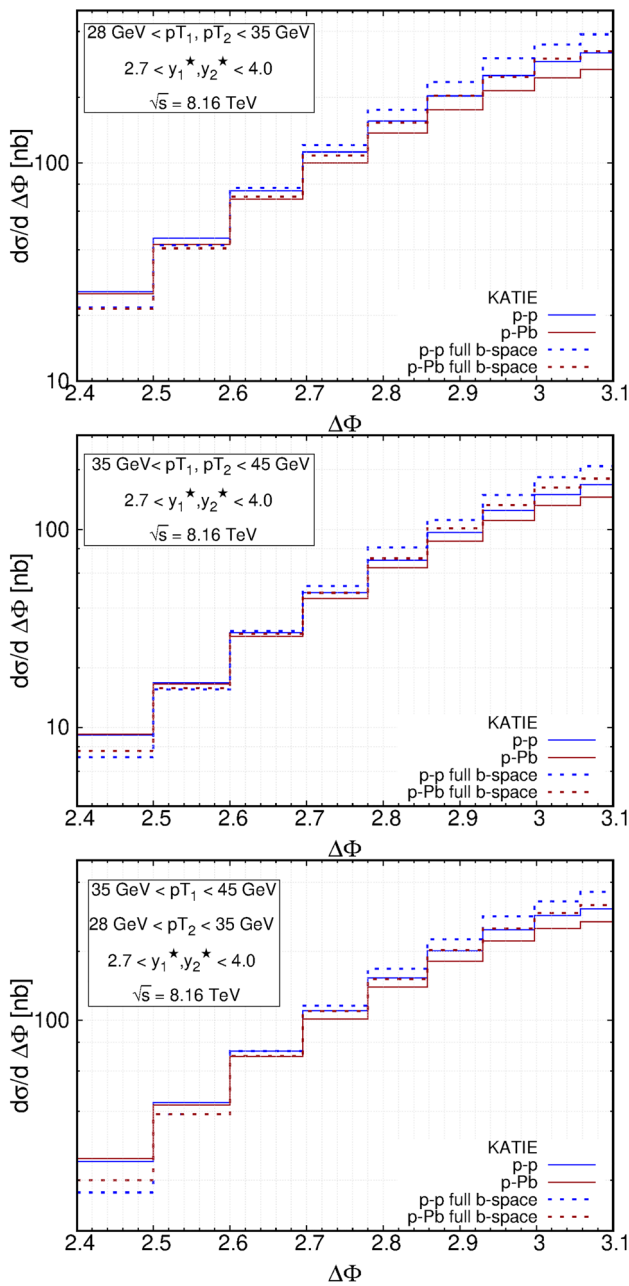


Fig. 11 The differential cross sections in terms of the azimuthal angle $\Delta\phi$ between the leading and the sub-leading jets for the proton–proton and the proton–lead collisions at $\sqrt{s} = 8.16$ TeV in the FCal ATLAS kinematics. These were computed using KATIE within the ITMD factorization formula with: the simplified Sudakov resummation Eq. (42) (solid lines), the full b -space resummation Eq. (65) (dotted lines). The plots were taken from [212]

rection factor”. We repeated the same procedure using the nuclear PDFs in PYTHIA. In Fig. 12 we applied that correction to KATIE results and compared with PYTHIA computations. Although the correction factor is rather large, as we shall see below it does not affect the saturation signal in the nuclear modification ratio. Next, in Fig. 13 we show the error bands

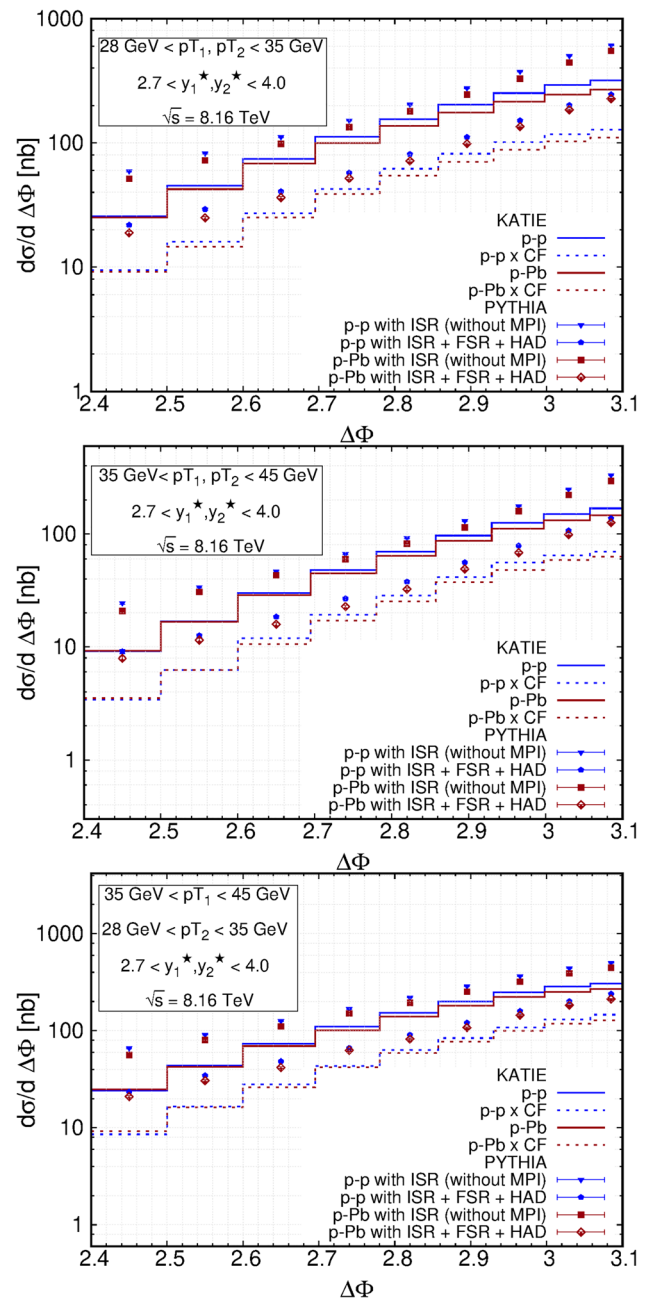


Fig. 12 The differential cross sections in terms of the azimuthal angle $\Delta\phi$ between the leading and the sub-leading jets for the proton–proton and the proton–lead collisions at $\sqrt{s} = 8.16$ TeV in the FCal ATLAS kinematics. The solid lines represent the results from KATIE computed within the ITMD approach, the points represent the results from PYTHIA with different components, and the dotted lines represent the KATIE results corrected with the non-perturbative correction factor extracted from PYTHIA. The plots were taken from [212]

due to both scale variation. Finally, in Fig. 14 we compute the nuclear modification ratio. For all three p_T cuts, we show the ITMD result with simplified Sudakov resummation, with the full- b space resummation, and the result where the non-perturbative correction factor from PYTHIA was applied.

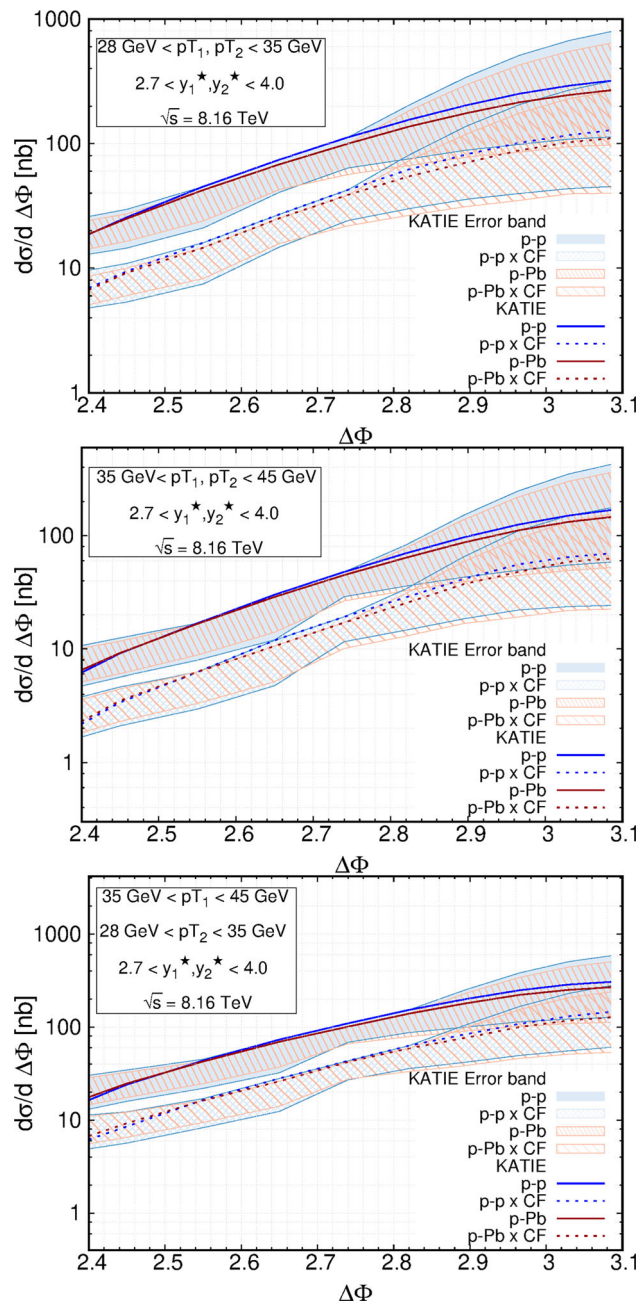


Fig. 13 The differential cross sections in terms of the azimuthal angle $\Delta\phi$ between the leading and the sub-leading jets for the proton–proton and the proton–lead collisions at $\sqrt{s} = 8.16$ TeV in the FCal ATLAS kinematics. The solid lines represent the results from KATIE computed within the ITMD approach, and the dotted lines represent the KATIE results corrected with the non-perturbative correction factor extracted from PYTHIA. The bands represent the error due to the variation of the factorization/renormalization scales from a value of $(p_{T1} + p_{T2})/2$ by a factor of 1/2 and 2. The plots were taken from [212]

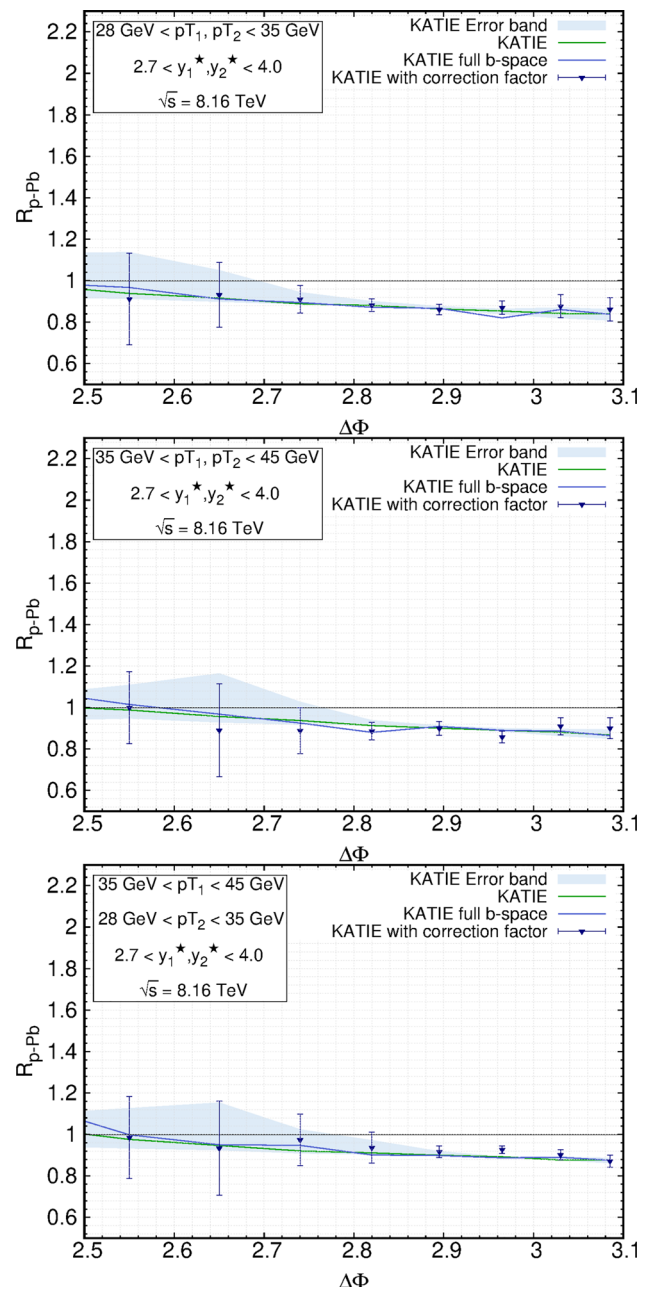


Fig. 14 Nuclear modification ratios R_{p-Pb} in terms of the azimuthal angle $\Delta\phi$ between the leading and the sub-leading jets for the proton–proton and the proton–lead collisions at $\sqrt{s} = 8.16$ TeV in the FCal ATLAS kinematics. The solid lines represent the results from KATIE computed within the ITMD approach with: the simplified Sudakov resummation Eq. (42) (red line), the full b -space resummation Eq. (65) (blue line). The band represents the error due to the variation of the factorization/renormalization scales from a value of $(p_{T1} + p_{T2})/2$ by a factor of 1/2 and 2. The points ∇ represent the KATIE results corrected with the non-perturbative correction factor extracted from PYTHIA. The error bars associated with these points account for both errors due to variation of scale in KATIE and the statistical uncertainties in the correction factor from PYTHIA. The plots were taken from [212]

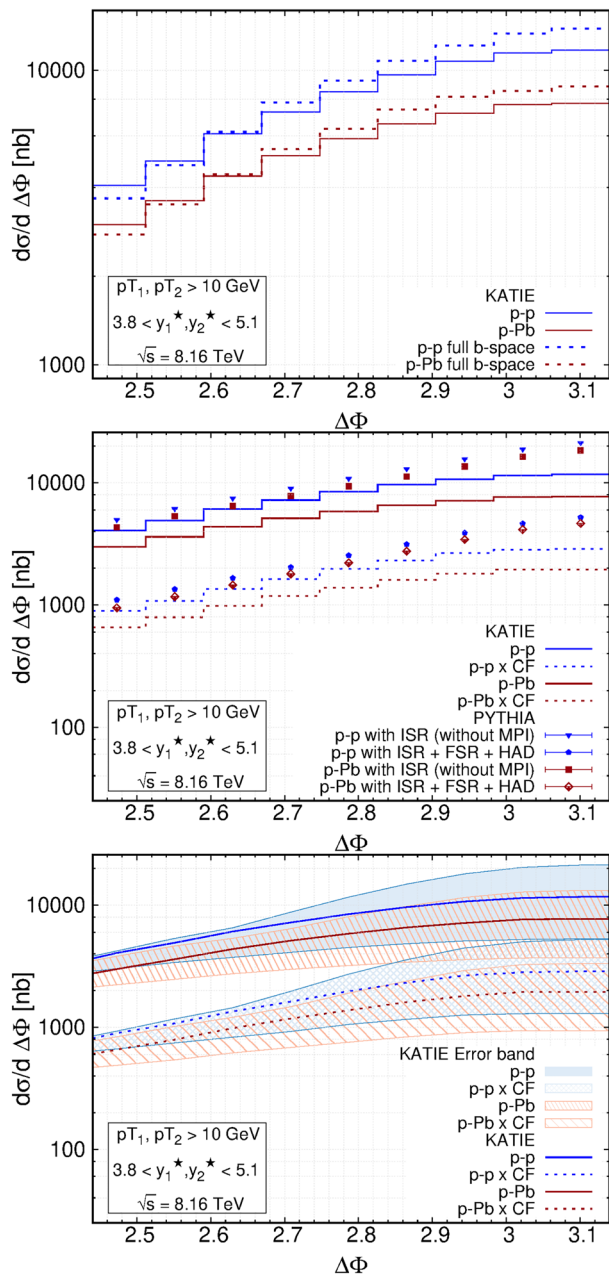


Fig. 15 The differential cross sections in terms of the azimuthal angle $\Delta\phi$ between the leading and the sub-leading jets for the proton–proton and the proton–lead collisions at $\sqrt{s} = 8.16$ TeV in the ALICE FoCal kinematics. The first plot represents the cross sections computed using KATIE within the ITMD factorization formula with: the simplified Sudakov resummation Eq. (42) (solid lines), the full b -space resummation Eq. (65) (dotted lines). In the second plot, the solid lines represent the cross sections from KATIE computed within the ITMD approach, the points represent the results from PYTHIA with different components, and the dotted lines represent the KATIE results corrected with the non-perturbative correction factor extracted from PYTHIA. In the third plot, the solid lines represent the cross sections from KATIE computed within the ITMD approach, and the dotted lines represent the KATIE results corrected with the non-perturbative correction factor extracted from PYTHIA. The bands represent the error due to the variation of the factorization/renormalization scales in KATIE from a value of $(p_{T1} + p_{T2})/2$ by a factor of 1/2 and 2. The plots were taken from [212]

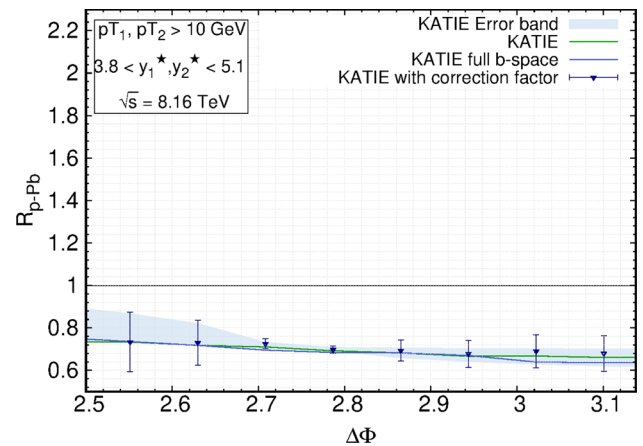


Fig. 16 Nuclear modification ratio R_{p-Pb} in terms of the azimuthal angle $\Delta\phi$ between the leading and the sub-leading jets for the proton–proton and the proton–lead collisions at $\sqrt{s} = 8.16$ TeV in the ALICE FoCal kinematics. The solid lines represent the results from KATIE computed within the ITMD approach with: the simplified Sudakov resummation Eq. (42) (red line), the full b -space resummation Eq. (65) (blue line). The band represents the error due to the variation of the factorization/renormalization scales from a value of $(p_{T1} + p_{T2})/2$ by a factor of 1/2 and 2. The points ∇ represent the KATIE results corrected with the non-perturbative correction factor extracted from PYTHIA. The error bars associated with these points account for both errors due to variation of scale in KATIE and the statistical uncertainties in the correction factor from PYTHIA. The plots were taken from [212]

We also compute the error band due to scale variation and due to the correction factor. We see, that the saturation effect due to the nonlinear evolution is visible, but not very significant for the considered kinematics. For the lower p_T cut, we observe suppression of about 15%, but the uncertainty due to the correction factor is not much less. Interestingly (but understandably) this error decreases for larger p_T bins.

Next, we move on to the more forward region with FoCal kinematics. Here we focus first on the $p_T > 10$ GeV cut. The results for azimuthal correlations are shown in Fig. 15. In one figure we show ITMD results with Sudakov obtained via both models, as well as PYTHIA corrections and error-bands, as discussed before. In Fig. 16 we compute the nuclear modification ratio for that case. As can be seen from the plot, the suppression due to saturation is very large, about 25–30%, and is not destroyed by the errors, both due to the scale variation and due to the non-perturbative effects. In Fig. 17 we show the latest results, where we compare p–p and p–Pb cross sections at different energies, computed also with larger $p_T > 20$ GeV cut. As expected, the difference between p–p and p–Pb is smaller in that case. Next, in Figs. 18 and 19 we present the latest results for rapidity distributions for the two p_T cuts, for the leading jet, and the sub-leading jet. As the shape of the rapidity distribution is correlated with the x dependence, and thus with the evolution in the energy, measurement of the rapidity distribution may provide a valuable discriminatory tool for the evolution equations. Finally, in

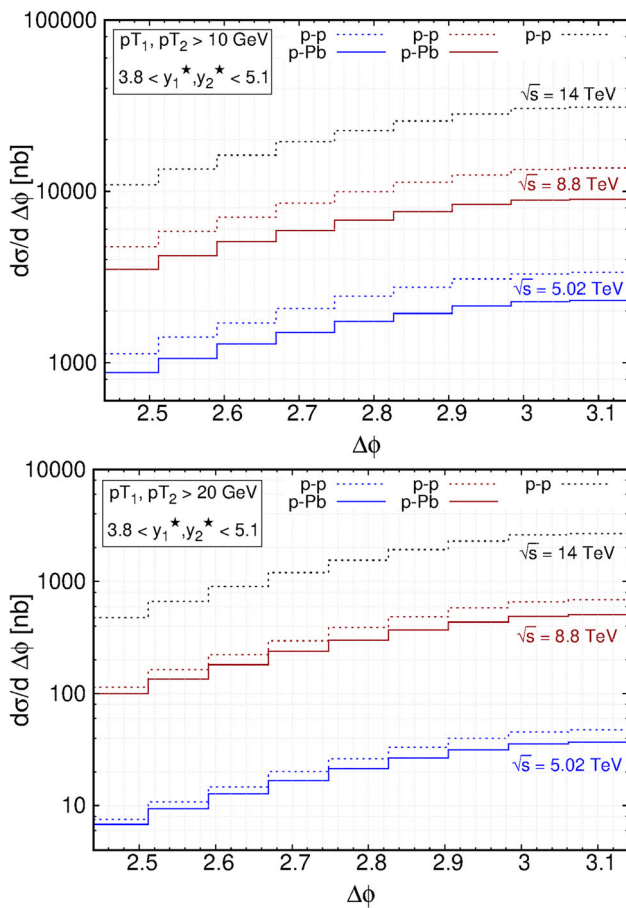


Fig. 17 The differential cross sections in terms of the azimuthal angle $\Delta\phi$ between the leading and the sub-leading jets for the proton–proton and the proton–lead collisions at $\sqrt{s} = 5.02$ TeV (blue) and 8.8 TeV (red) in the ALICE FoCal kinematics. For the same kinematics, each plot also represents the differential cross section for the proton–proton collision at $\sqrt{s} = 5.02$ TeV (black). Since proton–lead collisions are not feasible at this energy, we didn’t compute those. All of these cross sections were computed using KATIE within the ITMD factorization formula with the simplified Sudakov resummation Eq. (42) The solid lines represent the results for proton–lead collisions and the dotted lines represent the results for the proton–proton collisions

Fig. 20 we show the nuclear modification ratio for the two energies and both p_T cuts. As can be seen, with forward FoCal kinematics, even with the p_T cut of 20 GeV the suppression is about 20%.

7.2 Forward dijets at electron ion collider

While the focus of this review is on forward jets at LHC, the new accelerator Electron Ion Collider (EIC) is just around the corner [33]. A vital part of its research program is to look for gluon saturation. However, since the involved hard scales are lower than at the LHC, in fact, hadrons constitute better probes of the saturation physics than jets. Nevertheless, there has been a large interest in jets at EIC, see for example [184,

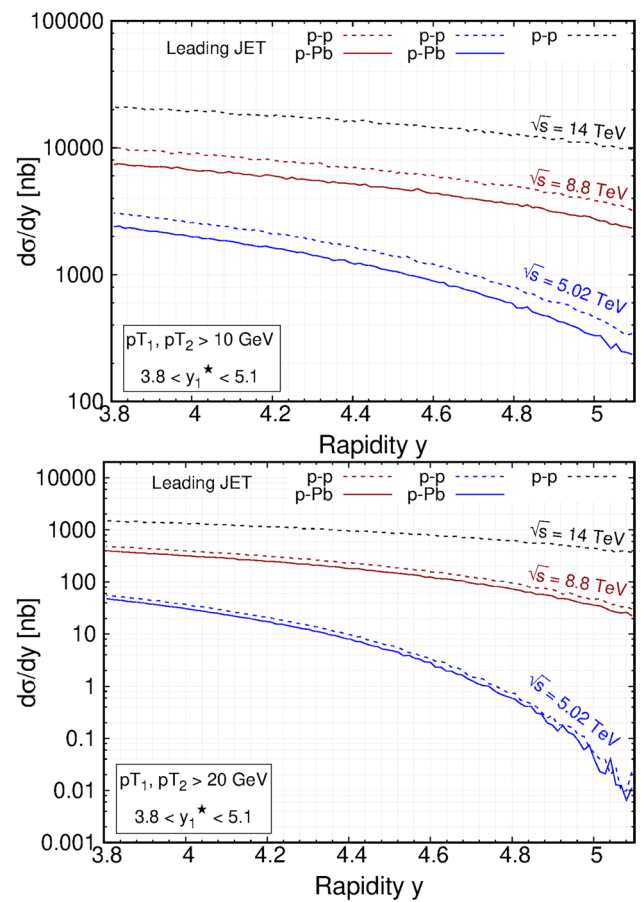


Fig. 18 The differential cross sections in terms of the rapidity of the leading jet y_1^* for the proton–proton and the proton–lead collisions at $\sqrt{s} = 5.02$ TeV (blue) and 8.8 TeV (red) in the ALICE FoCal kinematics. For the same kinematics, each plot also represents the differential cross section for the proton–proton collision at $\sqrt{s} = 5.02$ TeV (black). Since proton–lead collisions are not feasible at this energy, we didn’t compute those. All of these cross sections were computed using KATIE within the ITMD factorization formula with the simplified Sudakov resummation Eq. (42) The solid lines represent the results for proton–lead collisions and the dotted lines represent the results for the proton–proton collisions

219, 220]. Moreover, at the partonic level, both hadron and jet production need classes of the same diagrams. Therefore, the upcoming EIC experiment triggered tremendous progress in computing NLO corrections for the DIS process within the CGC formalism, see for example [101, 106, 139, 144, 221, 222].

In the context of the ITMD factorization, dijet production at EIC is actually a very interesting and important process. As discussed eg. in [168] the only TMD gluon distribution that is relevant for dijets in DIS, in the back-to-back limit, is the Weizsacker–Williams (WW) gluon distribution $F_{gg}^{(3)}$ (called

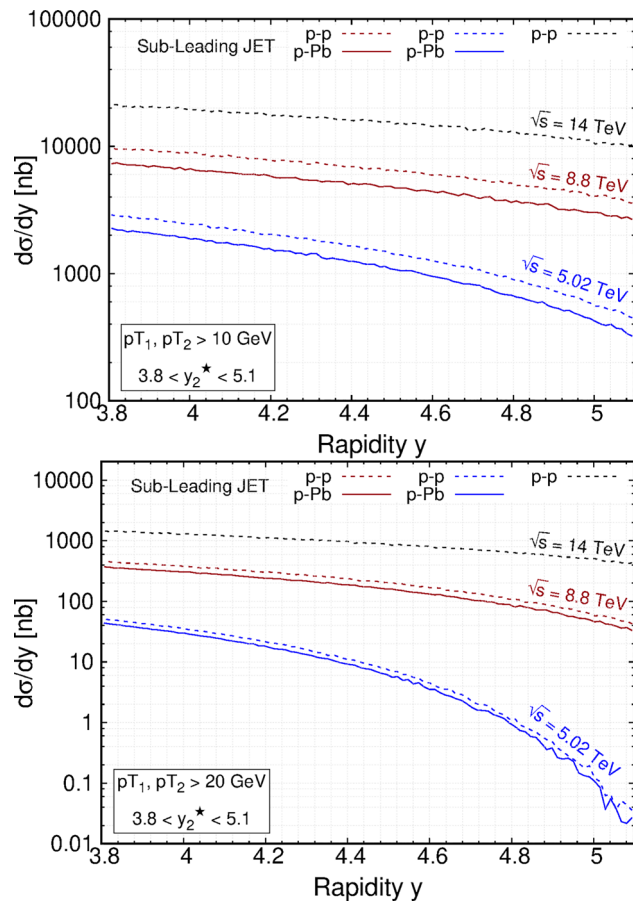


Fig. 19 The differential cross sections in terms of the rapidity of the sub-leading jet y_2^* for the proton–proton and the proton–lead collisions at $\sqrt{s} = 5.02$ TeV (blue) and 8.8 TeV (red) in the ALICE FoCal kinematics. For the same kinematics, each plot also represents the differential cross section for the proton–proton collision at $\sqrt{s} = 5.02$ TeV (black). Since proton–lead collisions are not feasible at this energy, we didn’t compute those. All of these cross sections were computed using KATIE within the ITMD factorization formula with the simplified Sudakov resummation Eq. (42) The solid lines represent the results for proton–lead collisions and the dotted lines represent the results for the proton–proton collisions

also $xG^{(1)}$.² For the ITMD factorization, this is only true for sufficiently small photon virtuality $Q^2 \ll p_T$, otherwise longitudinally polarized gluons contribute, and they are not formally accounted for in the ITMD approach. Due to this fact, for processes where such contributions formally enter, the ITMD factorization is called ITMD* (see for example [185] for the trijet production case).

The dijet production in the DIS process gives actually more interesting observables than dijets in hadron–hadron scattering. This is because there is also an identified electron in the final state. Thus, in addition to dijet azimuthal cor-

² This distribution is also probed in forward Ultra Peripheral Collisions at LHC. We however do not discuss this process here. The first application of ITMD to UPC processes can be found in [223].

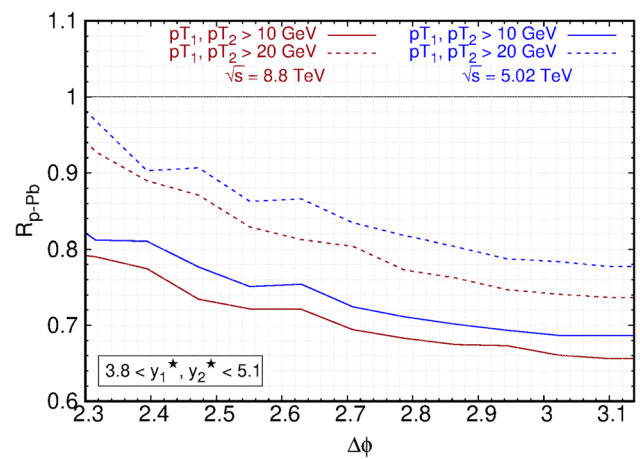


Fig. 20 Nuclear modification ratio R_{p-Pb} in terms of the azimuthal angle $\Delta\phi$ between the leading and the sub-leading jets for the proton–proton and the proton–lead collisions at $\sqrt{s} = 5.02$ TeV (blue) and 8.8 TeV (red) in the ALICE FoCal kinematics. The solid lines represent the results from KATIE computed within the ITMD approach with the simplified Sudakov resummation Eq. (42) for $p_{T1}, p_{T2} > 10$ GeV. And the dotted lines represent the results for $p_{T1}, p_{T2} > 20$ GeV

relations, one can also study correlations with the outgoing electron.

The ITMD* factorization formula for the process

$$A(P_A) + e^-(P_B) \rightarrow J(p_1) + J(p_2) + e^-(P'_B) + X, \quad (85)$$

reads

$$d\sigma_{eA \rightarrow e'+2j+X} = \int \frac{dx_A}{x_A} d^2k_T \times \frac{1}{4\pi x_A P_A \cdot P_B} \mathcal{F}_{gg}^{(3)}(x_A, |\vec{k}_T|, \mu) |\overline{M}_{eg^* \rightarrow e'+2j}|^2 d\Gamma_3. \quad (86)$$

As mentioned above, there is only WW gluon distribution in the above formula.

In [224] we computed several observables using the above framework, not only to quantify possible saturation effects in dijet observable at EIC but also to demonstrate the relevance of interplay of the saturation, the Sudakov effect, and the exact kinematics.

First, we found that in the context of saturation physics, it is best to consider forward dijets. This provides a very good focusing of the x_A distribution around the sufficiently small values so that the use of the small- x formalism is well justified. For the WW gluon distribution, we used the Kutak–Sapeta fit of the dipole TMD to HERA data, and then the WW TMD distribution was calculated in the mean field approximation (see Sect. 6.5). The calculation was supplemented with the Sudakov form factor, see Fig. 9 and the corresponding discussion in the text. In Fig. 21 we show prediction for the cross section dependence on azimuthal angle between the dijet system and the scattered electron for CM energy per

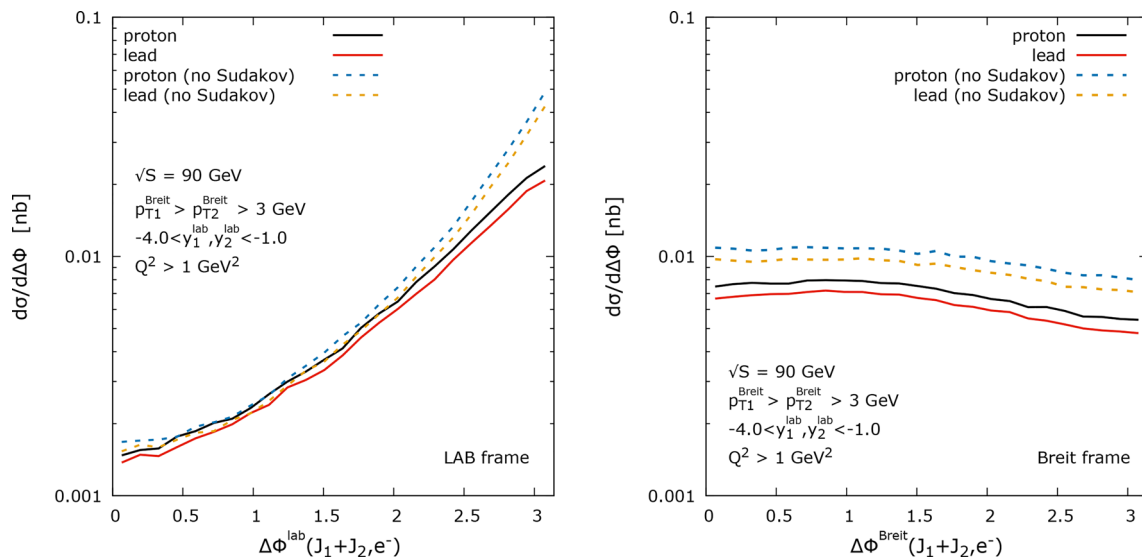


Fig. 21 Azimuthal correlations between the total transverse momentum of the dijet system and the transverse momentum of the scattered electron at EIC in two frames: the LAB frame (left), and the Breit

frame (right). The calculation has been done within the ITMD* framework with the Weizsäcker–Williams gluon distribution obtained from the Kutak–Sapeta fit to HERA data

nucleon $\sqrt{s} = 90$ GeV. The calculations are done both in the lab frame and the Breit frame. One clearly sees effects coming from the Sudakov form factor while the saturation is rather mild, despite the cut on the jet transverse momentum (in the Breit frame) is very low. Primarily, it is a consequence of the saturation pattern visible in the WW gluon distribution. Unlike the dipole gluon distribution, it does not have a peak as a function of the transverse momentum, c.f. Figs. 9 and 8. In our computation, we put quite a low cut on the photon virtuality $Q^2 > 1$ GeV² in order to suppress the longitudinal gluons. For a complete discussion see [224,225].

8 Summary and outlook

The text discusses the challenges and selected ongoing research related to searches of gluon saturation in QCD using dijet observables. Although there are indications of saturation in the experimental data, achieving a complete consensus on its existence is still a challenge due to demanding kinematics and the complex collision environment. While there are simpler observables than dijets, the latter have the advantage of providing the azimuthal correlations, which in the back-to-back kinematics are sensitive to saturation even for relatively hard jets.

The study of forward dijet production, using the Improved TMD Factorization (ITMD) framework, is a relatively novel proposal in the search for gluon saturation. The framework has been already used in addressing many dijet related observables that were reviewed in this work. The text high-

lights the need for more measurements and the construction of the FoCal detector by the ALICE collaboration to shed more light on the saturation phenomenon. Furthermore, it discusses complementary dijet measurements in photon nucleus scattering that can be done at the Electron Ion Collider.

While in the review we focused our attention on dijets, there are other forward physics final states that can be used to search for saturation effects [226]. Those include di-hadrons [13,227,228], J/ψ production [229], and trijets [148,185]. The processes are complementary to dijets, however, in some aspects more challenging. The di-hadrons require knowledge of fragmentation function and are sensitive to longitudinal polarization effects while trijets are just more difficult to measure and interpret.

Future research will be focused on increasing the precision of the calculations. The ITMD framework is well suited to extrapolate methods known in collinear factorization to compute higher order corrections to off-shell gauge invariant matrix elements, and in principle to automatize NLO computations. First steps toward that goal have already been undertaken [230–233]. Also, it is important to increase the accuracy of the evolution equations, parton densities and there is also a substantial progress in this direction, see for example [112,178,234–242]. Last but not least, the ITMD framework should account for the longitudinally polarized gluons, which contribute to some processes (see eg. [243]). The corresponding amplitudes should be obtainable automatically, similarly to off-shell gauge invariant amplitudes coupled eikonally that are used currently in the ITMD. Research in that direction is also ongoing.

Acknowledgements We would like to thank Jacek Otwinowski for interesting and stimulating discussions and Francesco Hautmann for useful comments. HK is supported by the National Science Centre, Poland Grant no. DEC-2021/41/N/ST2/02956. PK is partially supported by the National Science Centre, Poland Grant no. DEC-2020/39/O/ST2/03011. KK acknowledges the Polish National Science Centre Grant no. DEC-2017/27/B/ST2/01985. AvH is supported by the National Science Centre, Poland Grant no. DEC-2019/35/B/ST2/03531.

Data availability This manuscript has no associated data or the data will not be deposited. [Authors' comment: This is a theoretical paper and has no data.]

Open Access This article is licensed under a Creative Commons Attribution 4.0 International License, which permits use, sharing, adaptation, distribution and reproduction in any medium or format, as long as you give appropriate credit to the original author(s) and the source, provide a link to the Creative Commons licence, and indicate if changes were made. The images or other third party material in this article are included in the article's Creative Commons licence, unless indicated otherwise in a credit line to the material. If material is not included in the article's Creative Commons licence and your intended use is not permitted by statutory regulation or exceeds the permitted use, you will need to obtain permission directly from the copyright holder. To view a copy of this licence, visit <http://creativecommons.org/licenses/by/4.0/>.

Funded by SCOAP³. SCOAP³ supports the goals of the International Year of Basic Sciences for Sustainable Development.

References

- L. Gribov, E. Levin, M. Ryskin, Semihard Processes in QCD. *Phys. Rep.* **100**, 1–150 (1983). [https://doi.org/10.1016/0370-1573\(83\)90022-4](https://doi.org/10.1016/0370-1573(83)90022-4)
- A.H. Mueller, J.-W. Qiu, Gluon recombination and shadowing at small values of x . *Nucl. Phys. B* **268**, 427–452 (1986). [https://doi.org/10.1016/0550-3213\(86\)90164-1](https://doi.org/10.1016/0550-3213(86)90164-1)
- E. Iancu, R. Venugopalan, The Color glass condensate and high-energy scattering in QCD. *3*, 249–3363 (2003). https://doi.org/10.1142/9789812795533_0005. arXiv:hep-ph/0303204
- J. Jalilian-Marian, Y.V. Kovchegov, Saturation physics and deuteron-Gold collisions at RHIC. *Prog. Part. Nucl. Phys.* **56**, 104–231 (2006). <https://doi.org/10.1016/j.pnnp.2005.07.002>. arXiv:hep-ph/0505052
- F. Gelis, E. Iancu, J. Jalilian-Marian, R. Venugopalan, The color glass condensate. *Ann. Rev. Nucl. Part. Sci.* **60**, 463–489 (2010). <https://doi.org/10.1146/annurev.nucl.010909.083629>. arXiv:1002.0333
- J.L. Albacete, C. Marquet, Gluon saturation and initial conditions for relativistic heavy ion collisions. *Prog. Part. Nucl. Phys.* **76**, 1–42 (2014). <https://doi.org/10.1016/j.pnnp.2014.01.004>. arXiv:1401.4866
- J.-P. Blaizot, High gluon densities in heavy ion collisions. *Rep. Prog. Phys.* **80**, 032301 (2017). <https://doi.org/10.1088/1361-6633/aa5435>. arXiv:1607.04448
- Y.V. Kovchegov, E. Levin, *Quantum Chromodynamics at High Energy*, vol. 33 (Cambridge University Press, Cambridge, 2012). <https://doi.org/10.1017/CBO9781139022187>
- K.J. Golec-Biernat, M. Wusthoff, Saturation effects in deep inelastic scattering at low Q^2 and its implications on diffraction. *Phys. Rev. D* **59**, 014017 (1998). <https://doi.org/10.1103/PhysRevD.59.014017>. arXiv:hep-ph/9807513
- J.L. Albacete, C. Marquet, Azimuthal correlations of forward dihadrons in d+Au collisions at RHIC in the Color Glass Condensate. *Phys. Rev. Lett.* **105**, 162301 (2010). <https://doi.org/10.1103/PhysRevLett.105.162301>. arXiv:1005.4065
- K. Dusling, R. Venugopalan, Evidence for BFKL and saturation dynamics from dihadron spectra at the LHC. *Phys. Rev. D* **87**, 051502 (2013). <https://doi.org/10.1103/PhysRevD.87.051502>. arXiv:1210.3890
- K. Kutak, S. Sapeta, Gluon saturation in dijet production in p-Pb collisions at Large Hadron Collider. *Phys. Rev. D* **86**, 094043 (2012). <https://doi.org/10.1103/PhysRevD.86.094043>. arXiv:1205.5035
- A. Stasto, S.-Y. Wei, B.-W. Xiao, F. Yuan, On the Dihadron angular correlations in forward pA collisions. *Phys. Lett. B* **784**, 301–306 (2018). <https://doi.org/10.1016/j.physletb.2018.08.011>. arXiv:1805.05712
- A. van Hameren, P. Kotko, K. Kutak, S. Sapeta, Broadening and saturation effects in dijet azimuthal correlations in p-p and p-Pb collisions at $\sqrt{s} = 5.02$ TeV. *Phys. Lett. B* **795**, 511–515 (2019). <https://doi.org/10.1016/j.physletb.2019.06.055>. arXiv:1903.01361
- H. Mäntysaari, H. Paukkunen, Saturation and forward jets in proton-lead collisions at the LHC. *Phys. Rev. D* **100**, 114029 (2019). <https://doi.org/10.1103/PhysRevD.100.114029>. arXiv:1910.13116
- B. Ducloué, E. Iancu, G. Soyez, D.N. Triantafyllopoulos, HERA data and collinearly-improved BK dynamics. *Phys. Lett. B* **803**, 135305 (2020). <https://doi.org/10.1016/j.physletb.2020.135305>. arXiv:1912.09196
- A. Arroyo Garcia, M. Hentschinski, K. Kutak, QCD evolution based evidence for the onset of gluon saturation in exclusive photo-production of vector mesons. *Phys. Lett. B* **795**, 569–575 (2019). <https://doi.org/10.1016/j.physletb.2019.06.061>. arXiv:1904.04394
- STAR collaboration, M.S. Abdallah et al., Evidence for nonlinear gluon effects in QCD and their mass number dependence at STAR. *Phys. Rev. Lett.* **129**, 092501 (2022). <https://doi.org/10.1103/PhysRevLett.129.092501>. arXiv:2111.10396
- G. Beuf, H. Hänninen, T. Lappi, H. Mäntysaari, Color glass condensate at next-to-leading order meets HERA data. *Phys. Rev. D* **102**, 074028 (2020). <https://doi.org/10.1103/PhysRevD.102.074028>. arXiv:2007.01645
- A. Morreale, F. Salazar, Mining for gluon saturation at colliders. *Universe* **7**, 312 (2021). <https://doi.org/10.3390/universe7080312>. arXiv:2108.08254
- M. Cacciari, J. Rojo, G.P. Salam, G. Soyez, Jet reconstruction in heavy ion collisions. *Eur. Phys. J. C* **71**, 1539 (2011). <https://doi.org/10.1140/epjc/s10052-011-1539-z>. arXiv:1010.1759
- C. Marquet, Forward inclusive dijet production and azimuthal correlations in p(A) collisions. *Nucl. Phys. A* **796**, 41–60 (2007). <https://doi.org/10.1016/j.nuclphysa.2007.09.001>. arXiv:0708.0231
- A. van Hameren, P. Kotko, K. Kutak, C. Marquet, S. Sapeta, Saturation effects in forward-forward dijet production in p+Pb collisions. *Phys. Rev. D* **89**, 094014 (2014). <https://doi.org/10.1103/PhysRevD.89.094014>. arXiv:1402.5065
- K. Kutak, Hard scale dependent gluon density, saturation and forward-forward dijet production at the LHC. *Phys. Rev. D* **91**, 034021 (2015). <https://doi.org/10.1103/PhysRevD.91.034021>. arXiv:1409.3822
- M. Deak, F. Hautmann, H. Jung, K. Kutak, Forward-central jet correlations at the large hadron collider. arXiv:1012.6037
- M. Deak, F. Hautmann, H. Jung, K. Kutak, Forward jets and energy flow in hadronic collisions. *Eur. Phys. J. C* **72**, 1982 (2012). <https://doi.org/10.1140/epjc/s10052-012-1982-5>. arXiv:1112.6354

27. A. van Hameren, P. Kotko, K. Kutak, S. Sapeta, Small- x dynamics in forward-central dijet decorrelations at the LHC. *Phys. Lett. B* **737**, 335–340 (2014). <https://doi.org/10.1016/j.physletb.2014.09.005>. arXiv:1404.6204
28. A. van Hameren, P. Kotko, K. Kutak, S. Sapeta, Sudakov effects in central-forward dijet production in high energy factorization. *Phys. Lett. B* **814**, 136078 (2021). <https://doi.org/10.1016/j.physletb.2021.136078>. arXiv:2010.13066
29. ATLAS collaboration, M. Aaboud et al., Dijet azimuthal correlations and conditional yields in pp and p+Pb collisions at $\sqrt{s_{NN}}=5.02$ TeV with the ATLAS detector. *Phys. Rev. C* **100**, 034903 (2019). <https://doi.org/10.1103/PhysRevC.100.034903>. arXiv:1901.10440
30. CMS collaboration, A.M. Sirunyan et al., Measurement of inclusive very forward jet cross sections in proton–lead collisions at $\sqrt{s_{NN}} = 5.02$ TeV. *JHEP* **05**, 043 (2019). [https://doi.org/10.1007/JHEP05\(2019\)043](https://doi.org/10.1007/JHEP05(2019)043). arXiv:1812.01691
31. C. ALICE Collaboration, Letter of Intent: A Forward Calorimeter (FoCal) in the ALICE experiment, tech. rep., CERN, Geneva, Jun (2020)
32. A. Accardi et al., Electron ion collider: the next QCD frontier: understanding the glue that binds us all. *Eur. Phys. J. A* **52**, 268 (2016). <https://doi.org/10.1140/epja/i2016-16268-9>. arXiv:1212.1701
33. R. Abdul Khalek et al., Science requirements and detector concepts for the electron-ion collider: EIC yellow report. *Nucl. Phys. A* **1026**, 122447 (2022). <https://doi.org/10.1016/j.nuclphysa.2022.122447>. arXiv:2103.05419
34. P. Kotko, K. Kutak, C. Marquet, E. Petreska, S. Sapeta, A. van Hameren, Improved TMD factorization for forward dijet production in dilute-dense hadronic collisions. *JHEP* **09**, 106 (2015). [https://doi.org/10.1007/JHEP09\(2015\)106](https://doi.org/10.1007/JHEP09(2015)106). arXiv:1503.03421
35. J. Collins, *Foundations of Perturbative QCD*, vol. 32 (Cambridge University Press, Cambridge, 2013)
36. ATLAS collaboration, G. Aad et al., Measurement of Dijet Azimuthal Decorrelations in pp Collisions at $\sqrt{s} = 7$ TeV. *Phys. Rev. Lett.* **106**, 172002 (2011). <https://doi.org/10.1103/PhysRevLett.106.172002>. arXiv:1102.2696
37. CMS collaboration, V. Khachatryan et al., Dijet Azimuthal Decorrelations in pp Collisions at $\sqrt{s} = 7$ TeV. *Phys. Rev. Lett.* **106**, 122003 (2011). <https://doi.org/10.1103/PhysRevLett.106.122003>. arXiv:1101.5029
38. M. Bonvini, Small- x resummation in PDF fits and future prospects, in *Diffraction and Low- x 2022*, 12 (2022). arXiv:2212.14231
39. T.-J. Hou et al., New CTEQ global analysis of quantum chromodynamics with high-precision data from the LHC. arXiv:1912.10053
40. NNPDF collaboration, R.D. Ball et al., The path to proton structure at 1% accuracy. *Eur. Phys. J. C* **82**, 428 (2022). <https://doi.org/10.1140/epjc/s10052-022-10328-7>. arXiv:2109.02653
41. M. Froissart, Asymptotic behavior and subtractions in the Mandelstam representation. *Phys. Rev.* **123**, 1053–1057 (1961). <https://doi.org/10.1103/PhysRev.123.1053>
42. J. Bartels, K. Golec-Biernat, L. Motyka, Twist expansion of the nucleon structure functions, $F(2)$ and $F(L)$, in the DGLAP improved saturation model. *Phys. Rev. D* **81**, 054017 (2010). <https://doi.org/10.1103/PhysRevD.81.054017>. arXiv:0911.1935
43. L. Motyka, M. Sadzikowski, W. Slominski, Evidence of strong higher twist effects in diffractive DIS at HERA at moderate Q^2 . *Phys. Rev. D* **86**, 111501 (2012). <https://doi.org/10.1103/PhysRevD.86.111501>. arXiv:1203.5461
44. L. Motyka, M. Sadzikowski, Twist decomposition of proton structure from BFKL and BK amplitudes. *Acta Phys. Pol. B* **45**, 2079 (2014). <https://doi.org/10.5506/APhysPolB.45.2079>. arXiv:1411.7774
45. L. Motyka, M. Sadzikowski, T. Stebel, Twist expansion of Drell–Yan structure functions in color dipole approach. *JHEP* **05**, 087 (2015). [https://doi.org/10.1007/JHEP05\(2015\)087](https://doi.org/10.1007/JHEP05(2015)087). arXiv:1412.4675
46. D. Brzeminski, L. Motyka, M. Sadzikowski, T. Stebel, Twist decomposition of Drell–Yan structure functions: phenomenological implications. *JHEP* **01**, 005 (2017). [https://doi.org/10.1007/JHEP01\(2017\)005](https://doi.org/10.1007/JHEP01(2017)005). arXiv:1611.04449
47. L. Motyka, M. Sadzikowski, W. Słomiński, K. Wichmann, Evidence of quasi-partonic higher-twist effects in deep inelastic scattering at HERA at moderate Q^2 . *Eur. Phys. J. C* **78**, 80 (2018). <https://doi.org/10.1140/epjc/s10052-018-5548-z>. arXiv:1707.05992
48. U. Amaldi, R. Biancastelli, C. Bosio, G. Matthiae, J.V. Allaby, W. Bartel et al., The Energy dependence of the proton proton total cross-section for center-of-mass energies between 23 and 53 GeV. *Phys. Lett. B* **44**, 112–118 (1973). [https://doi.org/10.1016/0370-2693\(73\)90315-8](https://doi.org/10.1016/0370-2693(73)90315-8)
49. H.D.I. Abarbanel, J.B. Bronzan, R.L. Sugar, A.R. White, Reggeon field theory: formulation and use. *Phys. Rep.* **21**, 119–182 (1975). [https://doi.org/10.1016/0370-1573\(75\)90034-4](https://doi.org/10.1016/0370-1573(75)90034-4)
50. J. Bartels, C. Contreras, G.P. Vacca, Could reggeon field theory be an effective theory for QCD in the Regge limit? *JHEP* **03**, 201 (2016). [https://doi.org/10.1007/JHEP03\(2016\)201](https://doi.org/10.1007/JHEP03(2016)201). arXiv:1512.07182
51. A. Kovner, E. Levin, M. Li, M. Lublinsky, The JIMWLK evolution and the s -channel unitarity. *JHEP* **09**, 199 (2020). [https://doi.org/10.1007/JHEP09\(2020\)199](https://doi.org/10.1007/JHEP09(2020)199). arXiv:2006.15126
52. A. Kovner, E. Levin, M. Li, M. Lublinsky, Reggeon field theory and self duality: making ends meet. *JHEP* **10**, 185 (2020). [https://doi.org/10.1007/JHEP10\(2020\)185](https://doi.org/10.1007/JHEP10(2020)185). arXiv:2007.12132
53. I. Balitsky, L. Lipatov, The Pomeranchuk singularity in quantum chromodynamics. *Sov. J. Nucl. Phys.* **28**, 822–829 (1978)
54. E.A. Kuraev, L.N. Lipatov, V.S. Fadin, Multi-Reggeon processes in the Yang–Mills theory. *Sov. Phys. JETP* **44**, 443–450 (1976)
55. E.A. Kuraev, L.N. Lipatov, V.S. Fadin, The Pomeranchuk singularity in nonabelian gauge theories. *Sov. Phys. JETP* **45**, 199–204 (1977)
56. V.S. Fadin, E. Kuraev, L. Lipatov, On the Pomeranchuk singularity in asymptotically free theories. *Phys. Lett. B* **60**, 50–52 (1975). [https://doi.org/10.1016/0370-2693\(75\)90524-9](https://doi.org/10.1016/0370-2693(75)90524-9)
57. J.R. Forshaw, D.A. Ross, *Quantum Chromodynamics and the Pomeron*, vol. 9 (Oxford University Press, Oxford, 1998). <https://doi.org/10.1017/9781009290111>
58. J. Bartels, M. Wusthoff, The Triple Regge limit of diffractive dissociation in deep inelastic scattering. *Z. Phys. C* **66**, 157–180 (1995). <https://doi.org/10.1007/BF01496591>
59. J. Bartels, Unitarity corrections to the Lipatov pomeron and the four gluon operator in deep inelastic scattering in QCD. *Z. Phys. C* **60**, 471–488 (1993). <https://doi.org/10.1007/BF01560045>
60. J. Bartels, K. Kutak, A momentum space analysis of the triple Pomeron vertex in pQCD. *Eur. Phys. J. C* **53**, 533–548 (2008). <https://doi.org/10.1140/epjc/s10052-007-0501-6>. arXiv:0710.3060
61. R. Engel, Photoproduction within the two component dual parton model. 1. Amplitudes and cross-sections. *Z. Phys. C* **66**, 203–214 (1995). <https://doi.org/10.1007/BF01496594>
62. S. Roesler, R. Engel, J. Ranft, The Monte Carlo event generator DPMJET-III, in *International Conference on Advanced Monte Carlo for Radiation Physics, Particle Transport Simulation and Applications (MC 2000)*, 12 (2000), p. 1033–1038. https://doi.org/10.1007/978-3-642-18211-2_166. arXiv:hep-ph/0012252
63. K. Werner, F.-M. Liu, T. Pierog, Parton ladder splitting and the rapidity dependence of transverse momentum spectra in deuteron-gold collisions at RHIC. *Phys. Rev. C* **74**, 044902 (2006). <https://doi.org/10.1103/PhysRevC.74.044902>. arXiv:hep-ph/0506232

64. K. Werner, On a deep connection between factorization and saturation: new insight into modeling high-energy proton–proton and nucleus-nucleus scattering in the EPOS4 framework. [arXiv:2301.12517](https://arxiv.org/abs/2301.12517)
65. R.S. Fletcher, T.K. Gaisser, P. Lipari, T. Stanev, SIBYLL: an event generator for simulation of high-energy cosmic ray cascades. *Phys. Rev. D* **50**, 5710–5731 (1994). <https://doi.org/10.1103/PhysRevD.50.5710>
66. E.-J. Ahn, R. Engel, T.K. Gaisser, P. Lipari, T. Stanev, Cosmic ray interaction event generator SIBYLL 2.1. *Phys. Rev. D* **80**, 094003 (2009). <https://doi.org/10.1103/PhysRevD.80.094003>. [arXiv:0906.4113](https://arxiv.org/abs/0906.4113)
67. N.N. Kalmykov, S.S. Ostapchenko, A.I. Pavlov, Quark-gluon string model and EAS simulation problems at ultra-high energies. *Nucl. Phys. B Proc. Suppl.* **52**, 17–28 (1997). [https://doi.org/10.1016/S0920-5632\(96\)00846-8](https://doi.org/10.1016/S0920-5632(96)00846-8)
68. S. Ostapchenko, Monte Carlo treatment of hadronic interactions in enhanced Pomeron scheme: I. QGSJET-II model. *Phys. Rev. D* **83**, 014018 (2011). <https://doi.org/10.1103/PhysRevD.83.014018>. [arXiv:1010.1869](https://arxiv.org/abs/1010.1869)
69. L. Lipatov, Gauge invariant effective action for high-energy processes in QCD. *Nucl. Phys. B* **452**, 369–400 (1995). [https://doi.org/10.1016/0550-3213\(95\)00390-E](https://doi.org/10.1016/0550-3213(95)00390-E). [arXiv:hep-ph/9502308](https://arxiv.org/abs/hep-ph/9502308)
70. E. Antonov, L. Lipatov, E. Kuraev, I. Cherednikov, Feynman rules for effective Regge action. *Nucl. Phys. B* **721**, 111–135 (2005). <https://doi.org/10.1016/j.nuclphysb.2005.013>. [arXiv:hep-ph/0411185](https://arxiv.org/abs/hep-ph/0411185)
71. M. Hentschinski, Chapter 11: Lipatov’s QCD high energy effective action: past and future. 283–310 (2021). https://doi.org/10.1142/9789811231124_0011. [arXiv:2010.14748](https://arxiv.org/abs/2010.14748)
72. J. Bartels, V. Fadin, E. Levin, A. Levy, V. Kim, A. Sabio-Vera (eds.), *From the Past to the Future* (World Scientific, Singapore, 2021). <https://doi.org/10.1142/12127>
73. G. Chachamis, M. Hentschinski, J.D. Madrigal Martínez, A. Sabio Vera, Quark contribution to the gluon Regge trajectory at NLO from the high energy effective action. *Nucl. Phys. B* **861**, 133–144 (2012). <https://doi.org/10.1016/j.nuclphysb.2012.03.015>. [arXiv:1202.0649](https://arxiv.org/abs/1202.0649)
74. G. Chachamis, M. Hentschinski, J.D. Madrigal Martínez, A. Sabio Vera, Forward jet production & quantum corrections to the gluon Regge trajectory from Lipatov’s high energy effective action. *Phys. Part. Nucl.* **45**, 788–799 (2014). <https://doi.org/10.1134/S1063779614040030>. [arXiv:1211.2050](https://arxiv.org/abs/1211.2050)
75. G. Chachamis, M. Hentschinski, J.D. Madrigal Martínez, A. Sabio Vera, Next-to-leading order corrections to the gluon-induced forward jet vertex from the high energy effective action. *Phys. Rev. D* **87**, 076009 (2013). <https://doi.org/10.1103/PhysRevD.87.076009>. [arXiv:1212.4992](https://arxiv.org/abs/1212.4992)
76. G. Chachamis, M. Hentschinski, J.D. Madrigal Martínez, A. Sabio Vera, Gluon Regge trajectory at two loops from Lipatov’s high energy effective action. *Nucl. Phys. B* **876**, 453–472 (2013). <https://doi.org/10.1016/j.nuclphysb.2013.08.013>. [arXiv:1307.2591](https://arxiv.org/abs/1307.2591)
77. M. Hentschinski, J.D. Madrigal Martínez, B. Murdaca, A. Sabio Vera, The next-to-leading order vertex for a forward jet plus a rapidity gap at high energies. *Phys. Lett. B* **735**, 168–172 (2014). <https://doi.org/10.1016/j.physletb.2014.06.022>. [arXiv:1404.2937](https://arxiv.org/abs/1404.2937)
78. S. Bondarenko, L. Lipatov, A. Prygarin, Effective action for reggeized gluons, classical gluon field of relativistic color charge and color glass condensate approach. *Eur. Phys. J. C* **77**, 527 (2017). <https://doi.org/10.1140/epjc/s10052-017-5101-5>. [arXiv:1706.00278](https://arxiv.org/abs/1706.00278)
79. M. Hentschinski, Color glass condensate formalism, Balitsky–JIMWLK evolution, and Lipatov’s high energy effective action. *Phys. Rev. D* **97**, 114027 (2018). <https://doi.org/10.1103/PhysRevD.97.114027>. [arXiv:1802.06755](https://arxiv.org/abs/1802.06755)
80. S. Bondarenko, L. Lipatov, S. Pozdnyakov, A. Prygarin, One loop light-cone QCD, effective action for reggeized gluons and QCD RFT calculus. *Eur. Phys. J. C* **77**, 630 (2017). <https://doi.org/10.1140/epjc/s10052-017-5208-8>. [arXiv:1708.05183](https://arxiv.org/abs/1708.05183)
81. S. Bondarenko, S. Pozdnyakov, On correlators of Reggeon fields and operators of Wilson lines in high energy QCD. *Int. J. Mod. Phys. A* **33**, 1850204 (2018). <https://doi.org/10.1142/S0217751X18502044>. [arXiv:1806.02563](https://arxiv.org/abs/1806.02563)
82. I. Balitsky, Operator expansion for high-energy scattering. *Nucl. Phys. B* **463**, 99–160 (1996). [https://doi.org/10.1016/0550-3213\(95\)00638-9](https://doi.org/10.1016/0550-3213(95)00638-9). [arXiv:hep-ph/9509348](https://arxiv.org/abs/hep-ph/9509348)
83. Y.V. Kovchegov, Small x $F(2)$ structure function of a nucleus including multiple pomeron exchanges. *Phys. Rev. D* **60**, 034008 (1999). <https://doi.org/10.1103/PhysRevD.60.034008>. [arXiv:hep-ph/9901281](https://arxiv.org/abs/hep-ph/9901281)
84. A.H. Mueller, Soft gluons in the infinite momentum wave function and the BFKL pomeron. *Nucl. Phys. B* **415**, 373–385 (1994). [https://doi.org/10.1016/0550-3213\(94\)90116-3](https://doi.org/10.1016/0550-3213(94)90116-3)
85. Y.V. Kovchegov, Unitarization of the BFKL pomeron on a nucleus. *Phys. Rev. D* **61**, 074018 (2000). <https://doi.org/10.1103/PhysRevD.61.074018>. [arXiv:hep-ph/9905214](https://arxiv.org/abs/hep-ph/9905214)
86. E. Levin, K. Tuchin, Solution to the evolution equation for high parton density QCD. *Nucl. Phys. B* **573**, 833–852 (2000). [https://doi.org/10.1016/S0550-3213\(99\)00825-1](https://doi.org/10.1016/S0550-3213(99)00825-1). [arXiv:hep-ph/9908317](https://arxiv.org/abs/hep-ph/9908317)
87. E. Levin, K. Tuchin, New scaling at high-energy DIS. *Nucl. Phys. A* **691**, 779–790 (2001). [https://doi.org/10.1016/S0375-9474\(01\)00590-5](https://doi.org/10.1016/S0375-9474(01)00590-5). [arXiv:hep-ph/0012167](https://arxiv.org/abs/hep-ph/0012167)
88. E. Levin, K. Tuchin, Nonlinear evolution and saturation for heavy nuclei in DIS. *Nucl. Phys. A* **693**, 787–798 (2001). [https://doi.org/10.1016/S0375-9474\(01\)00880-6](https://doi.org/10.1016/S0375-9474(01)00880-6). [arXiv:hep-ph/0101275](https://arxiv.org/abs/hep-ph/0101275)
89. M. Braun, Structure function of the nucleus in the perturbative QCD with $N(c) \rightarrow \infty$ (BFKL pomeron fan diagrams). *Eur. Phys. J. C* **16**, 337–347 (2000). <https://doi.org/10.1007/s100520050026>. [arXiv:hep-ph/0001268](https://arxiv.org/abs/hep-ph/0001268)
90. N. Armesto, M.A. Braun, Parton densities and dipole cross-sections at small x in large nuclei. *Eur. Phys. J. C* **20**, 517–522 (2001). <https://doi.org/10.1007/s100520100685>. [arXiv:hep-ph/0104038](https://arxiv.org/abs/hep-ph/0104038)
91. M. Lublinsky, E. Gotsman, E. Levin, U. Maor, Nonlinear evolution and parton distributions at LHC and THERA energies. *Nucl. Phys. A* **696**, 851–869 (2001). [https://doi.org/10.1016/S0375-9474\(01\)01150-2](https://doi.org/10.1016/S0375-9474(01)01150-2). [arXiv:hep-ph/0102321](https://arxiv.org/abs/hep-ph/0102321)
92. M. Lublinsky, Scaling phenomena from nonlinear evolution in high-energy DIS. *Eur. Phys. J. C* **21**, 513–519 (2001). <https://doi.org/10.1007/s100520100752>. [arXiv:hep-ph/0106112](https://arxiv.org/abs/hep-ph/0106112)
93. K.J. Golec-Biernat, L. Motyka, A.M. Stasto, Diffusion into infrared and unitarization of the BFKL pomeron. *Phys. Rev. D* **65**, 074037 (2002). <https://doi.org/10.1103/PhysRevD.65.074037>. [arXiv:hep-ph/0110325](https://arxiv.org/abs/hep-ph/0110325)
94. K.J. Golec-Biernat, A.M. Stasto, On solutions of the Balitsky–Kovchegov equation with impact parameter. *Nucl. Phys. B* **668**, 345–363 (2003). <https://doi.org/10.1016/j.nuclphysb.2003.07.011>. [arXiv:hep-ph/0306279](https://arxiv.org/abs/hep-ph/0306279)
95. E. Gotsman, M. Kozlov, E. Levin, U. Maor, E. Naftali, Towards a new global QCD analysis: solution to the nonlinear equation at arbitrary impact parameter. *Nucl. Phys. A* **742**, 55–79 (2004). <https://doi.org/10.1016/j.nuclphysa.2004.05.018>. [arXiv:hep-ph/0401021](https://arxiv.org/abs/hep-ph/0401021)
96. T. Ikeda, L. McLerran, Impact parameter dependence in the Balitsky–Kovchegov equation. *Nucl. Phys. A* **756**, 385–398 (2005). <https://doi.org/10.1016/j.nuclphysa.2005.03.119>. [arXiv:hep-ph/0410345](https://arxiv.org/abs/hep-ph/0410345)

97. J. Berger, A. Stasto, Numerical solution of the nonlinear evolution equation at small x with impact parameter and beyond the LL approximation. *Phys. Rev. D* **83**, 034015 (2011). <https://doi.org/10.1103/PhysRevD.83.034015>. arXiv:1010.0671
98. A.H. Rezaeian, I. Schmidt, Impact-parameter dependent color glass condensate dipole model and new combined HERA data. *Phys. Rev. D* **88**, 074016 (2013). <https://doi.org/10.1103/PhysRevD.88.074016>. arXiv:1307.0825
99. D. Bendova, J. Cepila, J.G. Contreras, M. Matas, Solution to the Balitsky–Kovchegov equation with the collinearly improved kernel including impact-parameter dependence. *Phys. Rev. D* **100**, 054015 (2019). <https://doi.org/10.1103/PhysRevD.100.054015>. arXiv:1907.12123
100. J. Cepila, J.G. Contreras, M. Matas, Collinearly improved kernel suppresses Coulomb tails in the impact-parameter dependent Balitsky–Kovchegov evolution. *Phys. Rev. D* **99**, 051502 (2019). <https://doi.org/10.1103/PhysRevD.99.051502>. arXiv:1812.02548
101. T. Altinoluk, G. Beuf, A. Czajka, A. Tymowska, Quarks at next-to-eikonal accuracy in the CGC: forward quark-nucleus scattering. *Phys. Rev. D* **104**, 014019 (2021). <https://doi.org/10.1103/PhysRevD.104.014019>. arXiv:2012.03886
102. G.A. Chirilli, High-energy operator product expansion at sub-eikonal level. *JHEP* **06**, 096 (2021). [https://doi.org/10.1007/JHEP06\(2021\)096](https://doi.org/10.1007/JHEP06(2021)096). arXiv:2101.12744
103. Y.V. Kovchegov, M.G. Santiago, Quark sivers function at small x : spin-dependent odderon and the sub-eikonal evolution. *JHEP* **11**, 200 (2021). [https://doi.org/10.1007/JHEP11\(2021\)200](https://doi.org/10.1007/JHEP11(2021)200). arXiv:2108.03667
104. T. Altinoluk, G. Beuf, Quark and scalar propagators at next-to-eikonal accuracy in the CGC through a dynamical background gluon field. *Phys. Rev. D* **105**, 074026 (2022). <https://doi.org/10.1103/PhysRevD.105.074026>. arXiv:2109.01620
105. P. Agostini, T. Altinoluk, N. Armesto, F. Dominguez, J.G. Milhano, Multiparticle production in proton–nucleus collisions beyond eikonal accuracy. *Eur. Phys. J. C* **82**, 1001 (2022). <https://doi.org/10.1140/epjc/s10052-022-10962-1>. arXiv:2207.10472
106. T. Altinoluk, G. Beuf, A. Czajka, A. Tymowska, DIS dijet production at next-to-eikonal accuracy in the CGC. *Phys. Rev. D* **107**, 074016 (2023). <https://doi.org/10.1103/PhysRevD.107.074016>. arXiv:2212.10484
107. T. Altinoluk, N. Armesto, G. Beuf, Probing quark transverse momentum distributions in the Color Glass Condensate: quark-gluon dijets in Deep Inelastic Scattering at next-to-eikonal accuracy. arXiv:2303.12691
108. I. Balitsky, G.A. Chirilli, Next-to-leading order evolution of color dipoles. *Phys. Rev. D* **77**, 014019 (2008). <https://doi.org/10.1103/PhysRevD.77.014019>. arXiv:0710.4330
109. A. Kovner, M. Lublinsky, Y. Mulian, J.-M. Iancu, M. Weigert, L. Kovner, Evolution at next to leading order. *Phys. Rev. D* **89**, 061704 (2014). <https://doi.org/10.1103/PhysRevD.89.061704>. arXiv:1310.0378
110. A. Kovner, M. Lublinsky, Y. Mulian, NLO JIMWLK evolution unabridged. *JHEP* **08**, 114 (2014). [https://doi.org/10.1007/JHEP08\(2014\)114](https://doi.org/10.1007/JHEP08(2014)114). arXiv:1405.0418
111. T. Lappi, H. Mäntysaari, Direct numerical solution of the coordinate space Balitsky–Kovchegov equation at next to leading order. *Phys. Rev. D* **91**, 074016 (2015). <https://doi.org/10.1103/PhysRevD.91.074016>. arXiv:1502.02400
112. T. Lappi, H. Mäntysaari, Next-to-leading order Balitsky–Kovchegov equation with resummation. *Phys. Rev. D* **93**, 094004 (2016). <https://doi.org/10.1103/PhysRevD.93.094004>. arXiv:1601.06598
113. B. Ducloué, E. Iancu, A.H. Mueller, G. Soyez, D.N. Triantafyllopoulos, Non-linear evolution in QCD at high-energy beyond leading order. *JHEP* **04**, 081 (2019). [https://doi.org/10.1007/JHEP04\(2019\)081](https://doi.org/10.1007/JHEP04(2019)081). arXiv:1902.06637
114. L.D. McLerran, R. Venugopalan, Computing quark and gluon distribution functions for very large nuclei. *Phys. Rev. D* **49**, 2233–2241 (1994). <https://doi.org/10.1103/PhysRevD.49.2233>. arXiv:hep-ph/9309289
115. L.D. McLerran, R. Venugopalan, Gluon distribution functions for very large nuclei at small transverse momentum. *Phys. Rev. D* **49**, 3352–3355 (1994). <https://doi.org/10.1103/PhysRevD.49.3352>. arXiv:hep-ph/9311205
116. Y.V. Kovchegov, NonAbelian Weizsacker–Williams field and a two-dimensional effective color charge density for a very large nucleus. *Phys. Rev. D* **54**, 5463–5469 (1996). <https://doi.org/10.1103/PhysRevD.54.5463>. arXiv:hep-ph/9605446
117. J. Jalilian-Marian, A. Kovner, L.D. McLerran, H. Weigert, The Intrinsic glue distribution at very small x . *Phys. Rev. D* **55**, 5414–5428 (1997). <https://doi.org/10.1103/PhysRevD.55.5414>. arXiv:hep-ph/9606337
118. J. Jalilian-Marian, A. Kovner, A. Leonidov, H. Weigert, The BFKL equation from the Wilson renormalization group. *Nucl. Phys. B* **504**, 415–431 (1997). [https://doi.org/10.1016/S0550-3213\(97\)00440-9](https://doi.org/10.1016/S0550-3213(97)00440-9). arXiv:hep-ph/9701284
119. A. Kovner, J.G. Milhano, H. Weigert, Relating different approaches to nonlinear QCD evolution at finite gluon density. *Phys. Rev. D* **62**, 114005 (2000). <https://doi.org/10.1103/PhysRevD.62.114005>. arXiv:hep-ph/0004014
120. A. Kovner, J.G. Milhano, Vector potential versus color charge density in low x evolution. *Phys. Rev. D* **61**, 014012 (2000). <https://doi.org/10.1103/PhysRevD.61.014012>. arXiv:hep-ph/9904420
121. H. Weigert, Unitarity at small Bjorken x . *Nucl. Phys. A* **703**, 823–860 (2002). [https://doi.org/10.1016/S0375-9474\(01\)01668-2](https://doi.org/10.1016/S0375-9474(01)01668-2). arXiv:hep-ph/0004044
122. E. Iancu, A. Leonidov, L.D. McLerran, Nonlinear gluon evolution in the color glass condensate. 1. *Nucl. Phys. A* **692**, 583–645 (2001). [https://doi.org/10.1016/S0375-9474\(01\)00642-X](https://doi.org/10.1016/S0375-9474(01)00642-X). arXiv:hep-ph/0011241
123. E. Ferreira, E. Iancu, A. Leonidov, L. McLerran, Nonlinear gluon evolution in the color glass condensate. 2. *Nucl. Phys. A* **703**, 489–538 (2002). [https://doi.org/10.1016/S0375-9474\(01\)01329-X](https://doi.org/10.1016/S0375-9474(01)01329-X). arXiv:hep-ph/0109115
124. A. Dumitru, A. Hayashigaki, J. Jalilian-Marian, The color glass condensate and hadron production in the forward region. *Nucl. Phys. A* **765**, 464–482 (2006). <https://doi.org/10.1016/j.nuclphysa.2005.11.014>. arXiv:hep-ph/0506308
125. H. Fujii, F. Gelis, R. Venugopalan, Quark pair production in high energy pA collisions: General features. *Nucl. Phys. A* **780**, 146–174 (2006). <https://doi.org/10.1016/j.nuclphysa.2006.09.012>. arXiv:hep-ph/0603099
126. E. Iancu, J. Laidet, Gluon splitting in a shockwave. *Nucl. Phys. A* **916**, 48–78 (2013). <https://doi.org/10.1016/j.nuclphysa.2013.07.012>. arXiv:1305.5926
127. G.A. Chirilli, B.-W. Xiao, F. Yuan, One-loop factorization for inclusive hadron production in pA collisions in the saturation formalism. *Phys. Rev. Lett.* **108**, 122301 (2012). <https://doi.org/10.1103/PhysRevLett.108.122301>. arXiv:1112.1061
128. G.A. Chirilli, B.-W. Xiao, F. Yuan, Inclusive Hadron Productions in pA collisions. *Phys. Rev. D* **86**, 054005 (2012). <https://doi.org/10.1103/PhysRevD.86.054005>. arXiv:1203.6139
129. A.M. Stasto, B.-W. Xiao, D. Zaslavsky, Towards the test of saturation physics beyond leading logarithm. *Phys. Rev. Lett.* **112**, 012302 (2014). <https://doi.org/10.1103/PhysRevLett.112.012302>. arXiv:1307.4057
130. B. Ducloué, T. Lappi, Y. Zhu, Single inclusive forward hadron production at next-to-leading order. *Phys. Rev. D* **93**, 114016 (2016). <https://doi.org/10.1103/PhysRevD.93.114016>. arXiv:1604.00225

131. E. Iancu, A.H. Mueller, D.N. Triantafyllopoulos, CGC factorization for forward particle production in proton-nucleus collisions at next-to-leading order. *JHEP* **12**, 041 (2016). [https://doi.org/10.1007/JHEP12\(2016\)041](https://doi.org/10.1007/JHEP12(2016)041). arXiv:1608.05293
132. H.-Y. Liu, Y.-Q. Ma, K.-T. Chao, Improvement for color glass condensate factorization: single hadron production in pA collisions at next-to-leading order. *Phys. Rev. D* **100**, 071503 (2019). <https://doi.org/10.1103/PhysRevD.100.071503>. arXiv:1909.02370
133. H.-Y. Liu, K. Xie, Z. Kang, X. Liu, Single inclusive jet production in pA collisions at NLO in the small-x regime. *JHEP* **07**, 041 (2022). [https://doi.org/10.1007/JHEP07\(2022\)041](https://doi.org/10.1007/JHEP07(2022)041). arXiv:2204.03026
134. B. Ducloué, H. Hänninen, T. Lappi, Y. Zhu, Deep inelastic scattering in the dipole picture at next-to-leading order. *Phys. Rev. D* **96**, 094017 (2017). <https://doi.org/10.1103/PhysRevD.96.094017>. arXiv:1708.07328
135. G. Beuf, T. Lappi, R. Paatelainen, Massive quarks in NLO dipole factorization for DIS: transverse photon. *Phys. Rev. D* **106**, 034013 (2022). <https://doi.org/10.1103/PhysRevD.106.034013>. arXiv:2204.02486
136. H. Hänninen, H. Mäntysaari, R. Paatelainen, J. Penttala, Proton structure functions at next-to-leading order in the dipole picture with massive quarks. *Phys. Rev. Lett.* **130**, 192301 (2023). <https://doi.org/10.1103/PhysRevLett.130.192301>. arXiv:2211.03504
137. P. Caucal, F. Salazar, R. Venugopalan, Dijet impact factor in DIS at next-to-leading order in the color glass condensate. *JHEP* **11**, 222 (2021). [https://doi.org/10.1007/JHEP11\(2021\)222](https://doi.org/10.1007/JHEP11(2021)222). arXiv:2108.06347
138. P. Caucal, F. Salazar, B. Schenke, R. Venugopalan, Back-to-back inclusive dijets in DIS at small x : Sudakov suppression and gluon saturation at NLO. arXiv:2208.13872
139. P. Caucal, F. Salazar, B. Schenke, T. Stebel, R. Venugopalan, Back-to-back inclusive dijets in DIS at small x : Gluon Weizsäcker–Williams distribution at NLO. arXiv:2304.03304
140. H. Mäntysaari, J. Penttala, Exclusive production of light vector mesons at next-to-leading order in the dipole picture. *Phys. Rev. D* **105**, 114038 (2022). <https://doi.org/10.1103/PhysRevD.105.114038>. arXiv:2203.16911
141. H. Mäntysaari, J. Penttala, Complete calculation of exclusive heavy vector meson production at next-to-leading order in the dipole picture. *JHEP* **08**, 247 (2022). [https://doi.org/10.1007/JHEP08\(2022\)247](https://doi.org/10.1007/JHEP08(2022)247). arXiv:2204.14031
142. E. Iancu, Y. Mulian, Forward dijets in proton–nucleus collisions at next-to-leading order: the real corrections. *JHEP* **03**, 005 (2021). [https://doi.org/10.1007/JHEP03\(2021\)005](https://doi.org/10.1007/JHEP03(2021)005). arXiv:2009.11930
143. E. Iancu, Y. Mulian, Dihadron production in DIS at NLO: the real corrections. arXiv:2211.04837
144. P. Taels, T. Altinoluk, G. Beuf, C. Marquet, Dijet photoproduction at low x at next-to-leading order and its back-to-back limit. arXiv:2204.11650
145. P. Taels, Forward production of a Drell–Yan pair and a jet at small x at next-to-leading order. arXiv:2308.02449
146. T. Altinoluk, R. Boussarie, C. Marquet, P. Taels, TMD factorization for dijets + photon production from the dilute-dense CGC framework. *JHEP* **07**, 079 (2019). [https://doi.org/10.1007/JHEP07\(2019\)079](https://doi.org/10.1007/JHEP07(2019)079). arXiv:1810.11273
147. E. Iancu, Y. Mulian, Forward trijet production in proton–nucleus collisions. *Nucl. Phys. A* **985**, 66–127 (2019). <https://doi.org/10.1016/j.nuclphysa.2019.02.003>. arXiv:1809.05526
148. T. Altinoluk, R. Boussarie, C. Marquet, P. Taels, Photoproduction of three jets in the CGC: gluon TMDs and dilute limit. *JHEP* **07**, 143 (2020). [https://doi.org/10.1007/JHEP07\(2020\)143](https://doi.org/10.1007/JHEP07(2020)143). arXiv:2001.00765
149. J.C. Collins, R. Ellis, Heavy quark production in very high-energy hadron collisions. *Nucl. Phys. B* **360**, 3–30 (1991). [https://doi.org/10.1016/0550-3213\(91\)90288-9](https://doi.org/10.1016/0550-3213(91)90288-9)
150. S. Catani, M. Ciafaloni, F. Hautmann, High-energy factorization and small x heavy flavor production. *Nucl. Phys. B* **366**, 135–188 (1991). [https://doi.org/10.1016/0550-3213\(91\)90055-3](https://doi.org/10.1016/0550-3213(91)90055-3)
151. S. Catani, F. Hautmann, Quark anomalous dimensions at small x . *Phys. Lett. B* **315**, 157–163 (1993). [https://doi.org/10.1016/0370-2693\(93\)90174-G](https://doi.org/10.1016/0370-2693(93)90174-G)
152. S. Catani, F. Hautmann, High-energy factorization and small x deep inelastic scattering beyond leading order. *Nucl. Phys. B* **427**, 475–524 (1994). [https://doi.org/10.1016/0550-3213\(94\)90636-X](https://doi.org/10.1016/0550-3213(94)90636-X). arXiv:hep-ph/9405388
153. M. Ciafaloni, Coherence effects in initial jets at small q^{*2}/s . *Nucl. Phys. B* **296**, 49–74 (1988). [https://doi.org/10.1016/0550-3213\(88\)90380-X](https://doi.org/10.1016/0550-3213(88)90380-X)
154. S. Catani, F. Fiorani, G. Marchesini, Small x behavior of initial state radiation in perturbative QCD. *Nucl. Phys. B* **336**, 18–85 (1990). [https://doi.org/10.1016/0550-3213\(90\)90342-B](https://doi.org/10.1016/0550-3213(90)90342-B)
155. A. van Hameren, P. Kotko, K. Kutak, Helicity amplitudes for high-energy scattering. *JHEP* **01**, 078 (2013). [https://doi.org/10.1007/JHEP01\(2013\)078](https://doi.org/10.1007/JHEP01(2013)078). arXiv:1211.0961
156. CASCADE collaboration, H. Jung et al., The CCFM Monte Carlo generator CASCADE version 2.2.03. *Eur. Phys. J. C* **70**, 1237–1249 (2010). <https://doi.org/10.1140/epjc/s10052-010-1507-z>. arXiv:1008.0152
157. CASCADE collaboration, S. Baranov et al., CASCADE3 A Monte Carlo event generator based on TMDs. *Eur. Phys. J. C* **81**, 425 (2021). <https://doi.org/10.1140/epjc/s10052-021-09203-8>. arXiv:2101.10221
158. A. van Hameren, P. Kotko, K. Kutak, Multi-gluon helicity amplitudes with one off-shell leg within high energy factorization. *JHEP* **12**, 029 (2012). [https://doi.org/10.1007/JHEP12\(2012\)029](https://doi.org/10.1007/JHEP12(2012)029). arXiv:1207.3332
159. P. Kotko, Wilson lines and gauge invariant off-shell amplitudes. *JHEP* **07**, 128 (2014). [https://doi.org/10.1007/JHEP07\(2014\)128](https://doi.org/10.1007/JHEP07(2014)128). arXiv:1403.4824
160. A. van Hameren, BCFW recursion for off-shell gluons. *JHEP* **07**, 138 (2014). [https://doi.org/10.1007/JHEP07\(2014\)138](https://doi.org/10.1007/JHEP07(2014)138). arXiv:1404.7818
161. A. van Hameren, M. Serino, BCFW recursion for TMD parton scattering. *JHEP* **07**, 010 (2015). [https://doi.org/10.1007/JHEP07\(2015\)010](https://doi.org/10.1007/JHEP07(2015)010). arXiv:1504.00315
162. M. Deak, F. Hautmann, H. Jung, K. Kutak, Forward jet production at the large hadron collider. *JHEP* **09**, 121 (2009). <https://doi.org/10.1088/1126-6708/2009/09/121>. arXiv:0908.0538
163. R. Angeles-Martinez et al., Transverse momentum dependent (TMD) parton distribution functions: status and prospects. *Acta Phys. Pol. B* **46**, 2501–2534 (2015). <https://doi.org/10.5506/APhysPolB.46.2501>. arXiv:1507.05267
164. R. Boussarie et al., TMD Handbook. arXiv:2304.03302
165. C.J. Bomhof, P.J. Mulders, F. Pijlman, The construction of gauge-links in arbitrary hard processes. *Eur. Phys. J. C* **47**, 147–162 (2006). <https://doi.org/10.1140/epjc/s2006-02554-2>. arXiv:hep-ph/0601171
166. M. Bury, P. Kotko, K. Kutak, TMD gluon distributions for multi-parton processes. *Eur. Phys. J. C* **79**, 152 (2019). <https://doi.org/10.1140/epjc/s10052-019-6652-4>. arXiv:1809.08968
167. B.-W. Xiao, F. Yuan, Non-universality of transverse momentum dependent parton distributions at small- x . *Phys. Rev. Lett.* **105**, 062001 (2010). <https://doi.org/10.1103/PhysRevLett.105.062001>. arXiv:1003.0482
168. F. Dominguez, C. Marquet, B.-W. Xiao, F. Yuan, Universality of unintegrated gluon distributions at small x . *Phys. Rev. D* **83**, 105005 (2011). <https://doi.org/10.1103/PhysRevD.83.105005>. arXiv:1101.0715
169. A. Metz, J. Zhou, Distribution of linearly polarized gluons inside a large nucleus. *Phys. Rev. D* **84**, 051503 (2011). <https://doi.org/10.1103/PhysRevD.84.051503>. arXiv:1105.1991

170. E. Akcakaya, A. Schäfer, J. Zhou, Azimuthal asymmetries for quark pair production in pA collisions. *Phys. Rev. D* **87**, 054010 (2013). <https://doi.org/10.1103/PhysRevD.87.054010>. arXiv:1208.4965
171. I. Balitsky, A. Tarasov, Rapidity evolution of gluon TMD from low to moderate x . *JHEP* **10**, 017 (2015). [https://doi.org/10.1007/JHEP10\(2015\)017](https://doi.org/10.1007/JHEP10(2015)017). arXiv:1505.02151
172. I. Balitsky, A. Tarasov, Gluon TMD in particle production from low to moderate x . *JHEP* **06**, 164 (2016). [https://doi.org/10.1007/JHEP06\(2016\)164](https://doi.org/10.1007/JHEP06(2016)164). arXiv:1603.06548
173. Y.V. Kovchegov, M.D. Sievert, Calculating TMDs of a large nucleus: quasi-classical approximation and quantum evolution. *Nucl. Phys. B* **903**, 164–203 (2016). <https://doi.org/10.1016/j.nuclphysb.2015.12.008>. arXiv:1505.01176
174. Y.V. Kovchegov, D. Pitonyak, M.D. Sievert, Helicity evolution at small- x . *JHEP* **01**, 072 (2016). [https://doi.org/10.1007/JHEP01\(2016\)072](https://doi.org/10.1007/JHEP01(2016)072). arXiv:1511.06737
175. Y.V. Kovchegov, D. Pitonyak, M.D. Sievert, Small- x asymptotics of the gluon helicity distribution. *JHEP* **10**, 198 (2017). [https://doi.org/10.1007/JHEP10\(2017\)198](https://doi.org/10.1007/JHEP10(2017)198). arXiv:1706.04236
176. Y.V. Kovchegov, M.D. Sievert, Small- x helicity evolution: an operator treatment. *Phys. Rev. D* **99**, 054032 (2019). <https://doi.org/10.1103/PhysRevD.99.054032>. arXiv:1808.09010
177. R. Boussarie, Y. Mehtar-Tani, A novel formulation of the unintegrated gluon distribution for DIS. *Phys. Lett. B* **831**, 137125 (2022). <https://doi.org/10.1016/j.physletb.2022.137125>. arXiv:2006.14569
178. R. Boussarie, Y. Mehtar-Tani, Gluon-mediated inclusive deep inelastic scattering from Regge to Bjorken kinematics. *JHEP* **07**, 080 (2022). [https://doi.org/10.1007/JHEP07\(2022\)080](https://doi.org/10.1007/JHEP07(2022)080). arXiv:2112.01412
179. C. Marquet, E. Petreska, C. Roiesnel, Transverse-momentum-dependent gluon distributions from JIMWLK evolution. *JHEP* **10**, 065 (2016). [https://doi.org/10.1007/JHEP10\(2016\)065](https://doi.org/10.1007/JHEP10(2016)065). arXiv:1608.02577
180. T. Altinoluk, R. Boussarie, Low x physics as an infinite twist (G)TMD framework: unravelling the origins of saturation. *JHEP* **10**, 208 (2019). [https://doi.org/10.1007/JHEP10\(2019\)208](https://doi.org/10.1007/JHEP10(2019)208). arXiv:1902.07930
181. T. Altinoluk, R. Boussarie, P. Kotko, Interplay of the CGC and TMD frameworks to all orders in kinematic twist. *JHEP* **05**, 156 (2019). [https://doi.org/10.1007/JHEP05\(2019\)156](https://doi.org/10.1007/JHEP05(2019)156). arXiv:1901.01175
182. M.L. Mangano, S.J. Parke, Multiparton amplitudes in gauge theories. *Phys. Rep.* **200**, 301–367 (1991). [https://doi.org/10.1016/0370-1573\(91\)90091-Y](https://doi.org/10.1016/0370-1573(91)90091-Y). arXiv:hep-th/0509223
183. T. Altinoluk, C. Marquet, P. Taels, Low- x improved TMD approach to the lepto- and hadroproduction of a heavy-quark pair. *JHEP* **06**, 085 (2021). [https://doi.org/10.1007/JHEP06\(2021\)085](https://doi.org/10.1007/JHEP06(2021)085). arXiv:2103.14495
184. R. Boussarie, H. Mäntysaari, F. Salazar, B. Schenke, The importance of kinematic twists and genuine saturation effects in dijet production at the electron-ion collider. *JHEP* **09**, 178 (2021). [https://doi.org/10.1007/JHEP09\(2021\)178](https://doi.org/10.1007/JHEP09(2021)178). arXiv:2106.11301
185. M. Bury, A. van Hameren, P. Kotko, K. Kutak, Forward trijet production in p–p and p–Pb collisions at LHC. *JHEP* **09**, 175 (2020). [https://doi.org/10.1007/JHEP09\(2020\)175](https://doi.org/10.1007/JHEP09(2020)175). arXiv:2006.13175
186. A. van Hameren, KaTie: for parton-level event generation with k_T -dependent initial states. *Comput. Phys. Commun.* **224**, 371–380 (2018). <https://doi.org/10.1016/j.cpc.2017.11.005>. arXiv:1611.00680
187. J. Alwall et al., A Standard format for Les Houches event files. *Comput. Phys. Commun.* **176**, 300–304 (2007). <https://doi.org/10.1016/j.cpc.2006.11.010>. arXiv:hep-ph/0609017
188. N.A. Abdulov et al., TMDlib2 and TMDplotter: a platform for 3D hadron structure studies. *Eur. Phys. J. C* **81**, 752 (2021). <https://doi.org/10.1140/epjc/s10052-021-09508-8>. arXiv:2103.09741
189. F. Caravaglios, M. Moretti, An algorithm to compute Born scattering amplitudes without Feynman graphs. *Phys. Lett. B* **358**, 332–338 (1995). [https://doi.org/10.1016/0370-2693\(95\)00971-M](https://doi.org/10.1016/0370-2693(95)00971-M). arXiv:hep-ph/9507237
190. M.L. Mangano, M. Moretti, F. Piccinini, R. Pittau, A.D. Polosa, ALPGEN, a generator for hard multiparton processes in hadronic collisions. *JHEP* **07**, 001 (2003). <https://doi.org/10.1088/1126-6708/2003/07/001>. arXiv:hep-ph/0206293
191. K. Kutak, J. Kwiecinski, Screening effects in the ultrahigh-energy neutrino interactions. *Eur. Phys. J. C* **29**, 521 (2003). <https://doi.org/10.1140/epjc/s2003-01236-y>. arXiv:hep-ph/0303209
192. M.A. Kimber, J. Kwiecinski, A.D. Martin, Gluon shadowing in the low x region probed by the LHC. *Phys. Lett. B* **508**, 58–64 (2001). [https://doi.org/10.1016/S0370-2693\(01\)00235-0](https://doi.org/10.1016/S0370-2693(01)00235-0). arXiv:hep-ph/0101099
193. A. Kovner, U.A. Wiedemann, No Froissart bound from gluon saturation. *Phys. Lett. B* **551**, 311–316 (2003). [https://doi.org/10.1016/S0370-2693\(02\)02907-6](https://doi.org/10.1016/S0370-2693(02)02907-6). arXiv:hep-ph/0207335
194. N.N. Nikolaev, W. Schafer, Quenching of leading jets and particles: the p perp dependent Landau–Pomeranchuk–Migdal effect from nonlinear k perp factorization. *Phys. Rev. D* **74**, 014023 (2006). <https://doi.org/10.1103/PhysRevD.74.014023>. arXiv:hep-ph/0604117
195. J. Kwiecinski, A.D. Martin, A. Stasto, A unified BFKL and GLAP description of F2 data. *Phys. Rev. D* **56**, 3991–4006 (1997). <https://doi.org/10.1103/PhysRevD.56.3991>. arXiv:hep-ph/9703445
196. H1, ZEUS collaboration, F. Aaron et al., Combined measurement and QCD analysis of the inclusive e^+p scattering cross sections at HERA. *JHEP* **01**, 109 (2010). [https://doi.org/10.1007/JHEP01\(2010\)109](https://doi.org/10.1007/JHEP01(2010)109). arXiv:0911.0884
197. S. Bondarenko, Gluon density and $F(2)$ functions from BK equation with impact parameter dependence. *Phys. Lett. B* **665**, 72–78 (2008). <https://doi.org/10.1016/j.physletb.2008.05.053>. arXiv:0802.1802
198. M.A. Kimber, A.D. Martin, M.G. Ryskin, Unintegrated parton distributions and prompt photon hadroproduction. *Eur. Phys. J. C* **12**, 655–661 (2000). <https://doi.org/10.1007/s100520000326>. arXiv:hep-ph/9911379
199. F. Hautmann, H. Jung, A. Lelek, V. Radescu, R. Zlebcik, Soft-gluon resolution scale in QCD evolution equations. *Phys. Lett. B* **772**, 446–451 (2017). <https://doi.org/10.1016/j.physletb.2017.07.005>. arXiv:1704.01757
200. F. Hautmann, H. Jung, A. Lelek, V. Radescu, R. Zlebcik, Collinear and TMD quark and gluon densities from parton branching solution of QCD evolution equations. *JHEP* **01**, 070 (2018). [https://doi.org/10.1007/JHEP01\(2018\)070](https://doi.org/10.1007/JHEP01(2018)070). arXiv:1708.03279
201. R.K. Ellis, W.J. Stirling, B.R. Webber, *QCD and collider physics*, vol. 8 (Cambridge University Press, 2011). <https://doi.org/10.1017/CBO9780511628788>
202. A. Mueller, B.-W. Xiao, F. Yuan, Sudakov double logarithms resummation in hard processes in the small- x saturation formalism. *Phys. Rev. D* **88**, 114010 (2013). <https://doi.org/10.1103/PhysRevD.88.114010>. arXiv:1308.2993
203. A.H. Mueller, L. Szymanowski, S. Wallon, B.-W. Xiao, F. Yuan, Sudakov Resummations in Mueller–Navelet Dijet production. *JHEP* **03**, 096 (2016). [https://doi.org/10.1007/JHEP03\(2016\)096](https://doi.org/10.1007/JHEP03(2016)096). arXiv:1512.07127
204. A. Mueller, B. Wu, B.-W. Xiao, F. Yuan, Medium induced transverse momentum broadening in hard processes. *Phys. Rev. D* **95**, 034007 (2017). <https://doi.org/10.1103/PhysRevD.95.034007>. arXiv:1608.07339

205. A. Mueller, B.-W. Xiao, F. Yuan, Sudakov resummation in small- x saturation formalism. *Phys. Rev. Lett.* **110**, 082301 (2013). <https://doi.org/10.1103/PhysRevLett.110.082301>. arXiv:1210.5792
206. C. Marquet, S.-Y. Wei, B.-W. Xiao, Probing parton saturation with forward Z^0 -boson production at small transverse momentum in p+p and p+A collisions. *Phys. Lett. B* **802**, 135253 (2020). <https://doi.org/10.1016/j.physletb.2020.135253>. arXiv:1909.08572
207. P. Sun, J. Isaacson, C.P. Yuan, F. Yuan, Nonperturbative functions for SIDIS and Drell–Yan processes. *Int. J. Mod. Phys. A* **33**, 1841006 (2018). <https://doi.org/10.1142/S0217751X18410063>. arXiv:1406.3073
208. G. Watt, A. Martin, M. Ryskin, Unintegrated parton distributions and inclusive jet production at HERA. *Eur. Phys. J. C* **31**, 73–89 (2003). <https://doi.org/10.1140/epjc/s2003-01320-4>. arXiv:hep-ph/0306169
209. A. van Hameren, P. Kotko, K. Kutak, C. Marquet, E. Petreska, S. Sapeta, Forward di-jet production in p+Pb collisions in the small- x improved TMD factorization framework. *JHEP* **12**, 034 (2016). [https://doi.org/10.1007/JHEP12\(2016\)034](https://doi.org/10.1007/JHEP12(2016)034). arXiv:1607.03121
210. M.A. Al-Mashad, A. van Hameren, H. Kakkad, P. Kotko, K. Kutak, P. van Mechelen et al., Dijet azimuthal correlations in p-p and p-Pb collisions at forward LHC calorimeters. *JHEP* **12**, 131 (2022). [https://doi.org/10.1007/JHEP12\(2022\)131](https://doi.org/10.1007/JHEP12(2022)131). arXiv:2210.06613
211. H. Fujii, C. Marquet, K. Watanabe, Comparison of improved TMD and CGC frameworks in forward quark dijet production. *JHEP* **12**, 181 (2020). [https://doi.org/10.1007/JHEP12\(2020\)181](https://doi.org/10.1007/JHEP12(2020)181). arXiv:2006.16279
212. M.A. Al-Mashad, A. van Hameren, H. Kakkad, P. Kotko, K. Kutak, P. van Mechelen et al., Dijet azimuthal correlations in p-p and p-pb collisions at forward lhc calorimeters (2022)
213. M. Cacciari, G.P. Salam, G. Soyez, The anti- k_r jet clustering algorithm. *JHEP* (04) (2008). <https://doi.org/10.1088/1126-6708/2008/04/063>. arXiv:0802.1189
214. H.-L. Lai, M. Guzzi, J. Huston, Z. Li, P.M. Nadolsky, J. Pumplin et al., New parton distributions for collider physics. *Phys. Rev. D* **82** (2010). <https://doi.org/10.1103/physrevd.82.074024>
215. A. Buckley, J. Ferrando, S. Lloyd, K. Nordström, B. Page, M. Rüfenacht et al., LHAPDF6: parton density access in the LHC precision era. *Eur. Phys. J. C* **75** (2015). <https://doi.org/10.1140/epjc/s10052-015-3318-8>
216. T. Sjöstrand, S. Mrenna, P.Z. Skands, PYTHIA 6.4 Physics and Manual. *JHEP* **05**, 026 (2006). <https://doi.org/10.1088/1126-6708/2006/05/026>. arXiv:hep-ph/0603175
217. T. Sjöstrand, S. Ask, J.R. Christiansen et al., An introduction to PYTHIA 8.2. *Comput. Phys. Commun.* **191**, 159–177 (2015). <https://doi.org/10.1016/j.cpc.2015.01.024>. arXiv:1410.3012
218. M. Bury, A. van Hameren, H. Jung, K. Kutak, S. Sapeta, M. Serino, Calculations with off-shell matrix elements, TMD parton densities and TMD parton showers. *Eur. Phys. J. C* **78**, 137 (2018). <https://doi.org/10.1140/epjc/s10052-018-5642-2>. arXiv:1712.05932
219. M. Arratia, Y. Song, F. Ringer, B.V. Jacak, Jets as precision probes in electron-nucleus collisions at the future electron-ion collider. *Phys. Rev. C* **101**, 065204 (2020). <https://doi.org/10.1103/PhysRevC.101.065204>. arXiv:1912.05931
220. H.T. Li, I. Vitev, Nuclear matter effects on jet production at electron-ion colliders. arXiv:2010.05912
221. F. Bergabo, J. Jalilian-Marian, Single inclusive hadron production in DIS at small x : next to leading order corrections. *JHEP* **01**, 095 (2023). [https://doi.org/10.1007/JHEP01\(2023\)095](https://doi.org/10.1007/JHEP01(2023)095). arXiv:2210.03208
222. F. Bergabo, J. Jalilian-Marian, Dihadron production in DIS at small x at next-to-leading order: transverse photons. *Phys. Rev. D* **107**, 054036 (2023). <https://doi.org/10.1103/PhysRevD.107.054036>. arXiv:2301.03117
223. P. Kotko, K. Kutak, S. Sapeta, A.M. Stasto, M. Strikman, Estimating nonlinear effects in forward dijet production in ultra-peripheral heavy ion collisions at the LHC. *Eur. Phys. J. C* **77**, 353 (2017). <https://doi.org/10.1140/epjc/s10052-017-4906-6>. arXiv:1702.03063
224. A. van Hameren, P. Kotko, K. Kutak, S. Sapeta, E. Żarów, Probing gluon number density with electron-dijet correlations at EIC. *Eur. Phys. J. C* **81**, 741 (2021). <https://doi.org/10.1140/epjc/s10052-021-09529-3>. arXiv:2106.13964
225. T. Goda, K. Kutak, S. Sapeta, Effects of gluon kinematics and the Sudakov form factor on the dipole amplitude. arXiv:2305.14025
226. M. Hentschinski et al., White paper on forward physics, BFKL, saturation physics and diffraction. *Acta Phys. Pol. B* **54**, 2 (2023). <https://doi.org/10.5506/APhysPolB.54.3-A2>. arXiv:2203.08129
227. J.L. Albacete, G. Giacalone, C. Marquet, M. Matas, Forward dihadron back-to-back correlations in pA collisions. *Phys. Rev. D* **99**, 014002 (2019). <https://doi.org/10.1103/PhysRevD.99.014002>. arXiv:1805.05711
228. J. Jalilian-Marian, A.H. Rezaeian, Hadron production in pA collisions at the LHC from the color glass condensate. *Phys. Rev. D* **85**, 014017 (2012). <https://doi.org/10.1103/PhysRevD.85.014017>. arXiv:1110.2810
229. B. Ducloué, T. Lappi, H. Mäntysaari, Forward J/ψ production in proton-nucleus collisions at high energy. *Phys. Rev. D* **91**, 114005 (2015). <https://doi.org/10.1103/PhysRevD.91.114005>. arXiv:1503.02789
230. M. Hentschinski, J.D. Madrigal Martínez, B. Murdaca, A. Sabio Vera, NLO vertex for a forward jet plus a rapidity gap at high energies. *AIP Conf. Proc.* **1654**, 070013 (2015). <https://doi.org/10.1063/1.4916003>. arXiv:1409.7731
231. E. Blanco, A. van Hameren, P. Kotko, K. Kutak, All-plus helicity off-shell gauge invariant multigluon amplitudes at one loop. *JHEP* **12**, 158 (2020). [https://doi.org/10.1007/JHEP12\(2020\)158](https://doi.org/10.1007/JHEP12(2020)158). arXiv:2008.07916
232. A. van Hameren, L. Motyka, G. Ziarko, Hybrid k_T factorization and impact factors at NLO. *JHEP* **11**, 103 (2022). [https://doi.org/10.1007/JHEP11\(2022\)103](https://doi.org/10.1007/JHEP11(2022)103). arXiv:2205.09585
233. E. Blanco, A. Giachino, A. van Hameren, P. Kotko, One-loop gauge invariant amplitudes with a space-like gluon. arXiv:2212.03572
234. M. Hentschinski, A. Sabio Vera, C. Salas, Hard to soft pomeron transition in small- x deep inelastic scattering data using optimal renormalization. *Phys. Rev. Lett.* **110**, 041601 (2013). <https://doi.org/10.1103/PhysRevLett.110.041601>. arXiv:1209.1353
235. E. Iancu, J.D. Madrigal, A.H. Mueller, G. Soyez, D.N. Triantafyllopoulos, Collinearly-improved BK evolution meets the HERA data. *Phys. Lett. B* **750**, 643–652 (2015). <https://doi.org/10.1016/j.physletb.2015.09.071>. arXiv:1507.03651
236. M. Hentschinski, A. Kusina, K. Kutak, Transverse momentum dependent splitting functions at work: quark-to-gluon splitting. *Phys. Rev. D* **94**, 114013 (2016). <https://doi.org/10.1103/PhysRevD.94.114013>. arXiv:1607.01507
237. M. Hentschinski, A. Kusina, K. Kutak, M. Serino, TMD splitting functions in k_T factorization: the real contribution to the gluon-to-gluon splitting. *Eur. Phys. J. C* **78**, 174 (2018). <https://doi.org/10.1140/epjc/s10052-018-5634-2>. arXiv:1711.04587
238. Y. Shi, L. Wang, S.-Y. Wei, B.-W. Xiao, Pursuing the precision study for color glass condensate in forward hadron productions. *Phys. Rev. Lett.* **128**, 202302 (2022). <https://doi.org/10.1103/PhysRevLett.128.202302>. arXiv:2112.06975
239. W. Li, A.M. Stasto, Structure functions from renormalization group improved small x evolution. *Eur. Phys. J. C* **82**, 562 (2022). <https://doi.org/10.1140/epjc/s10052-022-10523-6>. arXiv:2201.10579
240. F. Hautmann, M. Hentschinski, L. Keersmaekers, A. Kusina, K. Kutak, A. Lelek, A parton branching with transverse

- momentum dependent splitting functions. *Phys. Lett. B* **833**, 137276 (2022). <https://doi.org/10.1016/j.physletb.2022.137276>. [arXiv:2205.15873](https://arxiv.org/abs/2205.15873)
241. M. Hentschinski, Transverse momentum dependent gluon distribution within high energy factorization at next-to-leading order. *Phys. Rev. D* **104**, 054014 (2021). <https://doi.org/10.1103/PhysRevD.104.054014>. [arXiv:2107.06203](https://arxiv.org/abs/2107.06203)
242. M. Hentschinski, K. Kutak, A. van Hameren, Forward Higgs production within high energy factorization in the heavy quark limit at next-to-leading order accuracy. *Eur. Phys. J. C* **81**, 112 (2021). <https://doi.org/10.1140/epjc/s10052-021-08902-6>. [arXiv:2011.03193](https://arxiv.org/abs/2011.03193)
243. C. Marquet, C. Roiesnel, P. Taels, Linearly polarized small- x gluons in forward heavy-quark pair production. *Phys. Rev. D* **97**, 014004 (2018). <https://doi.org/10.1103/PhysRevD.97.014004>. [arXiv:1710.05698](https://arxiv.org/abs/1710.05698)